LIMITED DATA PROBLEMS IN X-RAY AND POLARIZED LIGHT TOMOGRAPHY

A thesis submitted to the University of Manchester
for the degree of Doctor of Philosophy
in the Faculty of Engineering and Physical Sciences

2011

David Szotten

School of Mathematics

Contents

Word count 19136

List of Tables

List of Figures

The University of Manchester

David Szotten
Doctor of Philosophy
Limited Data Problems in X-Ray and Polarized Light Tomography
January 17, 2011

Abstract

We present new reconstruction results and methods for limited data problems in photoelastic tomography. We begin with a survey of the current state of x-ray tomography. Discussing the Radon transform and its inversion we also consider some stability results for reconstruction in Sobolev spaces. We describe certain limited data problems and ways to tackle these, in particular the Two Step Hilbert reconstruction method. We then move on to photoelastic tomography, where we make use of techniques from scalar tomography to develop new methods for photoelastic tomographic reconstruction.

We present the main mathematical model used in photoelasticity, the Truncated Transverse Ray Transform (TTRT). After some initial numerical studies, we extend a recently presented reconstruction algorithm for the TTRT from the Schwartz class to certain Sobolev spaces. We also give some stability results for inversion in these spaces. Moving on from general reconstruction to focus on inversion of some special cases of tensors we consider solenoidal and potential tensor fields. We discuss existing reconstruction methods and present several novel reconstructions and discuss their advantages over using more general machinery. We also extend our new algorithms, as well as existing ones, to certain cases of data truncation.

Finally, we present numerical studies of the general reconstruction method. We give the first published results of TTRT reconstruction and go into some detail describing the implementation before presenting our results.

Declaration

No portion of the work referred to in this thesis has been submitted in support of an application for another degree or qualification of this or any other university or other institute of learning.

Copyright Statement

i. The author of this thesis (including any appendices and/or schedules to this thesis) owns any copyright in it (the "Copyright") and he has given The University of Manchester the right to use such Copyright for any administrative, promotional, educational and/or teaching purposes.

ii. Copies of this thesis, either in full or in extracts, may be made **only** in accordance with the regulations of the John Rylands University Library of Manchester. Details of these regulations may be obtained from the Librarian. This page must form part of any such copies made.

iii. The ownership of any patents, designs, trade marks and any and all other intellectual property rights except for the Copyright (the "Intellectual Property Rights") and any reproductions of copyright works, for example graphs and tables ("Reproductions"), which may be described in this thesis, may not be owned by the author and may be owned by third parties. Such Intellectual Property Rights and Reproductions cannot and must not be made available for use without the prior written permission of the owner(s) of the relevant Intellectual Property Rights and/or Reproductions.

iv. Further information on the conditions under which disclosure, publication and exploitation of this thesis, the Copyright and any Intellectual Property Rights and/or Reproductions described in it may take place is available from the Head of the School of Mathematics.

Acknowledgements

My first thanks, of course, go to Bill. Without your patience, guidance and encouragement this work would not have been possible. The enthusiasm with which you approach mathematics never ceases to amaze me and it has been a privilege to share this exciting world with you for the last five years.

Next, my family: my parents and my brother. For your never faltering, never questioning support in all my endeavours. For your love.

My colleagues and comrades in arms in the department. For showing me that finishing is possible. For friendship and fun, for the never ending stream of puzzles in times of boredom. Thank you.

Finally, to Ruth. For keeping me sane. For being there, always. For the final push across the finish line. Now new adventures await.

To each of you, my deepest gratitude.

Thank you.

Chapter 1

Introduction

In 1917 Johan Radon published his paper "On the definition of functions from the values on their integrals on certain manifolds"[1]. Little could he know that the subject of his investigations would come to underpin what has been described as "the most important invention in diagnostic radiology since the discovery of x-rays"[2]: x-ray computerized tomography (CT).

Of course, as often happens, the first practical implementations of x-ray CT by Godfrey Hounsfield in 1972 were completed without knowledge of Radon's work, rederiving the necessary equations for the application. Allan Cormack, who shared the 1979 Nobel Prize in medicine with Hounsfield was equally unaware of the previous work of Radon. Since its original invention, the x-ray CT field has developed and evolved, finding applications not only in medicine, but in areas ranging from palaeontology and nondestructive testing to geophysics and archaeology. Scanners have moved from single rows of x-ray detectors to entire arrays, and improvements in computer technology have allowed algorithm implementations to keep up with the ever increasing number of detectors. In the 1990s, scanning modalities moved from circular to the helical trajectories common today. One of the more unexpected consequences of this development is the new results in two-dimensional Radon transform inversion for limited data. Indeed, many of the recent results in the field are based

[1] Author's translation. Original title: Über die Bestimmung von Funktionen durch ihre Integralwerte längs gewisser Mannigfaltigkeiten.

[2] See e.g. [11]

on the exact reconstruction formula for helical CT presented by Katsevich in 2002. Considering the new inversion formula and letting the helical pitch tend to zero, led to the discovery of algorithms for local tomography such as the Two Step Hilbert transform by Noo et al. described in this thesis.

Photoelastic tomography is, compared to x-ray tomography, a much younger field. This is only natural, as rank two tensor fields lead to much more complicated relationships than the much simpler scalar field sought by x-ray CT. Two-dimensional "transmission" photoelasticity dates back to the end of the 19th century, but photoelastic tomography was not developed until the 1990s. Before then, the only way to make use of photoelastic measurements for three-dimensional objects was to carefully cut the specimen into thin slices and investigate each one. This method was extremely time-consuming, not to mention the fact that investigation destroyed the specimen. For these reasons, three-dimensional photoelasticity was largely abandoned.

Recent advances in photoelastic tomography show promise of once again making photoelasticity a viable option for non-destructive testing. Using knowledge and algorithms based on scalar tomography, new methodologies are being developed. In this thesis we will survey the landscape of scalar x-ray tomography and tensor field tomography. We present new theoretical developments for photoelastic tomography, including novel reconstruction algorithms for special types of tensor fields and new stability results for a recently developed algorithm. We also present the first results of numerical reconstructions using the aforementioned recent algorithm for photoelastic tomography, and note that this method is now ready for testing on real data. We give special attention to limited data problems. The phrase "limited data" is somewhat unfortunate as it is often reached for and used in a number of different contexts. For two-dimensional Radon transforms, restrictions to limited data are typically catastrophic, in the sense that a nullspace in the underlying operator is implied, and so full reconstructions are no longer possible. Typical practical situations include detectors too small to take all necessary data. In three dimensions, the situation is somewhat different. The reconstruction problem is dimensionally overdetermined, and certain forms of limited data may still allow full and exact reconstruction. Similar situations

occur in photoelastic tomography. We will refer to the former situation as *truncated data*, leaving the phrase *limited data* for cases when the limitation is not catastrophic. This distinction will become clear as the specifics of particular cases are described.

While our focus is on tomography of scalar fields and rank two tensor fields, we should also mention the thriving field of tomography of rank one tensor fields, usually referred to as vector tomography. Indeed, some of the results by Sharafutdinov used in this thesis are based on his earlier work on vector tomography. One of the main applications of this field is the determination of fluid velocities from tomographic acoustic measurements, but other applications include oceanography and nuclear magnetic resonance. For an overview of vector tomography see for example [26].

We give a brief outline of each chapter of this thesis, drawing attention to the main results.

In Chapter 2 we introduce the Radon transform and consider its inversion. We also present stability estimates and results for limited data problems, both of which we will make use of in later chapters to develop novel results for photoelastic tomography.

Chapter 3 gives an introduction to the mathematics of photoelasticity and photoelastic tomography. We present some initial numerical findings and describe the general reconstruction algorithm recently developed, encouraged by our numerical work. We also give new results extending the general algorithm to Sobolev spaces and considering its stability.

In Chapter 4 we consider some special types of tensors and present one existing and several new reconstruction algorithms for these special cases. Whilst only applicable to certain cases, these new algorithms allow for more efficient reconstructions. The new algorithms also have applications for certain types of truncated data.

In Chapter 5 we present our main numerical results. We describe the implementation of our forward model, the phantoms and simulated data, and finally results of reconstructions.

Finally, in Chapter 6 we summarise and give our thoughts on how to extend and continue this work.

Chapter 2

Tomography and the Radon Transform

2.1 Mathematical model

Before we begin our introduction to the mathematics describing the x-ray transform, we make some remarks about notation.

Definition 2.1. A function $\phi \in C^\infty(\mathbb{R}^n)$ is called an **open support test function** if for every $n, k \in \mathbb{N}$, $x^n \phi^{(k)}(x)$ is bounded as $x \to \pm\infty$. The space of open support test functions is known as the Schwartz space and is denoted by $\mathscr{S}$.

For a function $\phi \in \mathscr{S}(\mathbb{R}^n)$ we use the notation $\hat{\phi}$ and $\check{\phi}$ to denote the Fourier transform and its inverse, respectively, and use the following definitions:

$$\hat{\phi}(\omega) = (2\pi)^{-n/2} \int_{\mathbb{R}^n} e^{-ix\cdot\omega} \phi(x)\, dx \tag{2.1}$$

$$\check{\phi}(x) = (2\pi)^{-n/2} \int_{\mathbb{R}^n} e^{ix\cdot\omega} \phi(\omega)\, dx \tag{2.2}$$

For functions of several variables we sometimes only require partial Fourier transforms

or Fourier transforms in some of the variables. In this case we use the notation $\mathcal{F}_{p\to t}[g(\theta,p)]$ to indicate a Fourier transform in the p-variable only.

Lemma 2.2. *For $\phi \in \mathscr{S}$, we have both $\hat{\phi} \in \mathscr{S}$ and $\check{\phi} \in \mathscr{S}$*

Proof. See e.g. [23]. □

The mathematical model typically used in x-ray computerized tomography (CT) is to approximate the x-rays by lines, and ignore scattering, beam hardening and other physical effects. The main physical assumption is that the absorption of x-rays is proportional to the density of the object being x-rayed. We give here a brief introduction to the theory. For a more thorough treatment, see e.g. [17]. Let f be the density of some object being hit with x-rays. Typically f represents some finite object, and so we assume it to be *compactly supported*, that is equal to zero outside some bounded domain. If an x-ray beam of intensity I_0 enters the object, travels along the line L, and exits with intensity I, then

$$I = I_0 \exp\left[-\int_L f \; dl\right], \tag{2.3}$$

where dl is the measure on the line L. Typically, one considers as data not the measured values of the intensity I, but rather $g_L = -\ln(I_0/I)$. We then have

$$g_L = \int_L f \; dl. \tag{2.4}$$

The problem of computerized tomography is then to reconstruct f given g_L for all lines L passing through the support of f. As a purely theoretical exercise this problem was formulated long before the invention of x-ray CT. In 1917 Johann Radon published a paper [21] describing this problem, as well as a solution. For this reason, the integral operator (2.4) is known in the mathematical literature as the Radon transform of f, Rf. For a direction $\theta \in S^{n-1}$ and $p \in \mathbb{R}$ we have

$$R : \mathscr{S}(\mathbb{R}^n) \to \mathscr{S}(Z), \quad \text{with } Z = S^{n-1} \times \mathbb{R},$$

given by

$$Rf(\theta,p) = \int_{\theta^\perp} f(p\theta + y) \; dy. \tag{2.5}$$

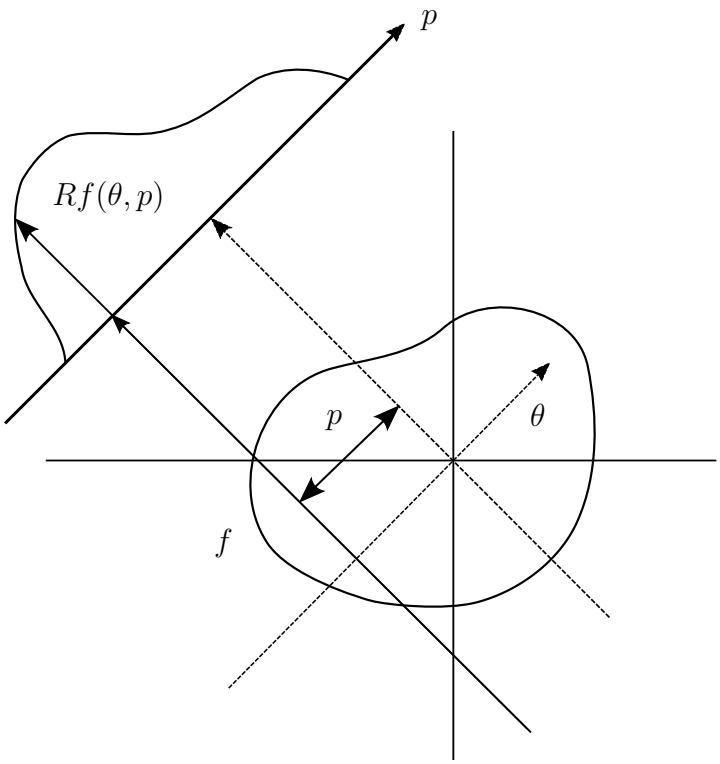

Figure 2.1: The Radon transform

See Figure 2.1 for a simple illustration of R.

For images f in $\mathbb{R}^2$, the Radon data lives on $S^1 \times \mathbb{R}$. Typically one only considers the subset $[0, \pi) \times \mathbb{R}$, since $Rf(\theta + \pi, p) = Rf(\theta, -p)$. This type of data is often referred to as a *sinogram*, due to the characteristic shape of the data for a delta function input, illustrated in Figure 2.2. Since the Radon transform is linear, sinograms from more complicated images, which can be thought of as a sum of delta measures, look like a very large number of sine waves all superimposed. The images in Figure 2.3 show a Shepp-Logan phantom, which is often used to test reconstruction algorithms, and its Radon transform.

The spaces $\mathscr{S}(\mathbb{R}^n)$ and $\mathscr{S}(Z)$ are equipped with the inner products

$$\langle f_1, f_2 \rangle = \langle f_1, f_2 \rangle_{\mathscr{S}(\mathbb{R}^n)} = \int_{\mathbb{R}^n} f_1(x) \overline{f_2(x)} \, dx \tag{2.6}$$

$$\langle g_1, g_2 \rangle = \langle g_1, g_2 \rangle_{\mathscr{S}(Z)} = \int_{S^{n-1}} \int_{\mathbb{R}} g_1(x) \overline{g_2(x)} \, dp \, d\theta, \tag{2.7}$$

where $\overline{f(x)}$ is the complex conjugate of $f(x)$.

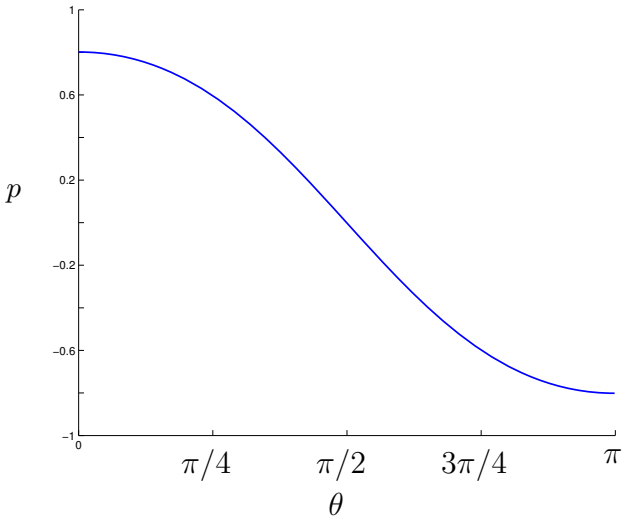

Figure 2.2: The sinogram of a delta measure at polar coordinates $(p, \phi) = (0.7, 0)$

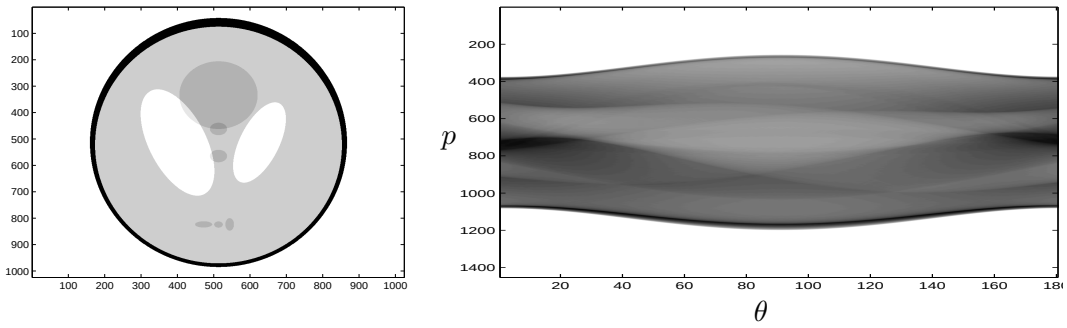

(a) Shepp-Logan phantom (b) A typical sinogram

Figure 2.3: Shepp-Logan phantom and its Radon transform

The **formal adjoint** operator $R^\#$ of R is given by

$$\langle Rf, g\rangle = \langle f, R^\# g\rangle. \tag{2.8}$$

since we only consider the Radon transform on real valued functions, we leave out the complex conjugation below. We thus have

$$\begin{aligned}\langle Rf, g\rangle &= \int_{S^{n-1}} \int_{\mathbb{R}} Rf(\theta, p) g(\theta, p)\, dp\, d\theta \\ &= \int_{S^{n-1}} \int_{\mathbb{R}} \int_{\theta^\perp} f(p\theta + y) g(\theta, p)\, dy\, dp\, d\theta\end{aligned}$$

Now, let $x = p\theta + y$, giving $p = x \cdot \theta$, and $dx = dp\ dy$, and so

$$\begin{aligned}\langle Rf, g\rangle &= \int_{S^{n-1}} \int_{\mathbb{R}^n} f(x) g(\theta, \theta \cdot x)\ dx\ d\theta \\ &= \int_{\mathbb{R}^n} f(x) \int_{S^{n-1}} g(\theta, \theta \cdot x)\ d\theta\ dx. \end{aligned} \tag{2.9}$$

Hence,

$$R^{\#} g = \int_{S^{n-1}} g(\theta, \theta \cdot x)\ d\theta. \tag{2.10}$$

The adjoint is also dual in a geometric sense: While the Radon transform integrates over all points on a given line (or hyperplane), $R^{\#}$ integrates over all lines (hyperplanes) through a point. This can be seen as "projecting back" the Radon data along the lines onto the image, and so the formal adjoint operator is known as **backprojection**.

2.2 Reconstruction

Today a wide range of applications involve the reconstruction of functions given information about their Radon transform. Below we outline the basic theory behind Radon transform inversion. We sometimes write $R_\theta f(p) = Rf(\theta, p)$.

2.2.1 The Fourier slice theorem

Theorem 2.3 (The Fourier slice theorem)**.** *Let $f \in \mathscr{S}(\mathbb{R}^n)$, $\theta \in S^{n-1}$, and $t \in \mathbb{R}$. Then*

$$\widehat{R_\theta f}(t) = (2\pi)^{(n-1)/2} \hat{f}(t\theta). \tag{2.11}$$

Note that since the Fourier transform is invertible, this proves that the Radon transform is also invertible.

Proof.

$$\begin{aligned}\widehat{R_\theta f}(t) &= (2\pi)^{-1/2} \int_{\mathbb{R}} e^{-ipt} R_\theta f(p)\ \ dp \\ &= (2\pi)^{-1/2} \int_{\mathbb{R}} e^{-ipt} \int_{\theta^\perp} f(p\theta + y)\ \ dy\ dp \end{aligned} \tag{2.12}$$

Now, let $x = p\theta + y$, giving $p = x \cdot \theta$, and $dx = dp\ dy$, and so

$$\begin{aligned} \widehat{R_\theta f}(t) &= (2\pi)^{-1/2} \int_{\mathbb{R}^n} e^{-it\theta \cdot x} f(x)\ dx \\ &= (2\pi)^{(n-1)/2} \hat{f}(t\theta) \end{aligned} \tag{2.13}$$

□

2.2.2 Filtered backprojection

The Fourier slice theorem shows that the Radon transform is invertible in principle, but it turns out to be a rather cumbersome algorithm to use in practice and this type of inversion is not widely used. Instead, some algebraic manipulation yields an equation much better suited for practical purposes. This algorithm is known as filtered backprojection.

For Radon data $Rf(\theta, p)$ we are only interested in Fourier transforms in the p variable, so we use the notation $\widehat{Rf}(\theta, p)$ to mean a Fourier transform in this variable only.

Definition 2.4. The **Riesz potential** I^α of a function f is given by

$$\widehat{I^\alpha[f]}(t) = |t|^{-\alpha} \hat{f}(t). \tag{2.14}$$

Theorem 2.5. *Let $f(x) \in \mathscr{S}(\mathbb{R}^n)$. Then for any $\alpha < n$ we have*

$$f = \tfrac{1}{2}(2\pi)^{1-n} I^{-\alpha} R^\# I^{\alpha-n+1} Rf. \tag{2.15}$$

Proof. Write

$$I^\alpha f(x) = (2\pi)^{-n/2} \int_{\mathbb{R}^n} e^{ix\cdot\omega} |\omega|^{-\alpha} \hat{f}(\omega)\ d\omega \tag{2.16}$$

We change to polar coordinates by letting $\omega = t\theta$, $t \in \mathbb{R}, \theta \in S^{n-1}$, giving

$$I^\alpha f(x) = (2\pi)^{-n/2} \int_{S^{n-1}} \int_0^\infty e^{itx\cdot\theta} |t|^{n-1-\alpha} \hat{f}(t\theta)\ dt\ d\theta \tag{2.17}$$

The Fourier Slice Theorem (2.3) then gives

$$I^\alpha f(x) = (2\pi)^{-n+1/2} \int_{S^{n-1}} \int_0^\infty e^{itx\cdot\theta} |t|^{n-1-\alpha} \widehat{Rf}(\theta, t)\ dt\ d\theta \tag{2.18}$$

Since $\widehat{Rf}(-t,-\theta) = \widehat{Rf}(t,\theta)$, we can replace t and θ in the above argument by $-t$ and $-\theta$, respectively to get the same equation with the inner integral over $(-\infty, 0)$, and adding the two gives

$$I^\alpha f(x) = \tfrac{1}{2}(2\pi)^{-n+1/2} \int_{S^{n-1}} \int_{-\infty}^{\infty} e^{itx\cdot\theta} |t|^{n-1-\alpha} \widehat{Rf}(\theta, t)\ dt\ d\theta \tag{2.19}$$

Using the definition of I^α again we have

$$\begin{aligned} I^\alpha f(x) &= \tfrac{1}{2}(2\pi)^{-n+1} \int_{S^{n-1}} I^{\alpha-n+1} Rf(\theta, x\cdot\theta)\ d\theta \\ &= \tfrac{1}{2}(2\pi)^{-n+1} R^\# I^{\alpha-n+1} Rf(x) \end{aligned} \tag{2.20}$$

and finally we apply $I^{-\alpha}$ to both sides, completing the proof. □

This establishes $\frac{1}{2}(2\pi)^{1-n} I^{-\alpha} R^\# I^{\alpha-n+1}$ as R^{-1}, and forms the basis for many practically used inversion algorithms. In 2D the most common form is $\alpha = 0$, in which case the leftmost filter is simply the identity, leaving a simple 1D filter on the right:

$$R^{-1} = \tfrac{1}{2}(2\pi)^{-1} R^\# I^{-1}. \tag{2.21}$$

This reconstruction is known as *Filtered Backprojection* (FBP) and lends itself to very efficient implementations, as the filter used is one-dimensional. Moreover, $I^{-1} g(\theta, p)$ is independent for each value of θ, and as data is often collected at one angle position at a time, the collected data may be filtered on the fly.

The filter I^α is often referred to as a *Ramp filter* due to the shape of the commonly used form I^{-1} in the Fourier domain, illustrated in Figure 2.4.

One other case will be of interest later, namely $\alpha = 1$ which is called *Backproject-then-filter* (BPF) as it only requires a filter on the image side:

$$\tfrac{1}{2}(2\pi)^{-1} I^{-1} R^\#. \tag{2.22}$$

Note that the backprojection operator is local, in the sense that to calculate the value of $R^\# g(x)$ at a given point x, only knowledge of the values of g at rays that meet x is needed. The filter I^α however, is only local for even integers α. For $n = 2$ at least one of the filters is non-local and this gives the inversion operator global dependence.

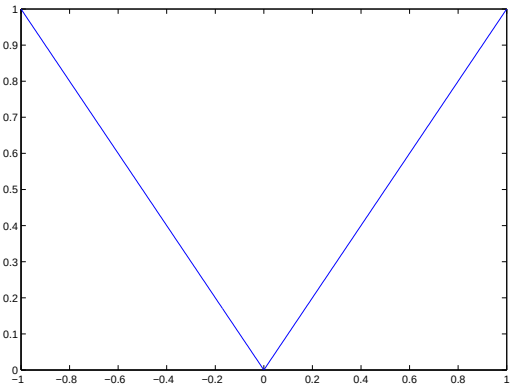

Figure 2.4: Ramp filter

2.2.3 Implementation issues

In practical situations there is always some level of noise present in the data. This is accentuated by a ramp filter, since high frequency components are amplified. To reduce the noise level we regularise the ramp filter by limiting the high frequency amplification. The simplest way to achieve this is to simply crop, or *window*, the filter beyond a certain absolute frequency. However, the sharp change can produce artefacts and better results are often achieved by smoothly rolling the filter down to zero. One way to do this is to use a Hamming window as defined by (2.23) below. The result of multiplying the ramp filter by a Hamming window is illustrated in Figure 2.5.

Definition 2.6. For a discrete signal of length N, labelled by $n = 0 \dots N-1$, the **Hamming window** $w(n)$ is given by

$$w(n) = 0.54 - 0.46 \cos\left(\frac{2\pi n}{N-1}\right) \tag{2.23}$$

The effect of using a Hamming window is illustrated in Figure 2.6. A small amount of random noise was added to the signal before applying a ramp filter, with and without a regularising Hamming window. The noise suppression is clearly visible.

2.2.4 Algebraic reconstruction techniques

Algebraic reconstruction techniques take a different approach compared to the analytic inversion algorithms described above. Here, the CT system is modelled using a

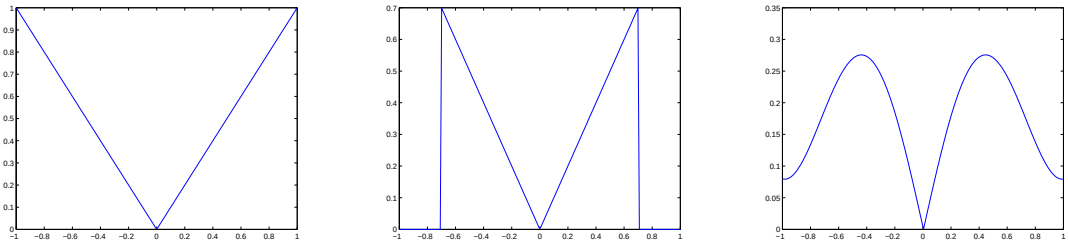

(a) Full ramp filter (b) Cropped at 0.7 (c) Hamming window

Figure 2.5: Ramp filter with various windows

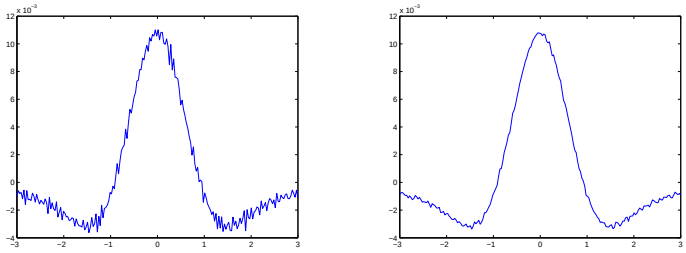

(a) Normal ramp filter (b) Regularised ramp filter

Figure 2.6: Ramp filter of e^{-x^2}

set of linear equations which are then solved simultaneously. In modern applications these systems are extremely large and iterative techniques are used. As a general rule these methods are much more computationally intense than FBP type algorithms, but in return they are more flexible and can often use better models of the physics involved in the x-ray system. We will mainly focus on exact, analytic reconstruction techniques for Radon transform inversion. We do make use of some algebraic inversion methods for photoelastic tomography and so we give a brief outline of the procedure here. The idea is to model the linear Radon transform as a matrix. We discretize both images and sinograms as vectors and construct a matrix to represent the operator corresponding to applying a Radon transform. More detail on the actual construction of such a matrix is given in Section 5.1. Once we have a matrix, the inversion simply amounts to inverting this matrix. In practice these matrices are too large to invert directly, and so iterative methods are used.

Below is an illustration of a reconstruction using the Conjugate Gradient Least Squares (CGLS) method from Hansen's Regularisation Tools [7]. Notice that CGLS

achieves a very good reconstruction in relatively few iterations. This is a regularized inverse, and so we expect some degree of smoothing out of features. The effect is particularly visible on the edges of the phantom.

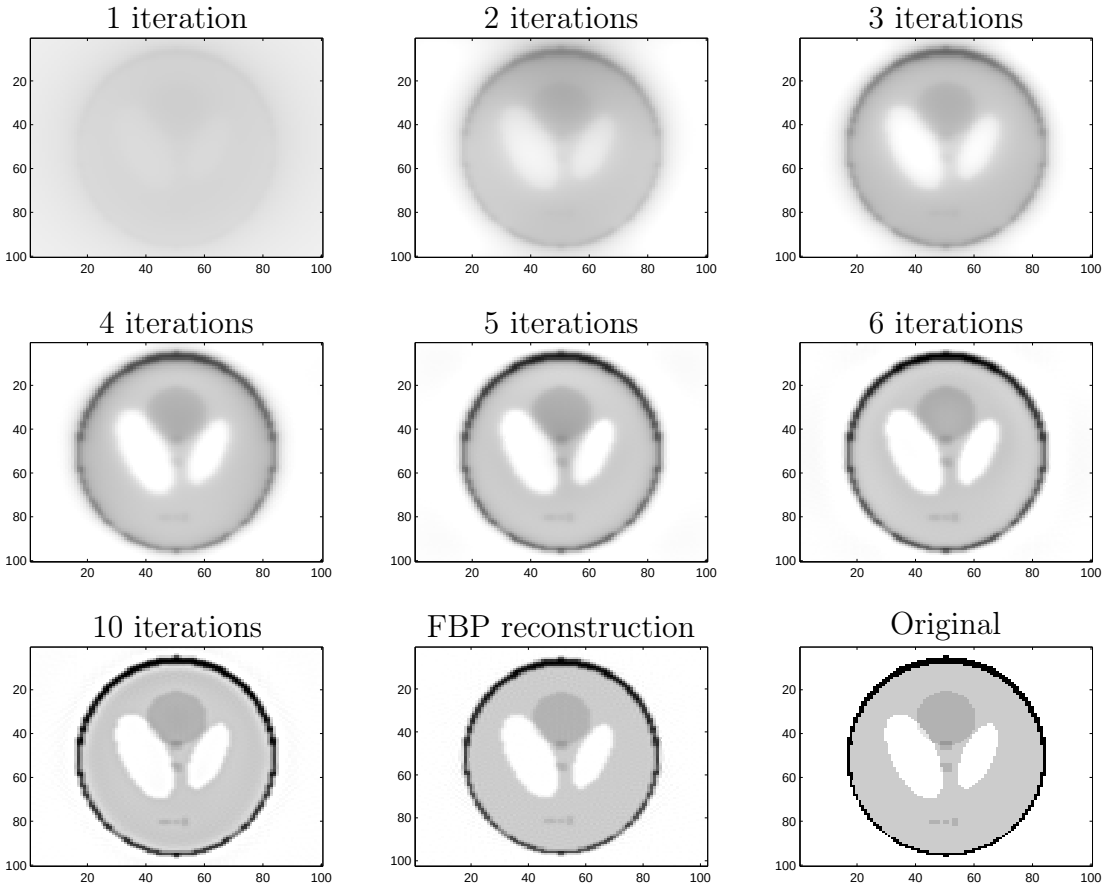

Figure 2.7: Algebraic Radon transform inversion

2.3 Stability estimates

To discuss the stability of the Radon transform we wish to consider it as an operator between suitable Sobolev spaces. For this investigation we restrict ourselves to functions supported in B_a, the ball of radius a in $\mathbb{R}^n$. This will clearly be the case in any practical situation.

Definition 2.7. The Sobolev space $H_0^s(B_a)$, $s \in \mathbb{R}$ is defined as the completion of

$C_0^\infty(B_a)$ in the norm of $H^s(\mathbb{R}^n)$, given by

$$||f||_s^2 = \int_{\mathbb{R}^n} (1 + |\omega|^2)^s |\hat{f}(\omega)|^2 \, d\omega. \tag{2.24}$$

Setting $s = 0$ gives the usual L^2 norm.

On the data side, we are interested in smoothness only in the p-direction, and so for $C_0^\infty(Z)$ we use the norm $|||\cdot|||_s$, given by

$$|||g|||_s^2 = \int_{S^1} \int_{\mathbb{R}} (1 + t^2)^s |\mathcal{F}_{p \to t} \, g(\theta, p)|^2 \, dt \, d\theta, \tag{2.25}$$

and denote the closure of $C_0^\infty(Z_a)$ by $H^s(Z_a)$. Here $Z_a = S^{n-1} \times [-a, a]$

Theorem 2.8. *Let $f \in H^s(B_a)$, with B_a the ball in $\mathbb{R}^n$. Then there exists a constant $c(s, n) > 0$ such that*

$$\frac{2\sqrt{\pi}}{(2\pi)^{n/2}} ||f||_s \leq |||Rf|||_{s+\frac{n-1}{2}} \leq c(s, n) ||f||_s \tag{2.26}$$

Proof. See e.g. [22], Theorem 2.4.1 □

Theorem 2.8 shows that the Radon transform increases smoothness by $\frac{n-1}{2}$ derivatives, as measured by the Sobolev norm. In addition, this shows that the Radon transform considered as a function from $H^s(B_a) \to H^{s+\frac{n-1}{2}}(Z_a)$ has a continuous inverse.

In practical situations we require no more than 3 dimensions, so we will restrict ourselves to this case. In fact, we are further restricted: Radon transform data, or indeed x-ray transform data, in 3 dimensions would require measurements from angles covering half the 2-sphere, which is somewhat impractical. It is much more convenient to consider our 3-dimensional object as a "stack" of 2D functions, as in Figure 2.8. The 2D Radon transform of each of these may be measured by a rotation around a single axis. For a given rotation angle, data from all slices may be collected at once, for example using a 2-dimensional detector, such as a CCD camera. We formalize this in the definitions below. We also extend the left hand inequality of (2.26) to 3D x-ray transforms, which we consider as a stack of 2D Radon transforms.

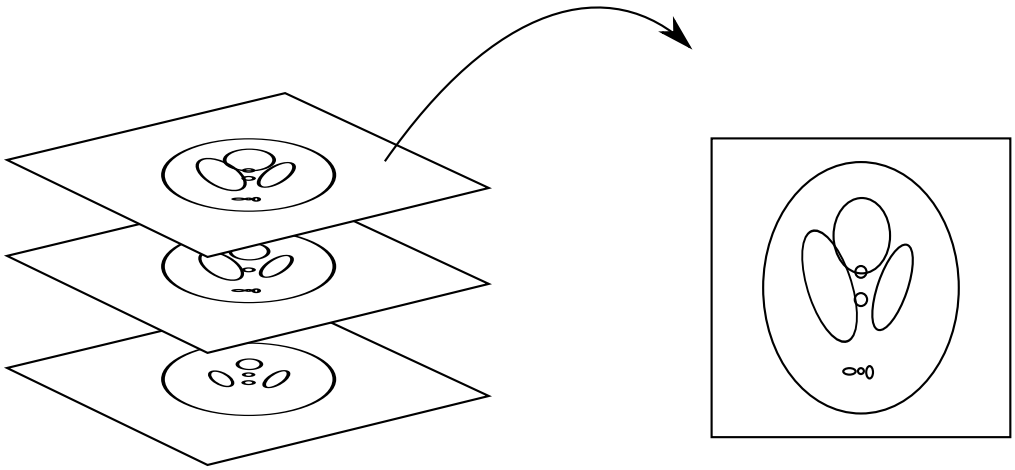

Figure 2.8: Each plane considered as a 2D function, for which we collect 2D Radon data

Definition 2.9. Consider $f(x)$ for $x \in \mathbb{R}^3 = \mathbb{R}^2 \times \mathbb{R}$ and write $f(y,z) = f_z(y)$, with $y \in \mathbb{R}^2$, and $z \in \mathbb{R}$. We then write the slice-by-slice Radon transform $\bar{R}$ as

$$\bar{R}f(\theta, p, z) = R[f_z(y)]. \tag{2.27}$$

For distributional $f \in \mathscr{S}'$, we define $\bar{R}$ by the action of a slice-by-slice backprojection $\bar{R^{\#}}$ on a test function ϕ:

$$\langle \bar{R}f, \phi \rangle = \langle f, \bar{R^{\#}}\phi \rangle \tag{2.28}$$

We define the Sobolev norm for slice-by-slice Radon data analogous to (2.25)

$$|||g|||_{\bar{s}}^2 = \int_{S^1} \int_{\mathbb{R}} \int_{\mathbb{R}} (1 + t^2 + \zeta^2)^s |\underset{z \to \zeta}{\mathcal{F}_{p \to t}} g(\theta, p, z)|^2 \, dt \, d\zeta \, d\theta, \tag{2.29}$$

along with the norm $H^{\bar{s}}$.

Clearly, $\bar{R}$ is bounded from $H^s \to H^{\bar{s}}$ for $s > 3/2$ by restriction followed by Theorem 2.25. At present we do not know the smallest value of s for which R is bounded however the following result shows the stability for the inverse for all s.

We shall require an extension of Theorem 2.8 for the slice-by-slice Radon transform. Unable to find the required result in the literature, we prove it here in the form of the following lemma:

Lemma 2.10. *Let $f \in H^s(B_a)$. Then*

$$||f||_s \leq (8\pi)^{-1/4} |||\bar{R}f|||_{\overline{s+\frac{1}{2}}} \tag{2.30}$$

Proof. We choose any $f \in C_0^\infty(B_a)$ and use the Fourier Slice Theorem for each slice to see that

$$\begin{aligned}
|||\bar{R}f|||^2_{\overline{s+\frac{1}{2}}} &= \int_{S^1}\int_{\mathbb{R}}\int_{\mathbb{R}} (1+t^2+\zeta^2)^{s+\frac{1}{2}} |\mathcal{F}_{\substack{p\to t \\ z\to\zeta}}\, Rf_z(\theta,p)|^2 \, dt \, d\zeta \, d\theta \\
&= \sqrt{2\pi}\int_{S^1}\int_{\mathbb{R}}\int_{\mathbb{R}} (1+t^2+\zeta^2)^{s+\frac{1}{2}} |\mathcal{F}_{z\to\zeta}\, \hat{f}_z(t\theta)|^2 \, dt \, d\zeta \, d\theta \\
&\geq 2\sqrt{2\pi}\int_{\mathbb{R}}\int_{S^1}\int_0^\infty t(1+t^2+\zeta^2)^s |\mathcal{F}_{z\to\zeta}\, \hat{f}_z(t\theta)|^2 \, dt \, d\theta \, d\zeta \\
&= 2\sqrt{2\pi}\int_{\mathbb{R}^3} (1+\omega^2)^s |\hat{f}(\omega)|^2 \, d\omega \\
&= 2\sqrt{2\pi}||f||_s^2.
\end{aligned} \tag{2.31}$$

□

We thus see that a slice-by-slice filtered backprojection, $\overline{\text{FBP}}$, defined in the obvious way, is a continuous map from $H^{\overline{s+\frac{1}{2}}}(Z_a^3)$ to $H^s(B_a)$

We have reviewed some stability results of the two-dimensional Radon transform, and extended these to a relevant special case of three-dimensional problems. In Section 3.6 we make use of these results to investigate the stability of a recently developed reconstruction algorithm for photoelastic tomography. But before moving on, we conclude our overview of the Radon transform by considering certain cases of missing data.

2.4 Limited data tomography

In many modern applications of x-ray CT, the size of the imaged specimen exceeds that of the detector array [9]. In the engineering community the problems associated with this are dealt with mainly on the experimental side, with methods like continuous image acquisition [12]. Much less emphasis has been put on the algorithm side

of development and often standard filtered backprojection is used even for truncated data. In the medical community there has been more of a drive towards new algorithms specially designed to deal with data truncation in both approximate and exact settings. We will consider some of the options available for dealing with truncated data.

2.4.1 Limited data tomography

The problem of tomographic reconstruction from only partial data is known as *limited data tomography*. Limited data here means the values of $Rf(\theta, p)$ are only known on some proper subset of the domain. One typically distinguishes between three types of limited data problems. In *limited angle* tomography, the data is, as the name suggests, only known for certain values of θ. This might occur in medical applications when a patient is attached to some apparatus, or in non-destructive testing when some views are obscured by some device used for live loading. *The exterior problem* concerns the case where the data $Rf(\theta, p)$ is known only for $|p| > a$ for some $a > 0$. Here one might be unable to measure rays going through the centre of the object, which may be too dense for the x-rays to penetrate. The final case, which is the focus of this section, is known as *the interior problem*. This involves, as described earlier, data of the form $Rf(\theta, p)$ for $|p| < a$, and some $a > 0$. The typical situation is a detector width too small to cover the entire object being scanned.

2.4.2 The interior problem and non-uniqueness

In the following sections we concentrate our attention to problems limited by detector width. We require some notation to aid our discussion. We shall also restrict our treatment to 2D. This includes the case of parallel x-ray 3D tomography, as each horizontal slice can be treated as an individual 2D problem. This setup is used for example at tomography beamlines at the European Synchrotron Radiation Facility (ESRF). Let $f \in \mathscr{S}(\mathbb{R}^2)$ be the object we wish to reconstruct. We assume f to be compactly supported and denote its support by Ω. Without loss of generality

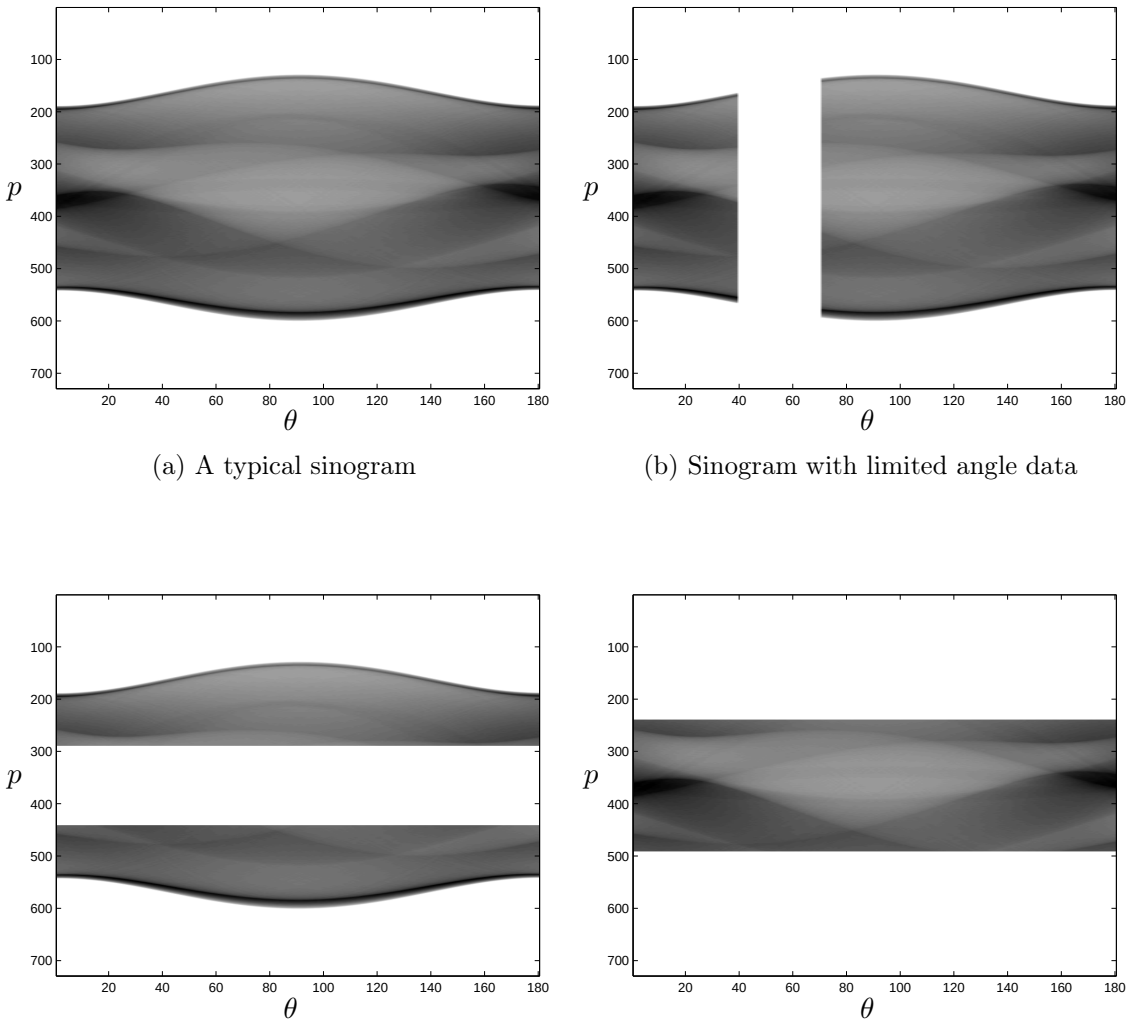

(a) A typical sinogram

(b) Sinogram with limited angle data

(c) Sinogram with exterior data

(d) Sinogram with interior data

Figure 2.9: Different types of limited data

we suppose that the object is rotated around some centre of rotation and that the source-detector pair is fixed, centered around the same centre of rotation. There will then be a circle determining the region of Ω that is illuminated by x-rays from all angles. We denote this region A, as shown in Figure 2.10.

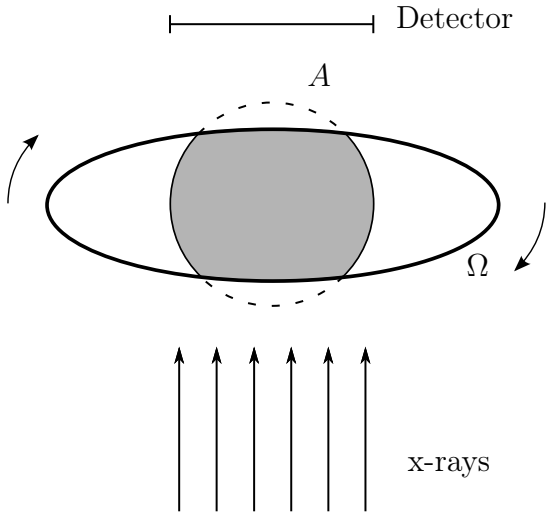

Figure 2.10: Region A

In this terminology, the *interior problem* above means that region A lies entirely inside Ω, that is, it does not contain any part of the boundary of Ω. If this is the case it is possible to prove that the measured truncated Radon transform no longer has a trivial nullspace. There are even compactly supported non-zero functions $f_0 \in \mathscr{S}(\mathbb{R}^n)$ such that $Rf|_{p<|a|} \equiv 0$. Natterer [17] gives an example. Note that a completely "invisible" object would have to take negative values, which is clearly not physically possible. However, the non-trivial nullspace does mean that unique reconstruction is no longer possible. . This is particularly useful in situations when detecting singularities, such as cracks, is of greatest interest. Later we shall see algorithms using this property.

2.4.3 Truncated filtered backprojection

If the sample is globally homogeneous and region A is in the centre of the specimen, some useful information can be recovered by applying the standard filtered backprojection (FBP) algorithm to the truncated data. Typically this yields reconstructions with strong artefacts near the regions of the image corresponding to edges of the detector, but it may still give some insight into the structure of f. Figure 2.11b shows the result of truncated FBP for a web phantom. The original image is shown in Figure 2.11a. For the purpose of illustration we show the image reconstructed on the whole original image space. When this method is used in practice, one typically only outputs the result inside region A. Note that the larger circle is a reconstruction artefact, and does not correspond to the middle circle in the original image, as can be seen from its location. The middle and outer original circles disappear almost completely. The edge artefacts arise due to the jump in the data from the last data value down to zero for unmeasured values. Since a ramp filter resembles a derivative, the large jump distorts the data. The location of this jump in the reconstructed image gives a good indication of the 'cut-off' value: the region inside is in full view of the detector at all times.

This artefact arising from the discontinuity at the detector edge can be alleviated by padding with the boundary value. Alternatively, one could try to smoothly round the data off to zero. There are various heuristic methods for doing this, including the "water cylinder" approach [8]. All these methods give very similar results and suffer from the same drawbacks. Figure 2.11c shows the image reconstructed using this method.

The use of the web phantom illustrates another important point. Outside region A, image features with different orientation are affected differently by data truncation. Essentially this is a limited angle problem, with more angles missing further away from region A. For the web phantom, the radial lines are reconstructed extremely well, whereas the circular features outside the fully illuminated region disappear almost completely. The reconstructed images may appear to provide information, when in

fact this information may be incomplete. Figure 2.12b is a physical phantom scanned with a synchrotron source at the ESRF, artificially truncated and then reconstructed using a padded FBP algorithm. The inner circle indicates the region illuminated from all angles, and the outer circle encloses the region illuminated by x-rays for at least 50% of the angles. The annulus region appears to contain information, and knowing that the original phantom consists of circles it is easy to see how and where the image is distorted. However, when imaging an unknown or more complicated object, it is not always clear which features are real and which are simply reconstruction artefacts. Figure 2.12a shows an example of how this information may be used. Region A is indicated by the dotted circle. Since images are almost always stored and displayed in rectangular shapes, and region A is circular, some of the incomplete data may be included, rather than leaving the corners empty, as long as the reader is aware of the difference.

2.4.4 Dual resolution tomography

Instead of simply using filtered backprojection on the truncated data, it may sometimes be possible to obtain some information about the whole specimen. If the limiting factor is the detector size, there is typically a trade-off between scanning the whole object at a lower resolution, or only a region at a higher resolution. Dual resolution tomography is an attempt to do both. The strategy is to take two or more sets of data for the same object using different magnification. Here at least one of the sets would cover the entire object, and subsequent sets would then be zoomed in on the region of interest. In cone beam systems, the magnification can be achieved by moving the specimen closer or further away from the source, and in parallel setups, where this is not possible, one can use lenses. In non-medical applications, x-ray dose is often not a concern and so multiple scans are less of a problem. There are different ways to combine the different data sets. In parallel beam regimes one could work only on the data side, by essentially replacing parts of the sinograms covering the whole object by the higher resolution data from the later scans. In fan beam or cone beam

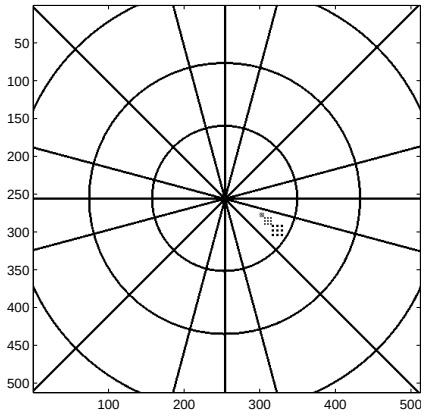

(a) Original phantom

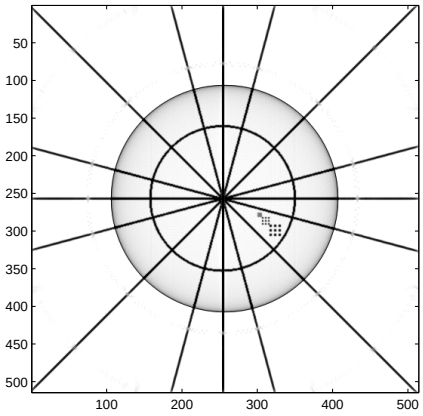

(b) Reconstructed from cropped data

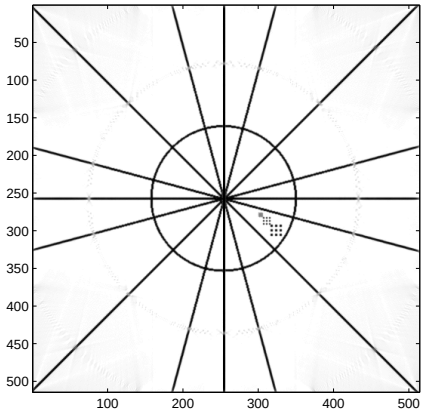

(c) Reconstructed from cropped data, padded with extreme values

Figure 2.11: The web phantom used to illustrate limited data artefacts

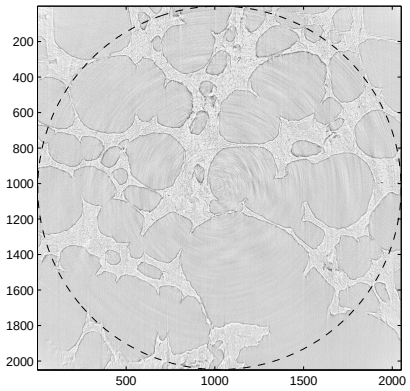

(a) A cracker

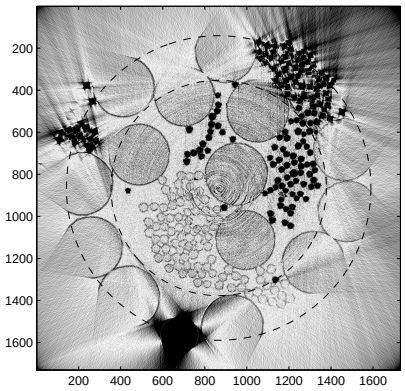

(b) A physical wire phantom

Figure 2.12: Two real examples

systems it is necessary to reconstruct an image using the full-view data, and then use this to generate higher resolution data for the regions outside region A. The latter approach is taken by Chun et. al in [4]. They carry out both numerical simulation and physical experiments, and also consider some of the effects of physical limitations, such as inaccuracies in the centre of rotation between the different measuring cycles. The images in Figure 2.13 show the result of applying this technique to the web phantom. We simulate two scans, the first one with a detector array covering the whole object, and the second using an array of half the width but with the same number of detectors. Note the improvement in resolution, which is clearly visible in the region south east of the centre, which consists of dots of various sizes. Using FBP based techniques means relatively low computations costs.

2.4.5 Two step Hilbert reconstruction

If we relax the degree of data truncation slightly, it is possible to achieve theoretically exact reconstruction for a large class of truncated data problems. If parts of region A lie outside Ω, any straight line inside A that intersects both edges of Ω can be reconstructed. See Figure 2.14, where the dotted line indicates the area inside the detector, and the shaded area can be reconstructed exactly, in spite of severe data truncation for certain angles.

The two step Hilbert method was first described by Noo et al. in [18]. The main practical advantage of the Hilbert transform method is its ability to reconstruct the actual attenuation values in situations with limited data. When using regular filtered backprojection this is not possible. From a theoretical viewpoint it is also very interesting to be able to achieve exact reconstructions from truncated data.

Definition 2.11. The *Hilbert transform* of f, $\mathcal{H}f$ is defined as a convolution with the kernel $\frac{1}{\pi p}$, that is

$$\mathcal{H}f(p) = pv \int_{-\infty}^{\infty} \frac{f(p-s')}{\pi s'} \; ds' = (2\pi)^{-1/2} \int_{-\infty}^{\infty} -i \operatorname{sgn}(t) e^{itp} \hat{f}(t) \; dt, \tag{2.32}$$

where pv indicates that the integral is understood in a Cauchy Principal value sense, and sgn denotes the *sign* function.

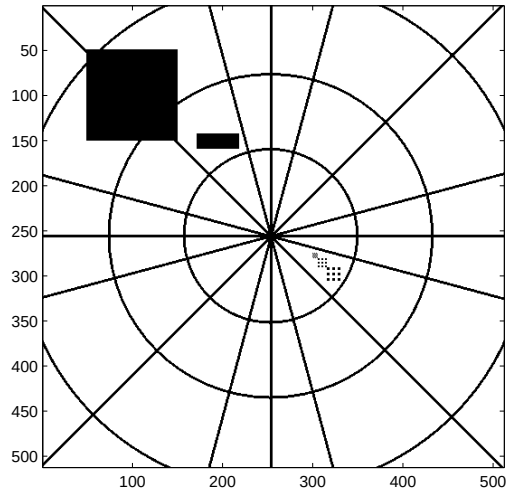

(a) Original phantom

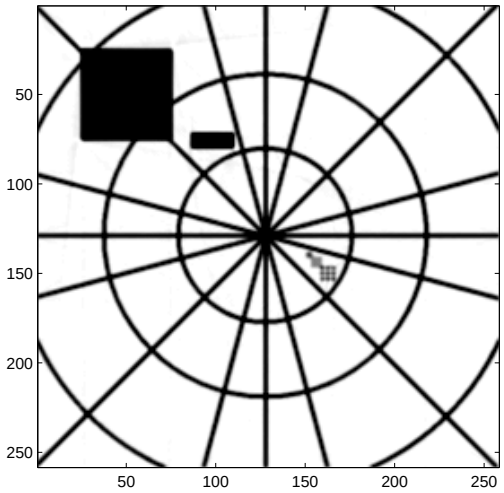

(b) Reconstruction from first scan data only

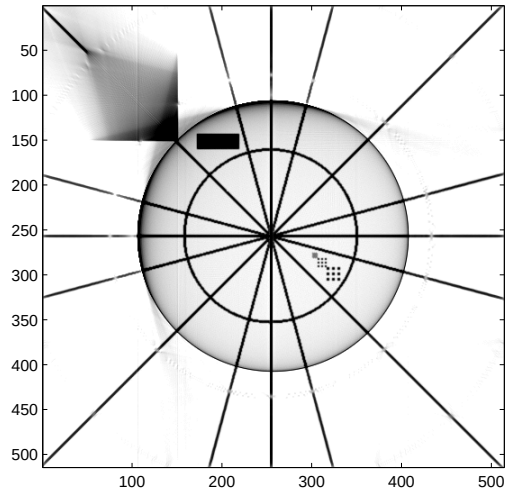

(c) Reconstruction from second scan data only

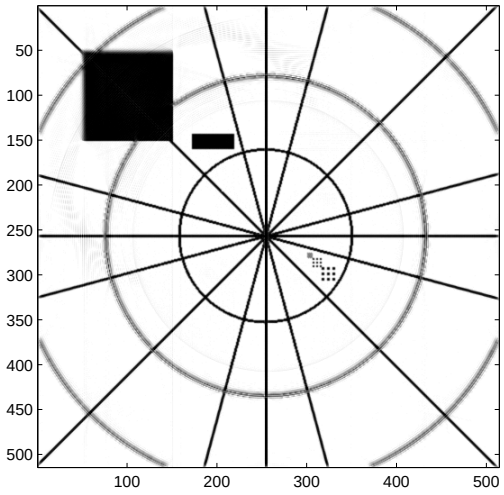

(d) Dual resolution reconstruction combining both data sets

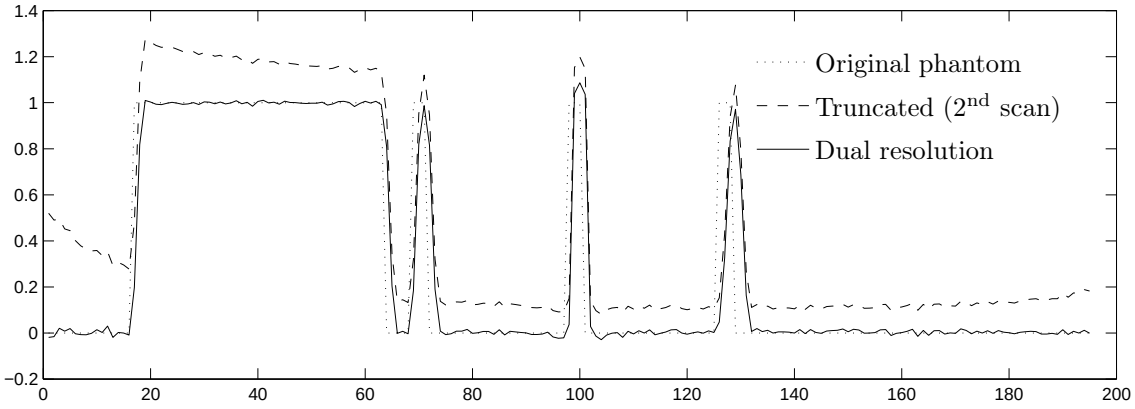

(e) Profile along 150th row, inside region A.

Figure 2.13: Dual resolution tomography

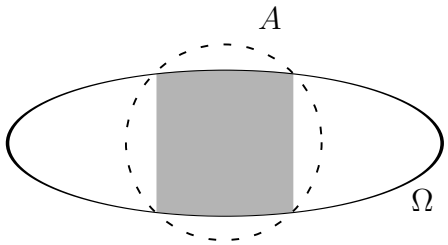

Figure 2.14: Reconstructible area using the two step Hilbert method

The Hilbert transform is intimately related to Radon transform inversion. The standard form of filtered backprojection uses a ramp filter, which is a multiplication by $|t|$ in the Fourier domain. This can be written as $|t| = (-it)\,(-i\,\mathrm{sgn}(t))$. A Fourier domain multiplication by $-it$ corresponds to a derivative in the spatial domain, and so a ramp filter can be decomposed into a differentiation followed by a Hilbert transform.

$$I^{-1}f(p) = \mathcal{H}\frac{\partial}{\partial p}f(p). \tag{2.33}$$

Since the derivative is a local operator, the non-local property of the Radon inversion is due to the Hilbert transform step.

We follow the notation of [18] and let $\mathcal{H}_0 f(x)$ denote a 2D function where a Hilbert transform has been applied in the second variable only, that is

$$\mathcal{H}_0 f(x_1, x_2) = pv \int_{-\infty}^{\infty} \frac{f(x_1, x_2 - x_2')}{\pi x_2'}\ dx_2' = pv \int_{-\infty}^{\infty} \frac{f(x_1, x_2')}{\pi(x_2 - x_2')}\ dx_2' \tag{2.34}$$

Lemma 2.12. *Let*

$$b_0 = \int_0^{\pi} \frac{d}{dp} Rf(\theta, p)\Big|_{p=x\cdot\theta}\ d\theta. \tag{2.35}$$

Then

$$b_0 = -\sqrt{2\pi}\mathcal{H}_0 f. \tag{2.36}$$

That is, first differentiating the Radon data in the p-direction and then backprojecting, gives the original image acted on by a Hilbert filter *in the x_2 direction*. It may, at first, seem strange that a particular direction is introduced in a seemingly rotationally symmetric procedure. The crucial point is the subset of angles which are backprojected. Radon data satisfies the symmetry relation $Rf(-\theta, -p) = Rf(\theta, p)$. When backprojecting over π radians, we are essentially backprojecting over the full

circle, and using redundancy. We note that the p-derivatives of the Radon transform are antisymmetric instead, and so when backprojecting it is no longer possible to backproject over the full circle, as the result would be zero. There is a choice of a parameter ϕ, where the backprojected angle range is $[\phi, \pi + \phi]$. In the lemma above we have $\phi = 0$ and a simple extension of the definition of b_0 to b_ϕ is possible, along with a corresponding definition of $\mathcal{H}_\phi$, Hilbert transforms along lines at an angle ϕ with the x_2 axis. We include the proof as we believe it is helpful in understanding the relationship between the Hilbert transform and Radon transform inversion.

Proof. We start with the definition of b_0, and write the derivative as a multiplication by $it = i|t|\operatorname{sgn}(t)$ in the Fourier domain.

$$\begin{aligned} b_0 &= \int_0^\pi \frac{d}{dp} Rf(\theta, p)\Big|_{p=x\cdot\theta} \, d\theta \\ &= (2\pi)^{-1/2} \int_0^\pi \int_{-\infty}^\infty ite^{i(x\cdot\theta)t} \widehat{Rf}(\theta, t) \, dt \, d\theta \\ &= (2\pi)^{-1/2} \int_0^\pi \int_{-\infty}^\infty i \operatorname{sgn}(t) e^{i(x\cdot\theta)t} \widehat{Rf}(\theta, t)|t| \, dt \, d\theta. \end{aligned} \tag{2.37}$$

We then use the Fourier slice theorem, and the fact that $\theta \in [0, \pi]$ means that $\sin\theta \geq 0$ and so $\operatorname{sgn}(t) = \operatorname{sgn}(t \sin\theta)$. We finally change variables to $\omega = t\theta$ and note that $t \sin\theta = \omega_2$.

$$\begin{aligned} b_0 &= (2\pi)^{-1/2} \int_0^\pi \int_{-\infty}^\infty i \operatorname{sgn}(t\sin\theta) e^{ix\cdot(t\theta)} \widehat{f}(\theta t)|t| \, dt \, d\theta \\ &= (2\pi)^{-1/2} \int_{-\infty}^\infty \int_{-\infty}^\infty i \operatorname{sgn}(\omega_2) e^{ix\cdot(\omega)} \widehat{f}(\omega) \, d\omega_1 \, d\omega_2 \\ &= -\sqrt{2\pi}\mathcal{H}_0 f. \end{aligned} \tag{2.38}$$

□

Thus, if we can invert the Hilbert transform, we have a new way of inverting the Radon transform. From the definition of the Hilbert transform in the Fourier domain, $\widehat{\mathcal{H}f}(p) = -i\,\mathrm{sgn}(p)\hat{f}(p)$ it is clear that it is its own inverse, up to a constant. The problem of inverting arises as even if f is compactly supported, $\mathcal{H}f$ may have unbounded support. As we can only recover a compact subset of b_0, some more machinery is needed. Formulae for inverting the Hilbert transform even in this setting have been known for a long time. We give one example due to Mikhlin [16, §26].

Proposition 2.13. *Let $f(t)$ be a function with support in $[L+\varepsilon, U-\varepsilon]$ for some $\varepsilon > 0$. Suppose $\mathcal{H}f(t)$ is known in $[L, U]$. Then*

$$f(t) = \frac{1}{\sqrt{(t-L)(t-U)}}\left(\int_L^U \frac{\sqrt{(p-L)(p-U)}\;\mathcal{H}f(p)}{\pi(p-t)}ds + C\right), \tag{2.39}$$

for some constant C, which in the tomography case is fixed by the integral of f, known from projection data.

Several other methods for finite Hilbert transform inversion have been suggested, in particular for dealing with the singularities near L and U. See e.g. [18, 31].

Figure 2.15 shows an example of using two step Hilbert reconstruction, compared to a regular FBP reconstruction. On the line plot, notice the FBP (dotted line) cupping, as well as giving the wrong attenuation level, both artefacts arising from the algorithm trying to compensate for the missing data from outside region A.

This completes our overview of the Radon transform and scalar tomography. We now move on to consider photoelasticity and tomography of tensor fields.

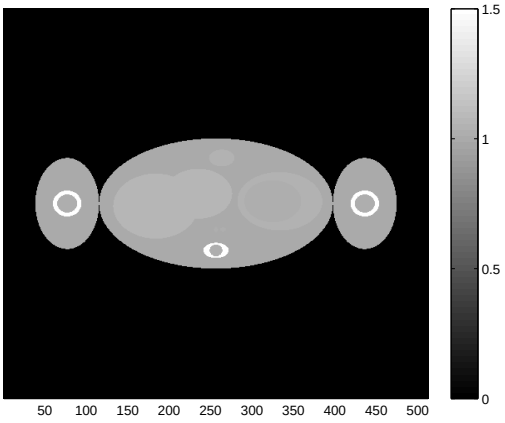

(a) Original phantom

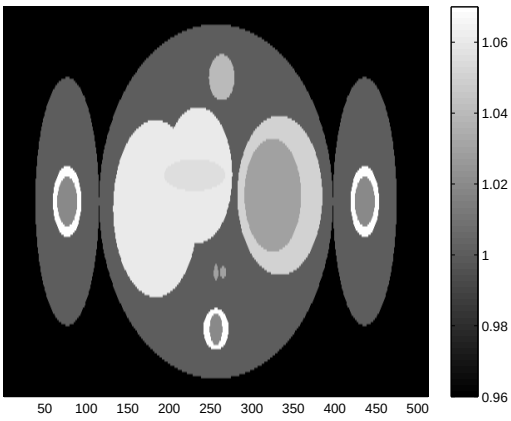

(b) Original, zoom and smaller display range

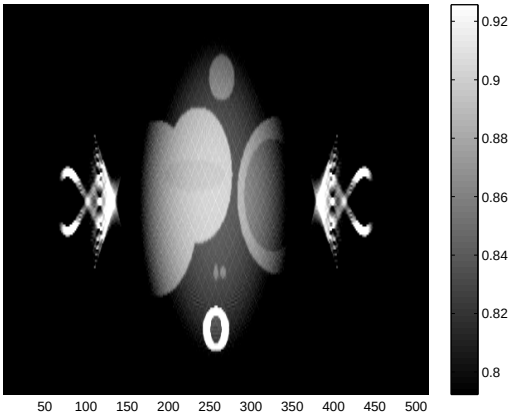

(c) Truncated FBP

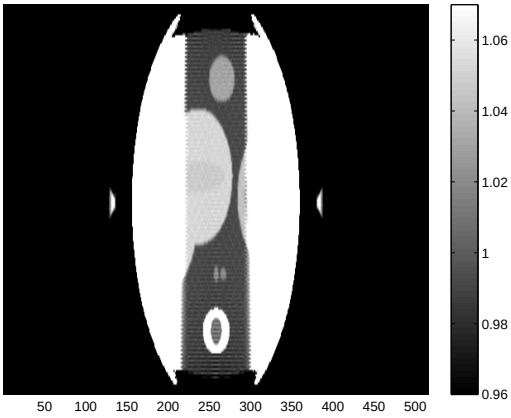

(d) DBP and Hilbert inversion

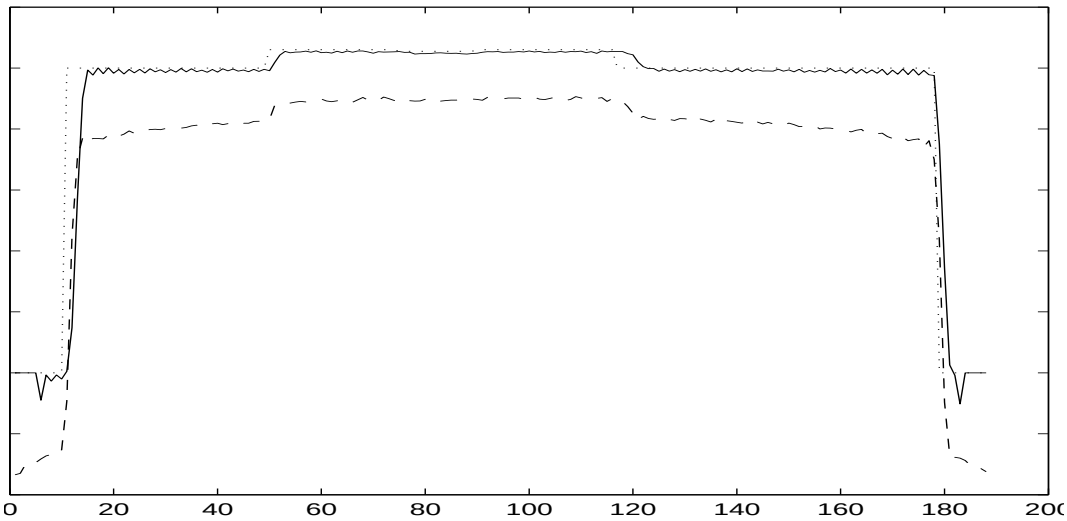

(e) Plot comparing original (dotted), FBP (dashed) and Hilbert inversion (solid)

Figure 2.15: Hilbert transform reconstruction

Chapter 3

Photoelasticity

In many situations in mechanical engineering it is of great importance to be able to predict the stress behaviour of solid components under load. Commonly today, a finite element model of the component is constructed and the stresses calculated using approximations to the partial differential equations. One major limitation of this approach is the importance of boundary conditions which may not be known, for example in cases of complicated contact between two surfaces such as a threaded nut and bolt. Photoelastic tomography overcomes this problem by recovering the stress experimentally.

Photoelasticity is the effect whereby the introduction of stress in certain transparent materials causes anisotropy in the otherwise isotropic permittivity, giving rise to birefringence. The optical anisotropy, which depends on the stress distribution within the material, may be measured using polarimetry [2, 30]. Assuming a low stress, the ordinary and extraordinary rays can be considered to be straight lines and to coincide, and the relationship between the anisotropic permittivity tensor and the stress can be assumed to be linear. This allows us to use tomographic techniques to recover the internal stress pattern of an object.

Figure 3.1: Epoxy resin cube with a point load, viewed through a polarizing filter [Image courtesy of Rachel Tomlinson, University of Sheffield]

3.1 Mathematical model

Before outlining the equations governing photoelasticity, we require some definitions. We will assume all coordinates to be Cartesian, and we will not distinguish between rank two tensors and matrices. Over $\mathbb{R}^3$ we identify a rank two symmetric tensor field with the matrix field

$$f = \begin{pmatrix} f_{11} & f_{12} & f_{13} \\ f_{12} & f_{22} & f_{23} \\ f_{13} & f_{22} & f_{33} \end{pmatrix}, \tag{3.1}$$

with the *components* f_{ij}.

Using terminology from the theory of elasticity we define a unique splitting of matrices into trace and trace-free parts.

Definition 3.1. Let f be a symmetric 3×3 matrix f. The *deviatoric*, or trace-free,

part of f $\mathbf{D}f$ is given by

$$\mathbf{D}f = f - \tfrac{1}{3}\operatorname{Tr}(f)I_3, \tag{3.2}$$

where Tr denotes the trace of f and I_3 is the identity matrix. Similarly, we have the isotropic, or in terminology from elasticity, the *hydrostatic* part of f, $\mathbf{H}f$ given by

$$\mathbf{H}f = \tfrac{1}{3}\operatorname{Tr}(f)I_3. \tag{3.3}$$

Symmetric tensors can be uniquely decomposed into deviatoric and isotropic parts $f = \mathbf{H}f + \mathbf{D}f$, and in the absence of any intrinsic directions in f, this decomposition is respected by linear equations. That is, any linear equation of f may be written as

$$L[f] = d\mathbf{D}(f) + h\mathbf{H}(f) \qquad \text{for some constants } d \text{ and } h. \tag{3.4}$$

This is a classical result in the tensor literature and may be proved by direct calculation [20].

The stress optic law proposes that the permittivity tensor depends linearly on the stress tensor [13, §16]. In the remainder of our study of photoelasticity, we shall assume that the forces involved are small enough to assume linear relationships in the equations governing strain, stress and permittivity. We also consider materials without intrinsic directions and so the dependence of the permittivity ϵ on stress σ must also preserve the splitting into deviatoric and potential parts.

$$\epsilon = C_0\mathbf{D}(\sigma) + C_1\mathbf{H}(\sigma), \tag{3.5}$$

where C_0 and C_1 are material-dependent constants.

The isotropic part of the permittivity is very difficult to recover using polarimetry, as it essentially involves measuring path lengths of light rays accurate to fractions of a wavelength. It is also the case in many applications that only the deviatoric part is of interest, and so the literature often only quotes one photoelastic constant, $C = C_0$.

This is particularly common when studying ductile materials such as metals. The von Mises yield criterion, which is a measure of when such a material begins to yield is defined in terms of the difference of the principal stresses. For a stress tensor with

eigenvalues λ_i, von Mises stress J is defined as

$$J = \sqrt{\frac{1}{2}\sum_{i \neq j}(\lambda_i - \lambda_j)^2}\ , \tag{3.6}$$

which clearly only depends on the deviatoric stress.

Considering only the deviatoric part and thus using only one constant also makes it possible to convert results between different materials. One is able to use a transparent photoelastic material such as epoxy resin and construct a model for an engineering component originally made from metal. This becomes a simple matter of rescaling results according to the photoelastic constants.

3.1.1 Ray approximation

An approximation to Maxwell's equations known as the Rytov-Kravtsov law is used to model the light propagation through the photoelastic medium. For a full derivation see e.g. [24, Ch. 5]. The anisotropy and its derivatives are assumed to be small, $\epsilon = \epsilon_0 I + f$ for some constant ϵ_0 and a small f. This leads to the approximation described below where, in particular, the ordinary and extraordinary rays are straight coinciding lines. We parameterize the space of rays (that is, lines with orientation) $L = L(\xi, x)$ in $\mathbb{R}^3$ by a unit vector ξ giving the direction of a line, and the point on the line closest to the origin x, which satisfies the inner product $\langle \xi, x \rangle = 0$. For a unit vector ξ we define P_ξ to be the projection of a vector in $\mathbb{R}^3$ onto the space perpendicular to ξ, and extend P_ξ to be defined for arbitrary symmetric matrices. To do this, we think of the symmetric matrix A as a bilinear form where

$$P_\xi(A)(u, v) = A(P_\xi u, P_\xi v), \tag{3.7}$$

or, writing P_ξ as a matrix, we have

$$P_\xi(A) = P_\xi^T A P_\xi. \tag{3.8}$$

For a vector v we have $P_\xi(v) = v - (v \cdot \xi)\xi$ and for example with $\xi = e_2 = (0, 1, 0)$

and the matrix f,

$$P_\xi(f) = \begin{pmatrix} f_{11} & 0 & f_{13} \\ 0 & 0 & 0 \\ f_{13} & 0 & f_{33} \end{pmatrix}. \tag{3.9}$$

The Rytov-Kravtsov law then states that for the electric field E and t measuring distance along the ray,

$$\frac{dE}{dt} = \frac{i}{2\epsilon_0} P_\xi(f) E, \tag{3.10}$$

where E is the electric vector.

The solution operator to the initial value problem $E(t) = U(t)E(t_0)$ is expanded as a Neumann series

$$U = I + \int_{t_0}^{t} \frac{i}{2\epsilon_0} P_\xi f(t_1)\ dt_1 + \int_{t_0}^{t} dt_1\ \frac{i}{2\epsilon_0} P_\xi f(t_1) \int_{t_0}^{t_1} dt_2\ \frac{i}{2\epsilon_0} P_\xi f(t_2) + \dots \tag{3.11}$$

and truncated to first order to form the linear approximation Sharafutdinov calls the *Transverse Ray Transform (TRT)* of f along the ray $x + \xi t \in L$,

$$TRTf(\xi, x) = \int_{-\infty}^{\infty} P_\xi f(x + t\xi)\ dt \tag{3.12}$$

As mentioned above, effects of the hydrostatic parts of f are very difficult to measure. Instead it is often only possible to measure integrals of a related operator, the *Truncated Transverse Ray Transform* (TTRT) [24, Ch 6], given by

$$Kf(\xi, x) = \int_{L(\xi,x)} Q_\xi(f)\ dt \tag{3.13}$$

with

$$Q_\xi = \mathbf{D} P_\xi \tag{3.14}$$

which in the example of (3.1) gives

$$Q_\xi(f) = \frac{1}{2} \begin{pmatrix} f_{11} - f_{33} & 0 & 2f_{13} \\ 0 & 0 & 0 \\ 2f_{13} & 0 & f_{33} - f_{11} \end{pmatrix}. \tag{3.15}$$

Here, $Kf(\xi, x)$ may be measured using polarimetry for each ray (ξ, x).

Since scalar multiples of the identity matrix field are in the nullspace of the TTRT, from now on we only consider reconstruction of trace free matrix fields. That is, f will be assumed to satisfy $\mathbf{H}f = 0$.

3.2 Photoelastic tomography

In contrast to conventional tomography, where a scalar field is reconstructed, photoelastic tomography involves the recovery of a rank two symmetric tensor field from integrals along lines of the projection of the tensor field onto planes normal to the lines. The interaction with the light rays is more involved, and the inversion is much more complicated.

We restrict our consideration to methods that recover the stress in a static object. Other inversion techniques include the *Load Incremental* approach developed by Wijerathne et al. [29]. As the name suggests this method involves taking measurements of a specimen under increasing load and this type of method is not considered in this thesis.

A possible experimental setup for the collection of TTRT data is being developed in collaboration with the University of Sheffield [14, 27, 30].

The experimental system uses a specimen constructed from birefringent epoxy resin. Objects are placed on a rotation stage inside a glass tank filled with fluid matching the refractive index of the epoxy, and illuminated by a laser. The laser light passes through a polarizer, the glass tank and finally an analyser before being measured by a CCD camera. Additional optical apparatus may be put in place to filter out scattered light rays, should this be deemed necessary. A technique known as Fourier polarimetry [30] is used to recover TTRT data from the measured light intensity. The specimen is rotated to collect tomographic data, and may be replaced at a different orientation relative to the rotation stage to collect data for various axes of rotation. Figure 3.2 illustrates the experimental setup.

We thus have the following problem definitions for our forward and inverse problems: Given a 3-dimensional rank two symmetric tensor field and a line $L(\xi, x)$, the

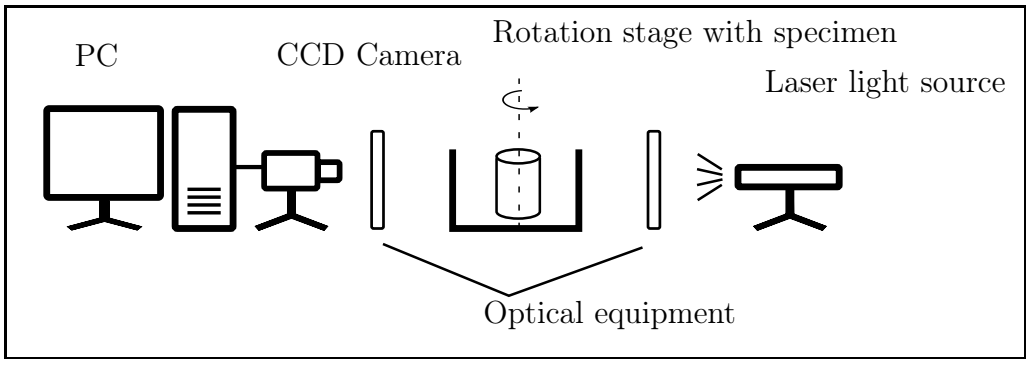

Figure 3.2: Possible experimental setup

data we collect is

$$Kf(\xi, x). \tag{3.16}$$

Now, given $Kf(\xi, x)$ for some family of lines, we wish to recover Df.

Our first step is to find some collections of lines which may feasibly be collected while still being enough to uniquely determine f.

It is somewhat impractical to collect data for *all* possible lines (even when excluding lines that do not intersect the support of f) and a simple heuristic argument shows that this may not be necessary. The space L of all lines in $\mathbb{R}^3$ is 4-dimensional, whereas the sought f is a function of only 3 variables, and so it seems plausible to expect that only a 3-dimensional family of lines would be needed for the recovery of f. Indeed, a recent paper [15] proves uniqueness and provides an unstable reconstruction algorithm using only lines parallel to 3 planes and a stable reconstruction algorithm using lines parallel to 6 planes.

3.2.1 Reconstruction: historical background

When we began our investigations into photoelastic reconstruction, the field looked very different compared to today. While the cutting edge of experimental photoelastic reconstruction still belongs to the group of Aben et al. [1, 2] now as it did then, much progress has been made on the theoretical side. The papers by Aben contain a basic derivation of the reconstruction algorithm used, mainly appealing to physical principles and a balance of forces. These investigations inspired Vladimir

Sharafutdinov to conduct a more thorough mathematical investigation into the subject and, in true mathematical style, in much more generality. In the preface to his book on the subject [24] he gives the following apology:

> I am not sure that this book will gain a wide readership. A pure mathematician would most likely consider it rather old-fashioned that the book is abundant in cumbersome calculations performed in coordinate form with use made of multilevel indeces. [...] On the other hand, an applied mathematician will likely be confused by vector bundles, Riemannian connections and Sobolev's spaces.

Both the reconstructions presented by Aben et al. and Sharafutdinov are for the recovery of only one component of the tensor field using data from rays parallel to a single plane. Sharafutdinov also presents a formula in his book for calculating the complete tensor, but this requires a practically infeasible amount of data, captured from rays in all possible directions in $\mathbb{R}^3$.

In 2004 Hammer and Lionheart began investigating the possibility of combining multiple one-component reconstructions to find the full stress tensor [6]. This is where the current author started his journey into photoelastic tomography and where this work takes its start.

3.2.2 Multiple axes of rotation

Our first approach to this problem is to consider algebraic methods. Instead of calculating each tensor component separately, this methodology enables us to calculate them all at once. An algebraic model of the problem also allows numerical analysis of the model itself, to investigate the feasibility of reconstructions from varying amounts of data. While it is clear that tomographic data collected using six different axes of rotation and six separate reconstructions are enough, it may be possible to achieve reconstruction using less data. Finally, using algebraic techniques allows a more explicit approach to regularisation as we shall see later. As is typical in inverse problems, quite some effort is required to construct an accurate numerical forward

model. In addition to above, the forward model will also serve as a source of simulated data for the testing of later analytical reconstructions.

3.3 Investigation of the forward model

The full description of the forward model is given in Section 5.1. For the following we will assume access to a linear forward model. The model takes the form of a sparse matrix representing the operator taking a three dimensional strain tensor field to photoelastic measurement images. In practice this matrix is far too large to fit in RAM at once, so we typically generate parts of it on the fly, as needed by our various algorithms. We focus our initial investigation on this matrix, estimating its rank and attempting reconstruction using the algebraic methods described in Section 2.2.4.

3.3.1 Rank estimation

We use a Singular Value Decomposition (SVD) to estimate the rank of the model matrix, varying the number of angle steps in the rotation around each axis, as well as the total number of axes. Even on small scales, the complete matrix becomes too large to calculate the SVD, so very coarse grids need to be used.

We discretize our tensor field into $18 \times 18 \times 18$ voxels. Using the forward model, we construct a complete matrix M representing the TTRT operator, and calculate its SVD. We simulate a digital camera with 30×40 pixels, and use 60 projections. To compare different data acquisition modalities, we split the 60 projections over one or several axes of rotation. The theory indicates that using 6 axes will be sufficient to recover the deviatoric part of the tensor field (5 values for each voxel). The heuristic argument based on dimensionality suggests that 3 axes may be enough.

Looking at the plot of the singular values in Figure 3.3a, the matrix rank certainly appears to match the expected 5 values per voxel. Recall that the symmetric tensor field has 6 independent values, but its trace is in the nullspace of the TTRT.

We may investigate the singular vectors corresponding to the zero (within numerical tolerance) singular vectors. Considering the span of these vectors and using

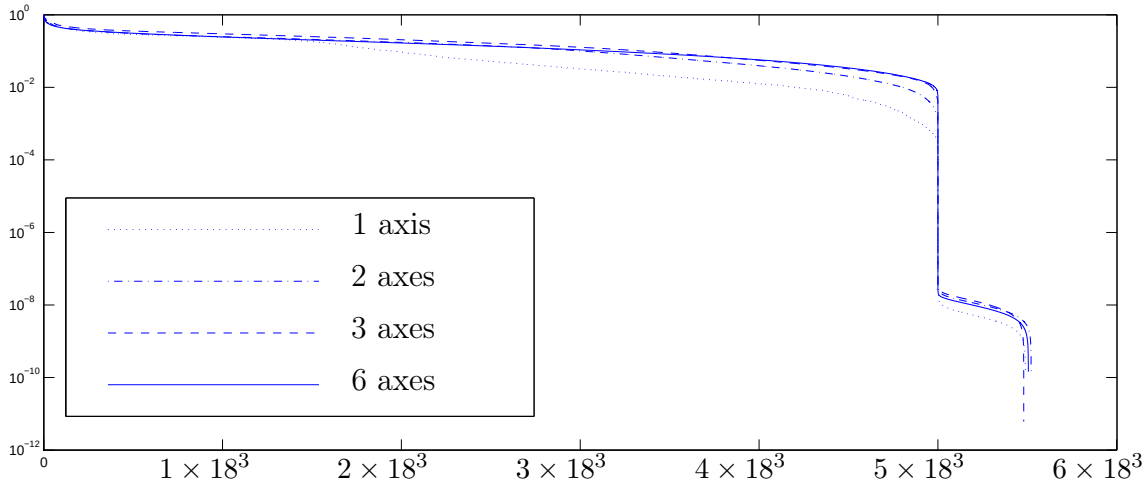

(a) Log scale

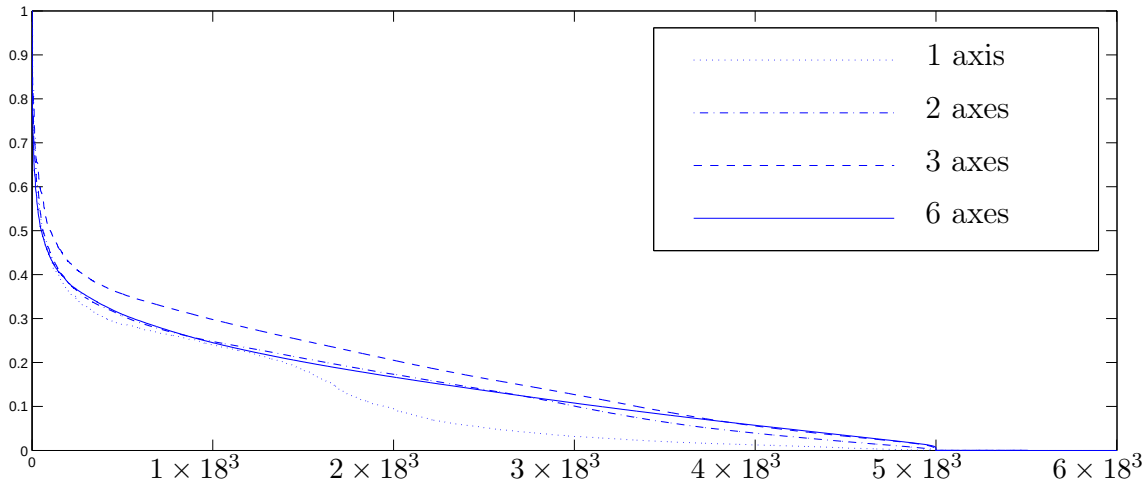

(b) Normal scale

Figure 3.3: The singular values of M plotted for 1,2,3, and 6 axes of rotation

Matlab to calculate a canonical basis, it is clear from Figure 3.4 that these do indeed correspond to the tensor trace in each voxel. The symmetric matrices have 6 independent values and are stored in the order $(f_{11}, f_{12}, f_{13}, f_{22}, f_{23}, f_{33})$, so in each voxel, the trace is the sum of the first, fourth and sixth values. The figure shows the case for 1 axis; 2, 3, and 6 axes give the same result.

Interestingly, the plot of the singular values for different number of axes appears to indicate that the nullspace is limited to the hydrostatic part of the tensor field even for a single axis of rotation. For 1 axis, the singular values decrease by several orders of magnitude, as may be seen in Figure 3.3b, but the main drop is still at 5 values per voxel. However, as we shall see, attempting a reconstruction from single

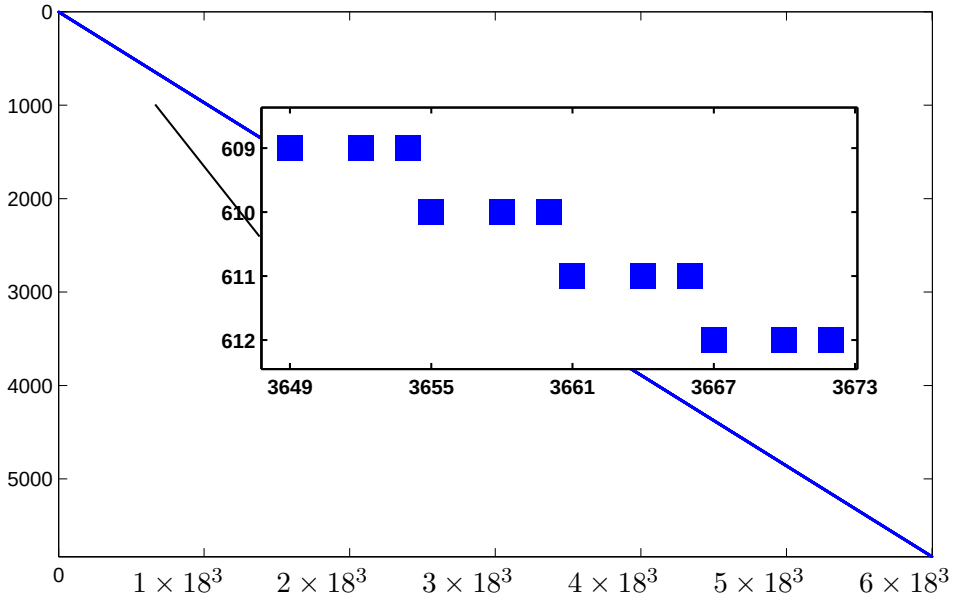

Figure 3.4: A basis for the nullspace of the TTRT

axis data does indicate the presence of a larger nullspace.

Figures 3.5 – 3.10 show a CGLS reconstruction of f from data collected using 1,2,3, and 6 axes of rotation. The phantom used is Phantom 2, defined in Section 5.2.2. Due to the computational intensity, the grid size was restricted to $30 \times 30 \times 30$. 1080 views were used, split over the varying number of rotation axes in order to use the same amount of data for all reconstructions.

The artefacts visible in the 2-axis reconstruction may indicate the presence of a nullspace beyond the hydrostatic part of the tensor. The reconstruction from data from a single axis appears to fail almost completely, and only recovers partial structures while suffering from large artefacts. Indeed, for the 1-axis case it is possible to calculate an explicit family of tensors in the nullspace of the TTRT. We defer the calculation of such tensors until Section 3.5, at which point we will have developed some more helpful tools.

Considering the reconstructions for 3 and 6 axes, the results from these numerical investigations provide a positive indication that a complete reconstruction is in fact possible from data limited to rays parallel to a small number of planes. Such an algorithm was indeed found by Sharafutdinov and Lionheart in 2009.

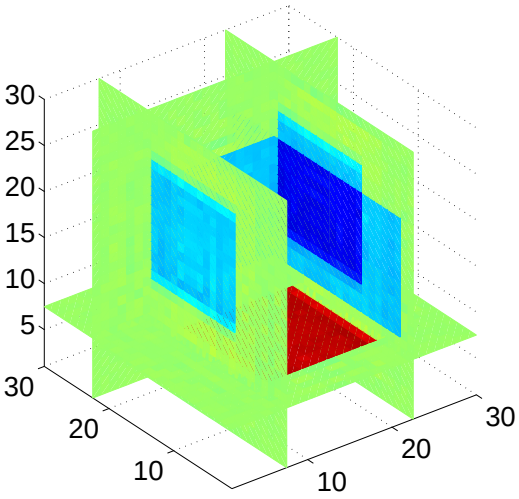

(a) Using 6 axes

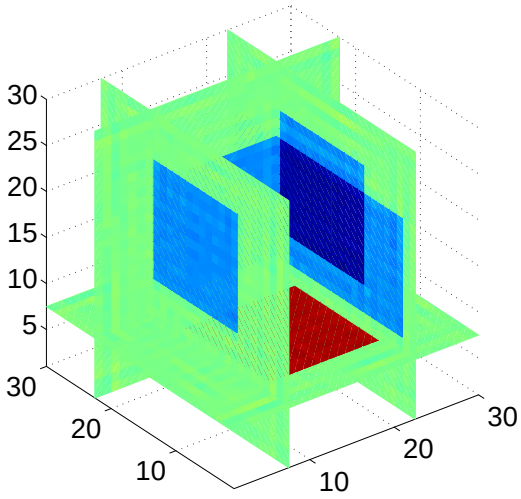

(b) Using 3 axes

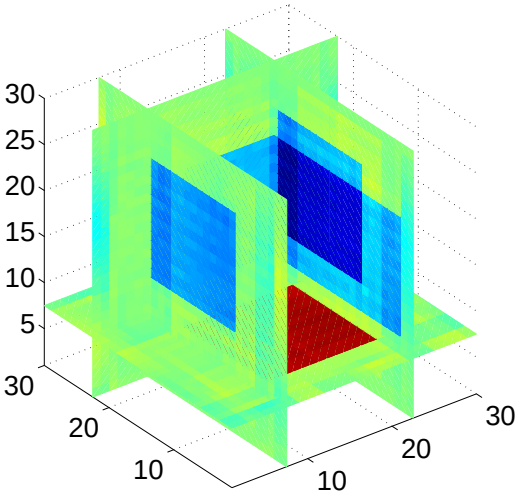

(c) Using 2 axes

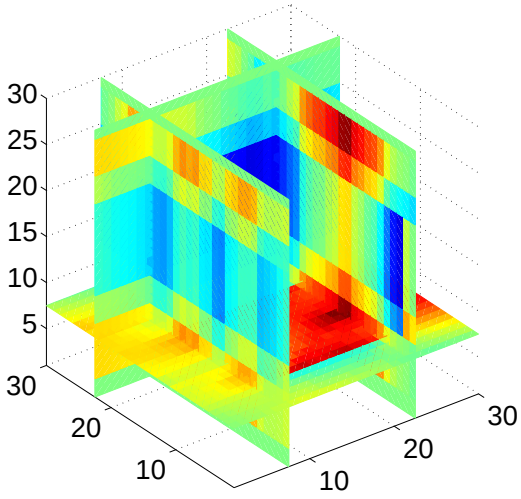

(d) Using 1 axis

Figure 3.5: Algebraic reconstruction of f_{11}

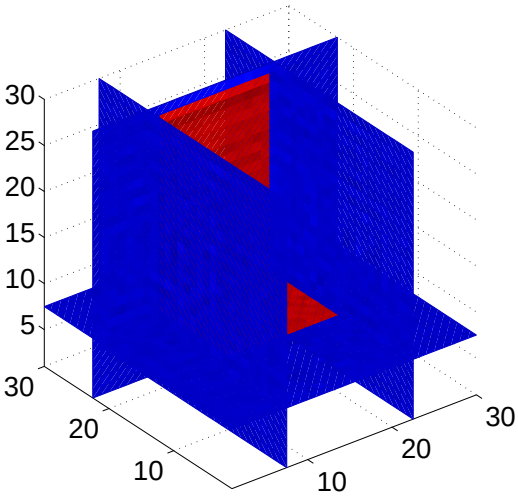

(a) Using 6 axes

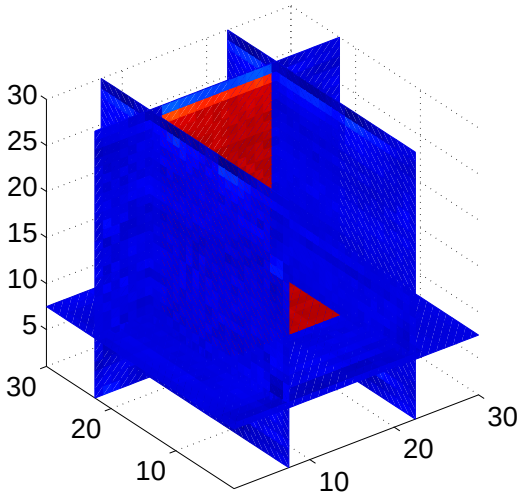

(b) Using 3 axes

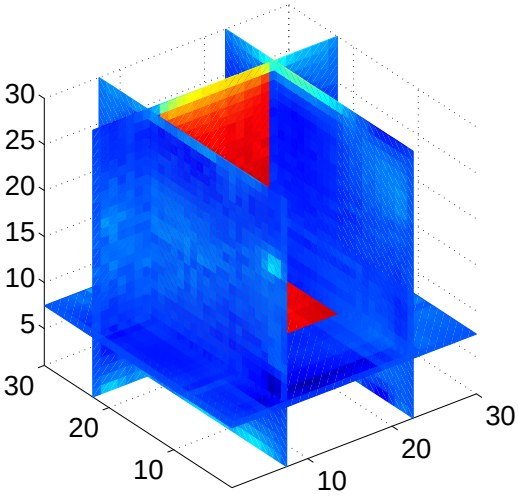

(c) Using 2 axes

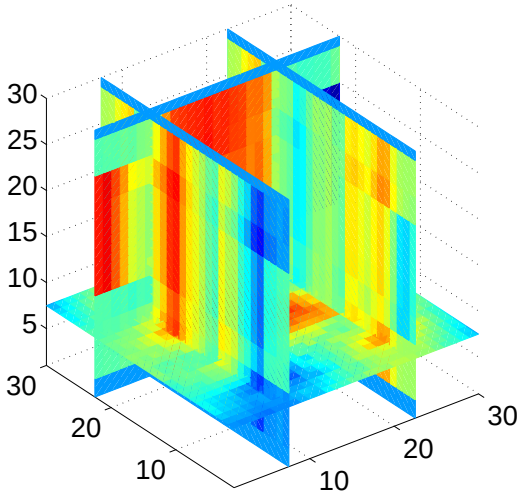

(d) Using 1 axis

Figure 3.6: Algebraic reconstruction of f_{12}

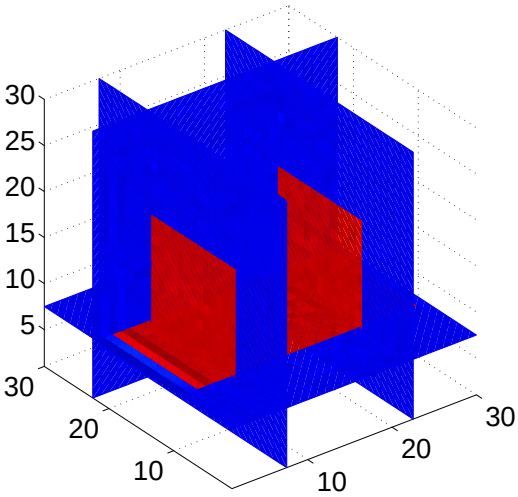

(a) Using 6 axes

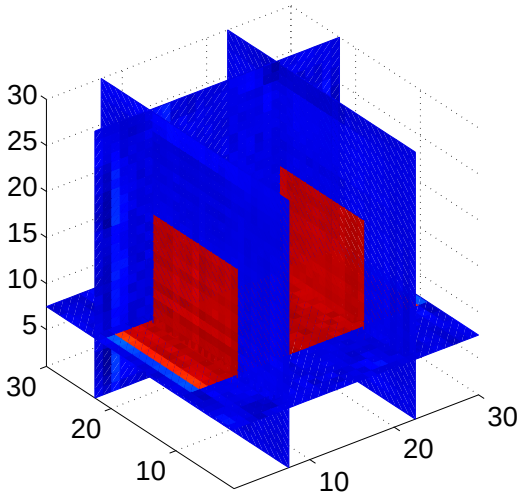

(b) Using 3 axes

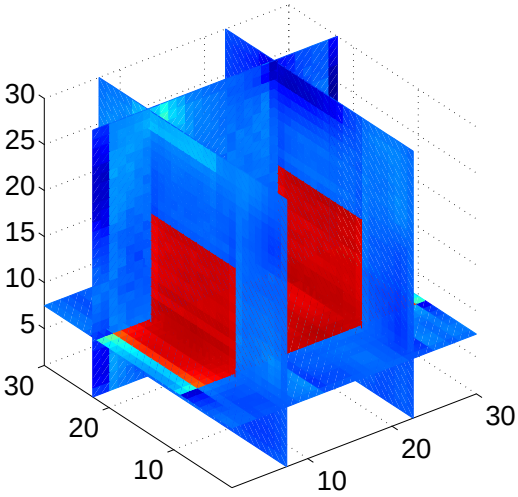

(c) Using 2 axes

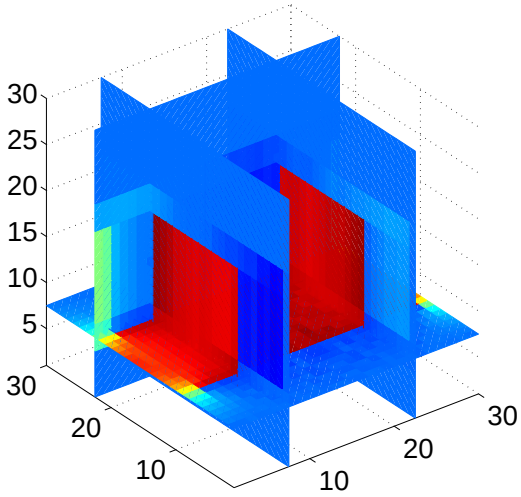

(d) Using 1 axis

Figure 3.7: Algebraic reconstruction of f_{13}

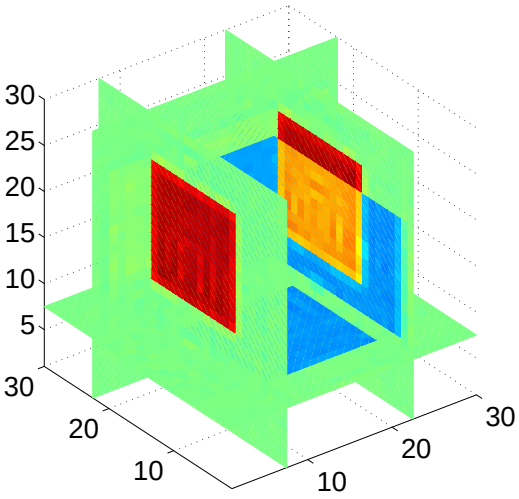

(a) Using 6 axes

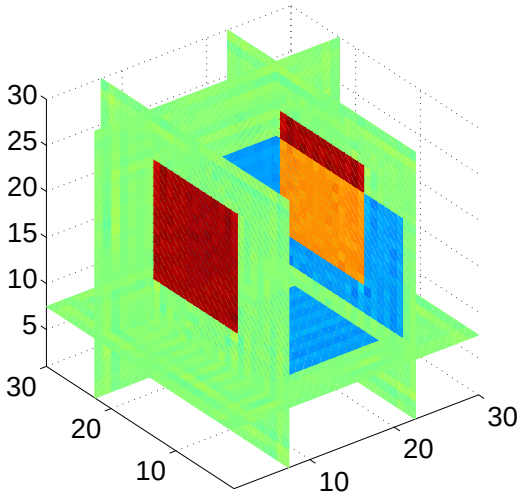

(b) Using 3 axes

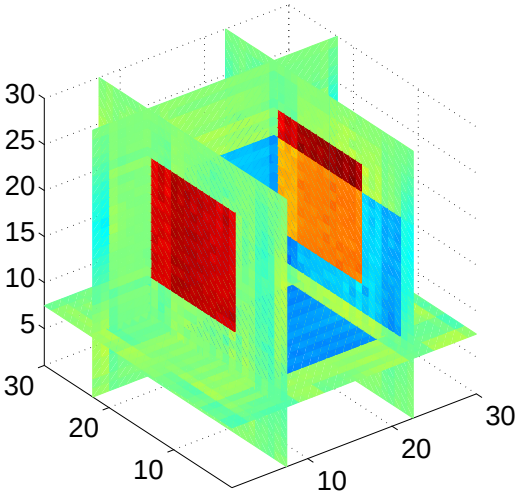

(c) Using 2 axes

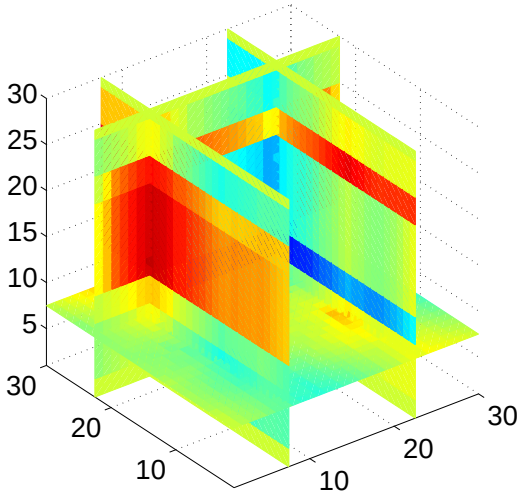

(d) Using 1 axis

Figure 3.8: Algebraic reconstruction of f_{22}

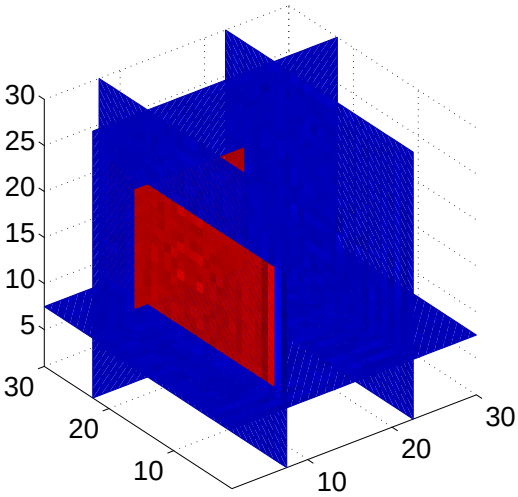

(a) Using 6 axes

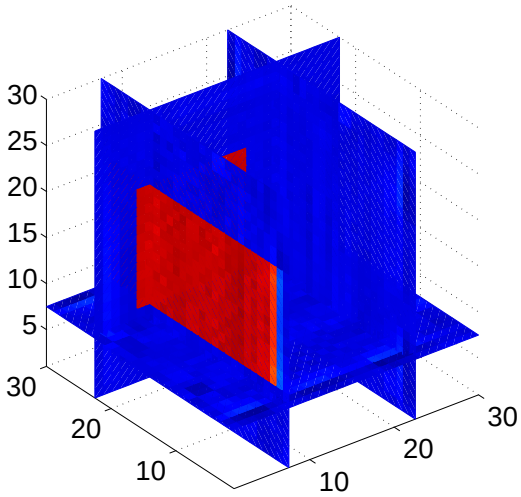

(b) Using 3 axes

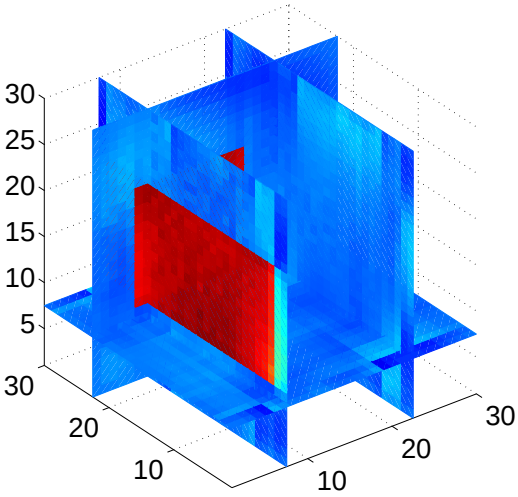

(c) Using 2 axes

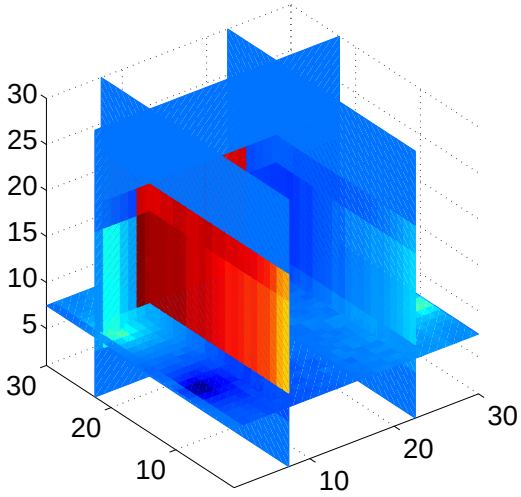

(d) Using 1 axis

Figure 3.9: Algebraic reconstruction of f_{23}

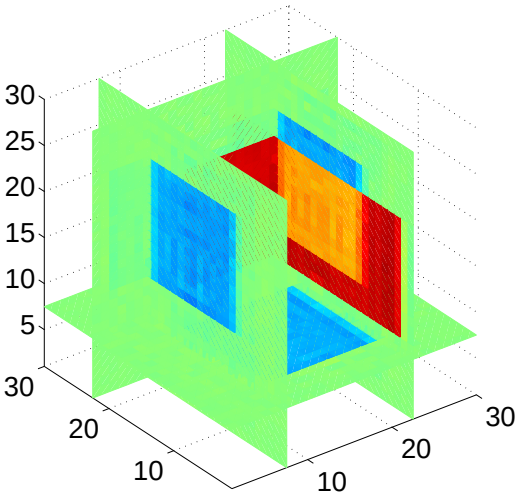

(a) Using 6 axes

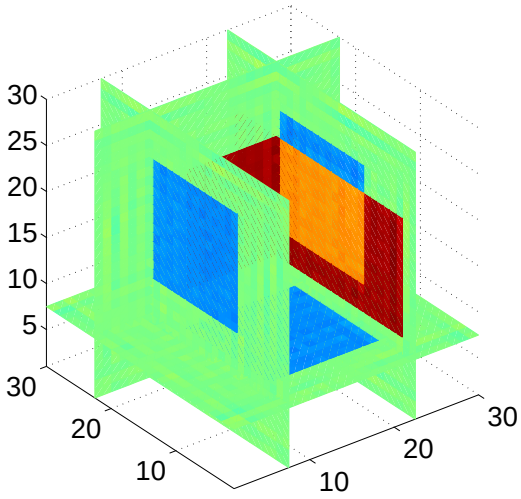

(b) Using 3 axes

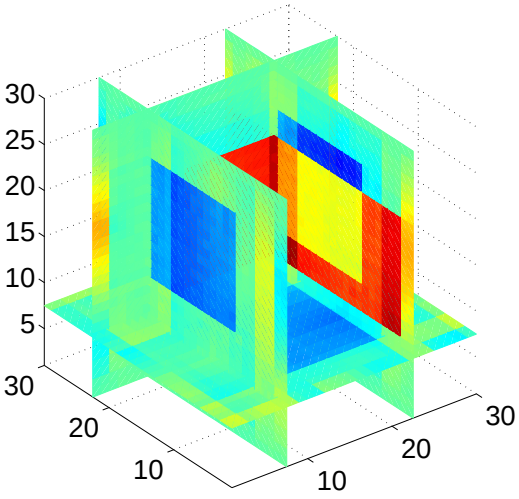

(c) Using 2 axes

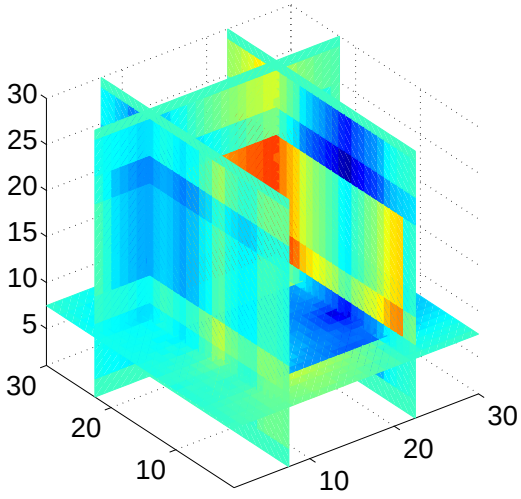

(d) Using 1 axis

Figure 3.10: Algebraic reconstruction of f_{33}

3.4 The general reconstruction algorithm

Below is a description of the new general reconstruction algorithm for the TTRT developed by Sharafutdinov and Lionheart [15]. In Section 5.4 we present the first published results of a numerical implementation of these methods. We recall the setup and notation: We have a tensor field $f_{ij} \in \mathscr{S}$, for which we have measured the TTRT, $Kf(\xi, x)$ for rays (ξ, x) parallel to k planes with normals $\eta_1, \ldots \eta_k$. This corresponds to tomographic data acquisition rotating about an axis aligned with η_i. By $K_\eta f$ we denote the data collected for all lines perpendicular to a unit vector η. For brevity, when using a set of vectors $\eta_1 \ldots \eta_k$ we sometimes write X_i to mean X_{η_i}. The data $K_i f$ is a trace-free symmetric 2×2 matrix and thus has two independent values, the *off-diagonal* component $K_i^1 f = (K_i f)\eta \cdot (\xi \times \eta)$, and the *diagonal* component $K_i^2 f = (K_i f)\eta \cdot \eta$. This may be seen by considering the tensor in the coordinate frame of the ray $(\xi \times \eta, \xi, \eta)$.

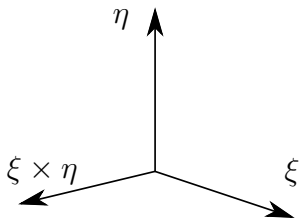

Figure 3.11: The coordinate frame of the ray

Continuing our example (3.15) with $\xi = e_2 = (0, 1, 0)$ and using $\eta = e_3 = (0, 0, 1)$ we have

$$K_\eta^1 = 2 \int_{x_2=-\infty}^{\infty} f_{13}\, dx_2, \quad \text{and} \tag{3.17}$$

$$K_\eta^2 = \int_{x_2=-\infty}^{\infty} f_{11} - f_{33}\, dx_2. \tag{3.18}$$

For each axis of rotation, the data is parameterized as $K_\eta^i f = K_\eta^i f(h, \theta, p)$ where h is the intersection of a given plane with η and (θ, p) are the usual coordinates of 2D Radon transforms in each plane. B_η is a two-dimensional backprojection as defined in (2.10) on each plane perpendicular to η.

Rather than working with the data $K^i f$ directly, we introduce intermediate variables λ and μ and describe the reconstruction in terms of these:

Lemma 3.2. *Let*

$$\lambda_\eta(y) = \frac{i}{2}|P_\eta y|\widehat{\left(B_\eta \frac{\partial K^1_\eta f}{\partial p}\right)} \tag{3.19}$$

$$\mu_\eta(y) = |P_\eta y|^3(\widehat{B_\eta K^2_\eta f}) \tag{3.20}$$

Then

$$\hat{f}(y)\eta \cdot P_\eta y = \lambda_\eta \tag{3.21}$$

$$|P_\eta y|^2 \hat{f}(y)\eta \cdot \eta - \hat{f}(y)P_\eta y \cdot P_\eta y = \mu_\eta \tag{3.22}$$

The unstable reconstruction algorithm uses three separate axes of rotation. For $\eta_1 = (1,0,0)$, we have $P_\eta y = (0, y_2, y_3)$, $\hat{f}\eta = (\hat{f}_{11}, \hat{f}_{12}, \hat{f}_{13})$ and using $\operatorname{Tr} \hat{f} = 0$,

$$|P_\eta y|^2 \hat{f}(y)\eta \cdot \eta - \hat{f}(y)P_\eta y \cdot P_\eta y = -\left((2y_2^2 + y_3^2)\hat{f}_{22} + 2y_2y_3\hat{f}_{23} + (y_2^2 + 2y_3^2)\hat{f}_{33}\right).$$

This allows us to rewrite equations (3.21)-(3.22) for η_1 as

$$y_2\hat{f}_{12} + y_3\hat{f}_{13} = \lambda_{\eta_1} \tag{3.23}$$

$$(2y_2^2 + y_3^2)\hat{f}_{22} + 2y_2y_3\hat{f}_{23} + (y_2^2 + 2y_3^2)\hat{f}_{33} = -\mu_{\eta_1} \tag{3.24}$$

Repeating these calculations for $\eta_2 = (0,1,0)$ and $\eta_3 = (0,0,1)$ we get the following system of equations:

$$\begin{cases} y_2\hat{f}_{12} + y_3\hat{f}_{13} & = \lambda_{\eta_1} \\ y_1\hat{f}_{12} + y_3\hat{f}_{23} & = \lambda_{\eta_2} \\ y_1\hat{f}_{13} + y_2\hat{f}_{23} & = \lambda_{\eta_3} \\ (2y_2^2 + y_3^2)\hat{f}_{22} + 2y_2y_3\hat{f}_{23} + (y_2^2 + 2y_3^2)\hat{f}_{33} & = -\mu_{\eta_1} \\ (2y_1^2 + y_3^2)\hat{f}_{11} + 2y_1y_3\hat{f}_{13} + (y_1^2 + 2y_3^2)\hat{f}_{33} & = -\mu_{\eta_2} \\ (2y_1^2 + y_2^2)\hat{f}_{11} + 2y_1y_2\hat{f}_{12} + (y_1^2 + 2y_2^2)\hat{f}_{22} & = -\mu_{\eta_3} \end{cases} \tag{3.25}$$

Lionheart and Sharafutdinov show that this system is nondegenerate everywhere except the coordinate planes, and so by continuity it has a unique solution on the whole of $\mathbb{R}^3$.

The stable reconstruction algorithm starts again from Lemma (3.2) but uses six axes to arrive at a system of equations which has a stable solution. The inversion is somewhat more involved and we will leave out the details. We present the final result, which corresponds to the final step in the practical implementation of this algorithm.

As suggested in [15] we use the following 6 axes: Let (e_1, e_2, e_3) be the standard basis for $\mathbb{R}^3$. We then use

$$\begin{cases} \eta_1 = \frac{1}{\sqrt{2}}(e_2 + e_3), \quad \eta_2 = \frac{1}{\sqrt{2}}(e_3 + e_1), \quad \eta_3 = \frac{1}{\sqrt{2}}(e_1 + e_2) \\ \eta_4 = \frac{1}{\sqrt{2}}(e_2 - e_3), \quad \eta_5 = \frac{1}{\sqrt{2}}(e_3 - e_1), \quad \eta_6 = \frac{1}{\sqrt{2}}(e_1 - e_2) \end{cases} \tag{3.26}$$

From Lemma (3.2) we now obtain 12 equations, and some algebraic manipulation yields the following, stable system for the off-diagonal entries of $\hat{f}$ for all $y \neq 0$:

$$\begin{cases} |y|^2 \hat{f}_{12} + y_2 y_3 \hat{f}_{13} + y_1 y_3 \hat{f}_{23} = (\mu_3 - \mu_6)/2 \\ y_2 y_3 \hat{f}_{12} + |y|^2 \hat{f}_{13} + y_1 y_2 \hat{f}_{23} = (\mu_2 - \mu_5)/2 \\ y1_y 3 \hat{f}_{12} + y_1 y_2 \hat{f}_{13} + |y|^2 \hat{f}_{23} = (\mu_1 - \mu_4)/2 \end{cases} \tag{3.27}$$

Sharafutdinov and Lionheart comment that singularities at the origin are inherent to this reconstruction approach, since the main equations (3.21)-(3.22) of Lemma 3.2 vanish at $y = 0$, and agree to disregard such singularities. As we shall see in Section 3.6, this issue is avoided as soon as f has compact support.

Finally, we are able to express the diagonal entries of $\hat{f}$ in terms of the off-diagonal entries from the solution of (3.27) and the corresponding λ_i.

$$\begin{aligned} \hat{f}_{11} = \frac{\sqrt{2}}{3|y|^2}\Big((y_2 + y_3)\lambda_1 + (y_1 - 2y_3)\lambda_2 + (y_1 - 2y_2)\lambda_3 + (y_2 - y_3)\lambda_4 \\ - (y_1 + 2y_3)\lambda_5 + (y_1 + 2y_2)\lambda_6\Big) - \frac{4}{3|y|^2}(y_1 y_2 \hat{f}_{12} + y_1 y_3 \hat{f}_{13} - 2y_2 y_3 \hat{f}_{23}). \end{aligned} \tag{3.28}$$

$$\begin{aligned}\hat{f}_{22} = \frac{\sqrt{2}}{3|y|^2}\Big((y_2 - 2y_3)\lambda_1 + (y_1 + y_3)\lambda_2 - (2y_1 - y_2)\lambda_3 + (y_2 + 2y_3)\lambda_4 \\ - (y_1 - y_3)\lambda_5 - (2y_1 + y_2)\lambda_6\Big) - \frac{4}{3|y|^2}(y_1y_2\hat{f}_{12} - 2y_1y_3\hat{f}_{13} + y_2y_3\hat{f}_{23}),\end{aligned} \tag{3.29}$$

$$\begin{aligned}\hat{f}_{33} = \frac{\sqrt{2}}{3|y|^2}\Big(- (2y_2 - y_3)\lambda_1 - (2y_1 - y_3)\lambda_2 + (y_1 + y_2)\lambda_3 - (2y_2 + y_3)\lambda_4 \\ + (2y_1 + y_3)\lambda_5 + (y_1 - y_2)\lambda_6\Big) - \frac{4}{3|y|^2}(-2y_1y_2\hat{f}_{12} + y_1y_3\hat{f}_{13} + y_2y_3\hat{f}_{23}).\end{aligned} \tag{3.30}$$

This completes the algorithm for the reconstruction of $f_{ij} \in \mathscr{S}$ from TTRT data by Sharafutdinov and Lionheart. Next we make use of the intermediate variables λ and μ from this work to investigate the nullspace of the TTRT for one axis.

3.5 The nullspace of the single axis TTRT

Armed with machinery from the general reconstruction algorithm we show that the TTRT with data from a single axis does indeed have a non-trivial nullspace, as suggested by the numerical experiments in Section 3.3.1. For convenience we repeat the relevant equations from Section 3.4:

$$\hat{f}(y)\eta \cdot P_\eta y = \lambda_\eta \tag{3.31}$$

$$|P_\eta y|^2 \hat{f}(y)\eta \cdot \eta - \hat{f}(y)P_\eta y \cdot P_\eta y = \mu_\eta \tag{3.32}$$

Our one axis of rotation is denoted by η and we now assume $\lambda_\eta = \mu_\eta = 0$. We will construct the tensor f in the Fourier domain, component-wise for each y. We begin by fixing some y, and noting that if $P_\eta y = 0$, then (3.31)-(3.32) are identically satisfied. From now on we assume $P_\eta y \neq 0$ and let our tensor be defined by analytic extension for such y satisfying $y = t\eta,\ t \in \mathbb{R}$.

We now define

$$\xi = \frac{P_\eta y}{|P_\eta y|}, \quad \text{and} \tag{3.33}$$

$$\zeta = \eta \times \xi \tag{3.34}$$

Considering $\hat{f}$ in the coordinate system given by (η, ξ, ζ), (3.31) and (3.32) now read $\hat{f}_{12} = 0$ and $\hat{f}_{11} - \hat{f}_{22} = 0$, respectively. These, along with $\operatorname{Tr} \hat{f} = 0$ are the only conditions on $\hat{f}$, so we may choose arbitrary values α, β and γ to construct the tensor

$$\hat{f}(\tilde{y}) = \begin{pmatrix} \alpha_{\eta,y} & 0 & \beta_{\eta,y} \\ 0 & -\alpha_{\eta,y} & \gamma_{\eta,y} \\ \beta_{\eta,y} & \gamma_{\eta,y} & 0 \end{pmatrix} \tag{3.35}$$

satisfying (3.31)-(3.32). Here we use the notation $\hat{f}(\tilde{y})$ to indicate that we are considering $\hat{f}$ in (η, ξ, ζ)-coordinates.

To find $f(x)$ we use a rotation matrix $R_{y \to \tilde{y}}$ to change back to standard coordinates for each y, followed by an inverse Fourier transform, giving

$$f(x) = \int e^{ix \cdot y} \; R^T_{y \to \tilde{y}} \; \hat{f}(\tilde{y}) \; R_{y \to \tilde{y}} \; dy. \tag{3.36}$$

Since α, β and γ were arbitrary, we have constructed a non-trivial element of the nullspace of the TTRT with data from a single axis, proving the hypothesis suggested by the numerical evidence in Section 3.3.1. We note that the rotation matrix R is an analytic function of y and only depends on the direction of y, not its magnitude. This enables us to impose smoothness restrictions such as $\hat{f}(\tilde{y}) \in \mathscr{S}$ and have them carry over to $\hat{f}(y)$. Growth restrictions on $\hat{f}(\tilde{y})$ will also be respected, including the conditions for the Paley-Wiener Theorem guaranteeing compact support for $f(x)$.

We return to multi-axis TTRT to present new results regarding the stability of the reconstruction in certain Sobolev spaces, making use of results from Section 2.3.

3.6 The TTRT on Sobolev spaces

In this section we present novel results extending the general TTRT reconstruction algorithm to certain Sobolev spaces and considering stability estimates.

We restrict our attention to compactly supported functions. It is clear that this is indeed the case for any practical application we are considering. Since we defined $H^s(B_a)$ as the completion of $C^\infty(B_a)$, it is enough to consider $f_{ij} \in C^\infty(B_a)$.

The definitions of λ and μ are in terms of slice-by-slice backprojections, followed by powers of the Laplacian on each slice. It is possible to rewrite these expressions in terms of slice-by-slice *filtered* backprojections, which enables us to make use of stability results from the Radon transform inversion.

Recall the definition of λ_η:

$$\lambda_\eta = \frac{i}{2}|P_\eta y|\left(\widehat{B_\eta \frac{\partial K_\eta^1 f}{\partial p}}\right) \tag{3.37}$$

In order to deal with the derivative $\partial/\partial p$, we make use of the following remark:

Remark 3.3. Let $f(x) \in H^s(B_a)$. Applying a Hilbert transform in any of its variables still leaves f in H^s. Indeed, a Hilbert transform is nothing but a multiplication by $i\,\mathrm{sgn}(y)$ in the Fourier domain, and clearly leaves $|\hat{f}|$ unchanged. The result follows from the definition of the Sobolev norm.

We use the above remark and replace $K_\eta^1 f$ by $\bar{K}_\eta^1 f$ given by

$$\mathcal{F}_{p\to t}\bar{K}_\eta^1 f(h,\theta,p) = -i(\mathrm{sgn}\, t)\mathcal{F}_{p\to t}K_\eta^1 f(h,\theta,p), \tag{3.38}$$

which gives

$$\begin{aligned} |\lambda_\eta| &= \tfrac{1}{2}|P_\eta y|\ |\overline{\mathrm{FBP}}\bar{K}_\eta^1 f| \\ &\leq \tfrac{1}{2}|y|\ |\overline{\mathrm{FBP}}\bar{K}_\eta^1 f|, \end{aligned} \tag{3.39}$$

and

$$||\check{\lambda}_\eta||_s \leq |||K_\eta^1|||_{\overline{s+\frac{3}{2}}}. \tag{3.40}$$

For μ_η we have

$$\begin{aligned} \mu_\eta &= |P_\eta y|^3(\widehat{B_\eta K_\eta^2 f}) \\ &= |P_\eta y|^2\overline{\mathrm{FBP}}K_\eta^2 f \\ &\leq |y|^2\overline{\mathrm{FBP}}K_\eta^2 f \end{aligned} \tag{3.41}$$

Hence,

$$||\check{\mu}_\eta||_{s+2} \leq |||K_\eta^2|||_{\overline{s+\frac{1}{2}}}. \tag{3.42}$$

We turn our attention to the choice of axes (3.26) used for the stable general reconstruction algorithm. For this particular choice of rotation axes, Sharafutdinov and Lionheart derive a system of equations (3.27) for the off-diagonal entries of f. The system is uniquely solvable for any $y \neq 0$ and satisfies the bound

$$|\hat{f}_{ij}| \leq \frac{3}{2}|y|^{-2} \sum_{i=1}^{3} |\mu_i(y) - \mu_{i+3}(y)| \quad (i \neq j). \tag{3.43}$$

Let $\varepsilon > 0$ and consider a high pass filtered f_{ij}, $f_{\varepsilon,ij}$,given by

$$\hat{f}_{\varepsilon,ij}(y) = \begin{cases} \hat{f}_{ij} & |y| > \varepsilon \\ 0 & |y| \leq \varepsilon \end{cases} \tag{3.44}$$

Just like $\hat{f}_{ij}$, $\hat{f}_{\varepsilon,ij}$ is uniquely determined from (3.27) and

$$||f_{\varepsilon,ij}||_s \leq ||\check{\mu}_\eta||_{s+2}. \tag{3.45}$$

and using (3.42), we have

$$||f_{\varepsilon,ij}||_s \leq |||K^2_\eta|||_{\frac{}{s+\frac{1}{2}}}. \tag{3.46}$$

Given $\hat{f}_{ij}, i \neq j$, Sharafutdinov and Lionheart provide a stable reconstruction of the diagonal components $\hat{f}_{ii}$ from the off-diagonal components and the λ_i, as given by (3.28)-(3.30). Replacing $\hat{f}_{ij}$ by $\hat{f}_{\varepsilon,ij}$, we proceed in the same way. The final stability estimate by Sharafutdinov and Lionheart reads

$$|\hat{f}(y)|^2 \leq C\Big(|y|^{-2} \sum_{i=1}^{6} |\lambda_i(y)|^2 + |y|^{-4} \sum_{i=1}^{3} |\mu_i(y) - \mu_{i+3}(y)|^2\Big) \tag{3.47}$$

for some constant C.

Finally, considering (3.47) together with (3.39) and (3.41) we have

Theorem 3.4. *Let $f_{ij} \in C^\infty(B_a)$ and $K^i_{\eta_i} f$ be given. Then for any $\varepsilon > 0$ we have*

$$||\hat{f}_\varepsilon(y)||^2_s \leq \sum_{i=1}^{6} \Big(C|||K^1_{\eta_i}|||^2_{\frac{}{s+\frac{1}{2}}} + C'|||K^2_{\eta_i}|||^2_{\frac{}{s+\frac{1}{2}}}\Big) \tag{3.48}$$

for some constants $C(\varepsilon)$, $C'(\varepsilon)$.

We can thus *stably* recover f, everywhere outside an ε-ball in the Fourier domain. As we shall see, f having compact support is enough for us to stably recover the missing ε-ball. We note that, in a sense, this is the opposite of another common inverse problem, analytic extrapolation. By the Paley-Wiener Theorem, a compactly supported function has an analytic Fourier transform. Analytic extrapolation, or analytic continuation, considers a situation where an analytic function is known on a compact interval, and attempts to recover the function everywhere else. This process has a unique solution but is severely ill-posed, see e.g. [5]. Returning to the problem at hand, we are in the fortunate situation to know the function values *everywhere except* a small ball. Moreover, the unknown ball is arbitrarily small. We proceed with the following lemma.

Lemma 3.5. *Let f be a compactly supported function with support in B_a and $\hat{f}_\varepsilon$ be a high pass filtered f, given by*

$$\hat{f}_\varepsilon(y) = \begin{cases} \hat{f} & |y| > \varepsilon \\ 0 & |y| \leq \varepsilon \end{cases} \tag{3.49}$$

Then f is completely and stably determined by $\hat{f}_\varepsilon$ for some $\varepsilon > 0$

Proof. Let $\text{Ш}_a(x)$ be the n-dimensional Shah function of period a, given by

$$\text{Ш}_a(x) = \prod_{i=0}^{n} \sum_{k=-\infty}^{\infty} \delta(x_i - ka) \tag{3.50}$$

We consider the periodic extension of f, given by a convolution with the Shah function and make use of the fact that the Fourier transform of $\text{Ш}_a(x)$ is $\frac{1}{a}\text{Ш}_{\frac{1}{a}}(x)$. This gives

$$\begin{aligned} \widehat{f * \text{Ш}_a} &= \hat{f}\ \widehat{\text{Ш}}_a \\ &= \hat{f}\ \tfrac{1}{a}\text{Ш}_{\frac{1}{a}}. \end{aligned} \tag{3.51}$$

Choosing some ε such that $0 < \varepsilon < \frac{1}{a}$ we may now evaluate $\widehat{f * \text{Ш}_a}$ everywhere except the origin. We can thus recover f up to one additive constant, corresponding to the Fourier transform evaluated at zero. But since we know that f is compactly supported, this final constant is also fixed, giving the result. □

We have extended the work of Sharafutdinov and Lionheart and shown that considering the TTRT as a mapping of tensor components in $H_0^s(B_a)$ to components in $H_0^s(Z_a)$ has a continuous inverse. We will now move on to consider some specialised reconstruction methods and the advantages these can provide in the cases where they apply.

Chapter 4

Special Tensors

In this chapter we will consider some special types of tensors and investigate the possibilities for reconstruction in these cases. Clearly the general reconstruction algorithm could be applied, but, as we shall see, there are better options available. We will describe one algorithm for certain tensors predating the general reconstruction, considering it in light of the more recent work. We will also describe a completely new algorithm for a different class of tensors, which when applicable provides a more efficient reconstruction. Finally we use results from scalar Radon inversion to describe new reconstruction algorithms for these special tensors in the case of data truncation.

Before describing the algorithms we briefly leave the subject of photoelastic reconstruction for a discussion of general symmetric tensor fields. Sharafutdinov [24, Ch 2] shows that there is a unique splitting of tensor fields into *solenoidal* (divergence free) and *potential* (symmetrised derivative of a vector field) parts. Whereas solenoidal fields often arise in engineering situations where the stress is due to temperature changes, certain cases of mechanical loading results in a purely potential stress field. It is worth noting that while we restrict our considerations to rank 2 tensors over $\mathbb{R}^3$, the tensor field splitting result by Sharafutdinov is given for general rank k tensors over $\mathbb{R}^n$.

The case of solenoidal fields has been studied extensively by Aben et al., see e.g. [2], and we shall return to these in Section 4.3. Photoelastic tomography of potential stress fields is less studied, and we will show that for these, the reconstruction

algorithm presented in [15] can be drastically improved.

4.1 Potential tensors

A symmetric rank two tensor field f is said to be *potential* if can be written as the symmetrised derivative of a vector field:

$$f_{ij} = \frac{1}{2}\left(\frac{\partial u_i}{\partial x_j} + \frac{\partial u_j}{\partial x_i}\right) \tag{4.1}$$

A strain field of this type satisfies a set of equations known as Saint-Venant's compatibility condition. The condition is the vanishing of the Saint-Venant tensor

$$W_{ijkl} = \frac{\partial^2 f_{ij}}{\partial x_k \partial x_l} + \frac{\partial^2 f_{kl}}{\partial x_i \partial x_j} - \frac{\partial^2 f_{il}}{\partial x_j \partial x_k} - \frac{\partial^2 f_{jk}}{\partial x_i \partial x_l} \qquad i,j,k,l = 1,2,3. \tag{4.2}$$

This is easily verified by direct calculation. Substituting (4.1) in (4.2) we get

$$\begin{aligned} W = &\frac{1}{2}\left(\frac{\partial^3 u_j}{\partial x_k \partial x_l \partial x_i} + \frac{\partial^3 u_i}{\partial x_k \partial x_j \partial x_i}\right) \\ &+ \frac{1}{2}\left(\frac{\partial^3 u_k}{\partial x_i \partial x_j \partial x_l} + \frac{\partial^3 u_k}{\partial x_i \partial x_j \partial x_l}\right) \\ &- \frac{1}{2}\left(\frac{\partial^3 u_i}{\partial x_j \partial x_k \partial x_l} + \frac{\partial^3 u_i}{\partial x_j \partial x_k \partial x_l}\right) \\ &- \frac{1}{2}\left(\frac{\partial^3 u_j}{\partial x_i \partial x_l \partial x_k} + \frac{\partial^3 u_j}{\partial x_i \partial x_l \partial x_k}\right) \end{aligned} \tag{4.3}$$

A sufficiently smooth potential field clearly satisfies $W = 0$. By symmetries in f and order of derivatives, the 81 permutations of the indices reduce to 6 distinct equations. One such choice of indeces (i,j,k,l) is

$$\{(1,1,2,2),(1,1,3,3),(2,2,3,3),(1,1,2,3),(1,2,2,3),(1,1,2,3)\} \tag{4.4}$$

Another way to look at the Saint-Venant tensor is to use the operator CURL defined by Amrouche et al. in [3].

Definition 4.1. Let f be a rank two tensor field over $\mathbb{R}^3$. The matrix curl of f $\operatorname{CURL} f$, mapping tensors to tensors is defined as

$$\operatorname{CURL}(f)_{ij} = \epsilon_{ilk}\partial_l f_{jk} \tag{4.5}$$

where ϵ_{ijk} is the Levi-Civita symbol given by

$$\epsilon_{ijk} = \begin{cases} +1 & \text{if } ijk \text{ is an even permutation of } 123 \\ -1 & \text{if } ijk \text{ is an odd permutation of } 123 \\ 0 & \text{if any index is repeated} \end{cases}$$

and $\partial_i = \partial/\partial x_i$. For brevity, we write $\mathscr{C}$ to mean the operator CURL applied twice.

The Saint-Venant tensor may then be written as $Wf = \mathscr{C}f$ as may be verified by writing out the terms. For symmetric tensors f, $\mathscr{C}f$ is itself a symmetric tensor and this clearly shows that there are only 6 independent equations in W. Indeed, we have

$$\begin{aligned} (\mathscr{C}f)_{ij} &= \epsilon_{ilk}\partial_l \operatorname{CURL} f_{jk} \\ &= \epsilon_{ilk}\epsilon_{jmn}\partial_l\partial_m f_{kn} \\ &= \epsilon_{ilk}\epsilon_{jmn}\partial_m\partial_l f_{nk} \\ &= (\mathscr{C}f)_{ji}. \end{aligned} \tag{4.6}$$

Potential tensors occur in practice in applications where the stress is due to strain, for example from mechanical loading. Consider an object going through a small deformation given by the vector field u. The strain tensor ε is defined by

$$\varepsilon_{ij} = \frac{1}{2}\left(\frac{\partial u_i}{\partial x_j} + \frac{\partial u_j}{\partial x_i}\right). \tag{4.7}$$

If the strain is sufficiently small to be in the range of linear elasticity, the stress σ is a linear function of strain, $\sigma = L(\varepsilon)$. For an isotropic material, L must be of the form (3.4)

$$L_{d,h}(f) = d\mathbf{D}(f) + h\mathbf{H}(f). \tag{4.8}$$

In the literature [20, 28] the parameters d and h are known in terms of the Lamé coefficients λ and μ and for a homogeneous material they are constants:

$$\sigma = 2\mu\varepsilon + \lambda \operatorname{Tr}\varepsilon I_3 = 2\mu\mathbf{D}(\varepsilon) + (2\mu + 3\lambda)\mathbf{H}(\varepsilon) \tag{4.9}$$

The linear relationships between strain and stress, and stress and permittivity mean that they have to be of the form (3.4). In particular, the isotropic part of ε, $\mathbf{H}\varepsilon$ is a scalar multiple of $\mathbf{H}\epsilon$, and hence constant. Thus, the Saint-Venant's tensor $W\varepsilon$ is zero if and only if $W\mathbf{D}\varepsilon$ is zero. Applying the relationship from (3.4) again we have that f also satisfies $Wf = 0$. We exploit this fact in a new reconstruction algorithm for tensors f such that $Wf = 0$.

4.2 A novel reconstruction algorithm for potential tensor fields

In this section we present a new reconstruction algorithm for the TTRT in the case of a potential strain field. We return to Lemma 3.2 and consider again the case $\eta_3 = e_3$, with the added condition of $Wf = 0$. Considering the Saint-Venant condition in the Fourier domain, we have

$$y_i y_j \hat{f}_{kl} + y_k y_l \hat{f}_{ij} - y_i y_l \hat{f}_{jk} - y_j y_k \hat{f}_{il} = 0 \qquad i, j, k, l = 1, 2, 3. \tag{4.10}$$

We start from the third equation of (3.25). Using the Saint-Venant condition to substitute the middle term and rearranging we get

$$2(y_1^2 + y_2^2)(\hat{f}_{11} + \hat{f}_{22}) = -\mu_{\eta_3} \tag{4.11}$$

And $\operatorname{Tr} f = 0$ gives

$$2(y_1^2 + y_2^2)\hat{f}_{33} = \mu_{\eta_3} \tag{4.12}$$

Now, μ_{η_3} was given by a plane by plane backprojection, followed by a multiplication in the Fourier domain by $(y_1^2 + y_2^2)^{3/2}$, so going back to the original data variable, we have

$$\hat{f}_{33} = \frac{1}{2}(y_1^2 + y_2^2)^{1/2}(\widehat{B_{\eta_3} K^2_{\eta_3} f}) \tag{4.13}$$

Comparing (4.13) with the definitions in Section 2.2, we note that this is nothing but a scalar Radon inversion of the form backproject-then-filter for each plane perpendicular to η_3. Indeed, $\frac{1}{2}(y_1^2 + y_2^2)^{1/2} = |P_{\eta_3} y|$ and so in each plane perpendicular to

η_3, this is equal to a ramp filter I^{-1}, exactly as in the 2D Radon transform inversion of (2.22).

Thus, f_{33} is exactly given by the 2D **scalar** Radon transform of K^2 in each plane, and can be reconstructed very efficiently for each plane from data collected using only one axis of rotation, for example using the more efficient inversion algorithm in (2.21) which uses a 1D filter. We have thus proved the following theorem:

Theorem 4.2. *Let f be a potential tensor field with $f_{ij} \in \mathscr{S}(\mathbb{R}^3)$. Then*

$$\bar{R}f_{33}(\theta, p, x_3) = K^2_{e_3} f(x_3, \theta, p) \tag{4.14}$$

The general method presented in [15] requires the collection of data for several axes, a solution of a system of equations for each point in the Fourier domain, and finally a 3D Fourier inversion before anything is reconstructed. In contrast to this, the algorithm presented here can be implemented very efficiently using standard methods of scalar 2D Radon transform inversion, and if only one component of the tensor is required, it is enough to use one axis of rotation. The sufficiency of one axis is of particular interest, as data acquisition is otherwise very time consuming. Changing axis of rotation requires human interaction with the experimental setup, and also presents additional practical challenges such as image registration for matching up data from different axes. In Section 4.4.1 we will also see how this new algorithm allows us to apply methods from x-ray reconstruction to handle photoelastic reconstruction from truncated data.

We now turn our attention to the second special type of tensor under consideration: solenoidal tensors.

4.3 Solenoidal tensors

A solenoidal tensor field f satisfies

$$\sum_{j=1}^{3} \frac{\partial f_{ij}}{\partial x_j} = 0 \tag{4.15}$$

for each i.

For an elastic body in equilibrium, with body forces absent or negligible, the stress tensor satisfies (4.15) [20]. Though explained in different terminology, this equation forms the basis of a reconstruction method for photoelastic tomography by Aben et al. [2] known as *Integrated Photoelasticity*. This method uses TTRT data from one axis of rotation to reconstruct a single tensor component, perpendicular to the axis of rotation. In contrast to the solution to the same problem given by Sharafutdinov [24, sec 2.16], Aben's method is not restricted to convex domains. Moreover, the method uses a regular backprojection, rather than Sharafutdinov's weighted *moment backprojection* which lends itself to less efficient implementations. Aben's method requires an integration and a differentiation of the TTRT data, followed by a scalar Radon transform reconstruction in each plane.

In light of the recent work by Lionheart and Sharafutdinov [15] it is clear that the assumption that the field is solenoidal is not required for a reconstruction using only data from rays parallel to a small number of planes. However, it is worth revising Aben's method as it provides a simpler and computationally less costly alternative for the solenoidal case. We will also show that considering the general reconstruction algorithm with the added assumption of a solenoidal tensor field does not reduce to Aben's method but rather to a new, related reconstruction procedure.

We will outline the method of Aben, reformulating it in a more mathematical framework. We also present the new, alternative solenoidal reconstruction derived from the general reconstruction algorithm.

4.3.1 Aben's method

The derivation of Aben's method in [2] appeals to physical principles and does not make clear its mathematical assumptions about the geometry of the domain. We hope in this section to clarify the derivation and its assumptions. The idea is to use the solenoidal property to reduce the problem to one of scalar Radon transform inversion. We may then use any of the inversion techniques from Section 2.2 to complete the reconstruction. Without loss of generality Aben chooses $\eta = e_3$ and

considers reconstruction of f_{33} in the plane $x_3 = Z$. We first restrict our attention to a single rotation angle, choosing rays parallel to some direction ξ perpendicular to η, say $\xi = e_2$, corresponding to $\theta = 0$. In the notation of Aben, our data is then

$$V_1(x_1, x_3) = K^2_{e_3} f(x_3, 0, x_1) = \int_{x_2=-\infty}^{\infty} f_{11} - f_{33}\, dx_2, \quad \text{and} \tag{4.16}$$

$$V_2(x_1, x_3) = K^1_{e_3} f(x_3, 0, x_1) = \int_{x_2=-\infty}^{\infty} 2f_{13}\, dx_2, \tag{4.17}$$

as in the example (3.17)-(3.18).

The case Aben et al. consider is a tensor field f on the closure of a domain D in $\mathbb{R}^3$ that is smooth apart from corners and edges. The field is solenoidal in the interior, and on the boundary satisfies a zero normal boundary condition $fn = 0$, where n is the normal to ∂D. It is not clear what assumptions are made about the domain. Aben's argument appears to require that a slice of D between $x_3 = Z$ and $x_3 = Z + \epsilon$, has the property that any plane of constant $x_3 \in [Z, Z + \epsilon]$ intersects ∂D with zero area.

Before continuing we digress with a remark: Rather than considering f on some domain D, we may consider it as a distribution on all of $\mathbb{R}^3$, given by the characteristic function of D multiplied by a smooth test function. In this case, the solenoidal condition in a distributional sense becomes a Neumann boundary condition on D exactly matching Aben's assumption, as well as a classical solenoidal condition on f in D.

Aben applies Gauss' theorem to the divergence free vector field with components f_{1i} on the slice of D with $x_3 \in [Z, Z + \epsilon]$ and $x_1 \in (-\infty, X]$. This is illustrated in Figure 4.1.

On the portion that intersects ∂D the normal component is zero so the remaining terms are

$$\int_{x_3=Z+\epsilon} f_{13}\, dx_1 dx_2 - \int_{x_3=Z} f_{13}\, dx_1 dx_2 + \int_{-\infty}^{\infty}\int_{Z}^{Z+\epsilon} f_{11}\, dx_3 dx_2 = 0. \tag{4.18}$$

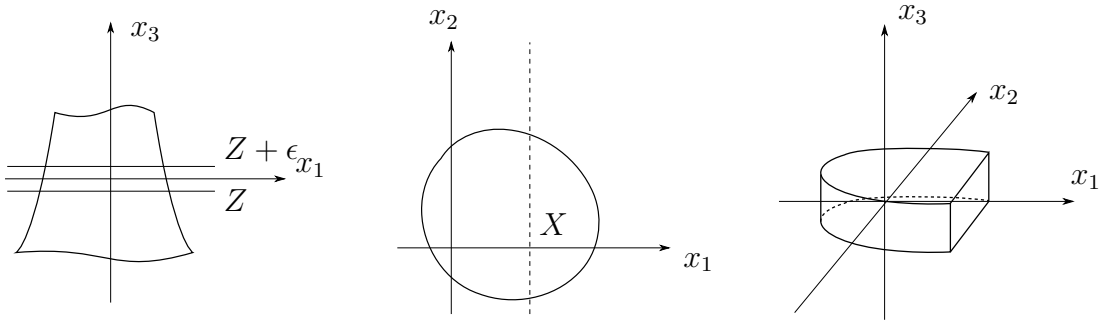

(a) Side view (b) Top view, slicing D (c) Slice of D

Figure 4.1: Illustration of slice of domain D used in Aben's method

Dividing by ϵ and taking the limit as $\epsilon \to 0$ we have

$$\int_{-\infty}^{\infty}\int_{-\infty}^{X} \left.\frac{\partial f_{13}}{\partial x_3}\right|_{x_3=Z} dx_1 dx_2 = \int_{-\infty}^{\infty} f_{11}\, dx_2, \tag{4.19}$$

and it follows that

$$\int_{x_2=-\infty}^{\infty} f_{33}\, dx_2 = \frac{\partial}{\partial x_3} \int_{x_1=-\infty}^{X} V_2\, dx_1 - V_1. \tag{4.20}$$

The RHS of (4.20) may be calculated from the data, and the LHS is exactly the two-dimensional Radon transform of f_{33} at $\theta = 0$. Repeating this argument for each rotation angle θ we arrive at a full set of 2D Radon transform data for f_{33} in the plane $x_3 = Z$. All that remains is to carry out a Radon transform inversion, for example using filtered backprojection. Repeating for each Z recovers f_{33} in the whole domain. The above argument is valid for any choice of rotation axis η, for each choice yielding the component $\eta \cdot f\eta$.

4.3.2 Another way of looking at Aben's method

Below we outline a different, more direct derivation of Aben's method. Starting with the assumption that f is solenoidal we have in particular

$$\frac{\partial f_{11}}{\partial x_1} + \frac{\partial f_{12}}{\partial x_2} + \frac{\partial f_{13}}{\partial x_3} = 0 \tag{4.21}$$

Integrating with respect to x_2 over all of $\mathbb{R}$ we have

$$\frac{\partial}{\partial x_1} \int_{x_2=-\infty}^{\infty} f_{11}\, dx_2 + \frac{\partial}{\partial x_3} \int_{x_2=-\infty}^{\infty} f_{13}\, dx_2 = 0 \tag{4.22}$$

and then integrating with respect to x_1 up to X we have

$$\int_{x_2=-\infty}^{\infty} f_{11}\, dx_2 = -\frac{\partial}{\partial x_3} \int_{x_1=-\infty}^{X} \int_{x_2=-\infty}^{\infty} f_{13}\, dx_2\, dx_1 \tag{4.23}$$

and the result follows as in (4.20).

To make it easier to compare to the other algorithms, we restate the relevant result in our previous notation, as the following theorem.

Theorem 4.3 (Aben's method)**.** *Let f be a solenoidal tensor. Then*

$$\bar{R}f_{33}(\theta, p, x_3) = \frac{\partial}{\partial x_3} \int_{\rho=-\infty}^{p} K^1_{e_3} f(x_3, \theta, \rho) - K^2_{e_3} f(x_3, \theta, p) \tag{4.24}$$

4.3.3 The general reconstruction formula [15] in the case of a solenoidal tensor field

It is of interest to investigate the general reconstruction formula when a solenoidal condition is enforced on f. As we shall see, it does not reduce to Aben's method, but rather to a new reconstruction method for solenoidal tensors. Considering (3.25) we notice that in the solenoidal case we have

$$\begin{aligned} &y_1\hat{f}_{11} + y_2\hat{f}_{12} + y_3\hat{f}_{12} = 0, \quad \text{and} \\ &y_1\hat{f}_{12} + y_2\hat{f}_{22} + y_3\hat{f}_{23} = 0, \quad \text{and} \\ &y_1\hat{f}_{13} + y_2\hat{f}_{23} + y_3\hat{f}_{33} = 0. \end{aligned} \tag{4.25}$$

Hence the first three equations of (3.25) reduce to

$$-y_i\hat{f}_{ii} = \lambda_i \tag{4.26}$$

and the diagonal components of f are given by

$$\hat{f}_{ii} = -\mathcal{F}^{-1}_{y\to x}(y_i^{-1}\lambda_i). \tag{4.27}$$

Once we have f_{ii}, the last three equations of (3.25) reduce to

$$y_i y_j \hat{f}_{ij} = g(y), \tag{4.28}$$

and $f_{ij},\ i \neq j$, can be found.

Considering, in particular, the reconstruction of f_{33}, we have

$$f_{33} = -\mathcal{F}^{-1}_{y\to x}\left(y_i^{-1}(y_1^2+y_2^2)\mathcal{F}_{x\to y} B_{e_3}\left[\frac{\partial K^1_{e_3}}{\partial p}\right]\right), \tag{4.29}$$

and since the multiplication by $(y_1^2+y_2^2)$ corresponds to a Riesz potential in each plane, we may write this as

$$\bar{R} f_{33}(\theta, p, x_3) = -\frac{\partial}{\partial p}\int_{z=-\infty}^{x_3} K^1_{e_3} f(z,\theta,p)\, dz \tag{4.30}$$

As in Aben's method, we recover the scalar Radon transform of the f_{33} component of the tensor. However, this algorithm is different from the Aben method (and indeed Sharafutdinov's original method in [24]). In particular, the only data required is the off-diagonal component K^1, or V_2 in the notation of Aben. Moreover, this algorithm involves differentiation in the x_1 direction and integration in x_3 direction, whereas these are reversed in Aben's method in Section 4.3.2.

This new reconstruction method for the solenoidal case can be derived without the machinery developed in [15], instead using a method similar to our derivation for Aben's method.

If we start with a different consequence of f being solenoidal, namely

$$\frac{\partial f_{13}}{\partial x_1} + \frac{\partial f_{23}}{\partial x_2} + \frac{\partial f_{33}}{\partial x_3} = 0 \tag{4.31}$$

and proceed as in Section 4.3.2 one obtains

$$\int_{x_2=-\infty}^{\infty} f_{33}\, dx_2 = -\frac{\partial}{\partial x_1}\int_{x_3=-\infty}^{Z} V_2\, dx_3, \tag{4.32}$$

which again yields a reconstruction formula for f_{33} using scalar Radon transform inversion as in (4.20). Note that considering all rotation angles, this reconstruction is identical to (4.30). This derivation is clearly much easier, not relying on any of the work needed for the general reconstruction.

4.3.4 Consistency condition

We have developed a reconstruction algorithm for solenoidal tensor fields which is distinct from the one by Aben et al. The two different formulae may be used together to arrive at a consistency condition on the TTRT data for solenoidal tensor fields. Since both algorithms recover $Rf_{33}(\theta, p)$ for a fixed angle θ, we have consistency conditions for each angle. By equating the two reconstruction methods for f_{33} we get

$$V_1 = \left(\int_{-\infty}^{Z} dx_3 \frac{\partial}{\partial x_1} + \int_{\infty}^{X} dx_1 \frac{\partial}{\partial x_3} \right) V_2. \tag{4.33}$$

This may be used in an experimental setting to check the validity of assuming a solenoidal stress field.

We now turn our attention to limited data problems, focusing on the algorithms for potential and solenoidal tensors.

4.4 Photoelastic tomography from truncated data

In the previous sections we have presented reconstruction algorithm for two commonly occurring cases in photoelastic tomography, potential and solenoidal tensor fields. Both cases, in slightly different ways, involve reducing the reconstruction of the tensor field to a scalar 2D Radon reconstruction yielding a given component of the tensor. Once in the domain of Radon inversion, we are able to apply new techniques developed in this field for certain types of data truncation problems. Of particular interest here are the Hilbert transform methods, which provide an exact reconstruction method for a special, but commonly occurring, type of data truncation. Typical practical applications include clamping apparatus obscuring some views or elongated specimens which in certain directions are too wide to fit in the field of view.

4.4.1 Hilbert transforms and potential tensors

The easiest case is the one for potential tensor fields. In Section 4.2 we showed that the reconstruction the $P_\eta f$ component of the tensor f is given exactly by a Radon

transform inversion of the data $K^2_\eta f$. We are thus in a position to use the two step Hilbert reconstruction described in Section 2.4.5 directly.

4.4.2 Hilbert transforms and Aben's method

We begin with a note on the implementation of Aben's method in its current version. The reconstruction algorithm by Aben et al. consists of two steps. First scalar Radon data is obtained from the photoelastic tomography measurements by integration and differentiation of the data. Finally, a Radon transform inversion is carried out using any standard method, typically filtered backprojection. Using the decomposition of the ramp filter from (2.33), these steps may be combined. We describe the case for recovering f_{33} from data acquired by a tomography scan around the axis $\eta = e_3$. Aben's method works with a fixed view and so we also consider the case $K^i_\eta f(h, \theta, p) = K^i_\eta f(x_3, 0, x_1)$. The calculation of the Radon data,

$$\int f_{33}\ dx_2 = \frac{\partial}{\partial x_3} \int_{-\infty}^{X} K^1_\eta f\ dx_1 - K^2_\eta f, \tag{4.34}$$

includes an integration in the x_1 direction. In the notation of Radon transform inversion, for rays along the vector θ, we have

$$\begin{aligned} R_\theta f_{11}(p) &= R_\theta f_{11}(x_1) \\ &= \frac{\partial}{\partial x_3} \int_{-\infty}^{X} K^1_\eta f\ dx_1 \\ &= \int_{-\infty}^{X} \frac{\partial}{\partial x_3} K^1_\eta f\ dx_1. \end{aligned} \tag{4.35}$$

The first step of an FBP Radon transform inversion involves applying a ramp filter:

$$\begin{aligned} I^{-1} R_\theta f_{11} &= \mathcal{H} \frac{\partial}{\partial p} R_\theta f_{33} \\ &= \mathcal{H} \frac{\partial}{\partial x_1} R_\theta f_{33} \\ &= -\mathcal{H} \frac{\partial}{\partial x_3} K^1_\eta f \end{aligned} \tag{4.36}$$

From the point of view of implementation stability, this is clearly better than performing a numerical integration followed by a ramp filter. Moreover, this illustrates the possibility of replacing filtered backprojection by a two step Hilbert reconstruction. In this case, only a derivative is required on the data side. Rewriting (4.36) for this case we have

$$\begin{aligned} \frac{\partial}{\partial p} R_\theta f_{11} &= \frac{\partial}{\partial x_1} R_\theta f_{33} \\ &= -\frac{\partial}{\partial x_3} K_\eta^1 f, \end{aligned} \tag{4.37}$$

and the local dependence is preserved. We may thus use this technique in any measurement setting where two step Hilbert reconstruction is available, including the situation illustrated in Figure 2.10.

4.5 Summary

We have presented a new reconstruction algorithm for photoelastic tomography of purely potential stress fields. Though a more general reconstruction procedure is known, the new algorithm lends itself to a much easier and more efficient implementation. Using the new algorithm it is now also possible to achieve partial reconstructions using only parts of the data. From rays parallel to only one axis η, the $\eta \cdot f\eta$ component of the stress tensor can be recovered. The new reconstruction algorithm has been implemented numerically, and a simple study of its stability with respect to noise was also carried out.

Further, we have provided a derivation of Aben's reconstruction algorithm for solenoidal tensors, set in a mathematical framework rather than the notion of balance of forces. We have shown that the new general reconstruction method yields a reconstruction algorithm which is different from Aben's in the solenoidal case. Used together, the two algorithms give rise to an integrability condition on the data for solenoidal tensor fields.

Finally, we have used results from scalar Radon transforms to extend the new algorithms to certain cases of truncated data.

While these new algorithms provide new theoretical inversion methods, further work is required before we are able to give results of practical implementations of these. In the next chapter we present the results of some numerical work, but only for the general reconstruction algorithm from Chapter 3.

Chapter 5

Numerical Results

5.1 Forward model

In order to test our algorithms we first develop a simulator in order to generate data sets. This will take discretized permittivity tensor fields and calculate integrals of projections, as described by the operator Q in (3.13). Though we simulate an experimental setup similar to the one described in [27], we calculate the values of K^i directly rather than the light intensities measured by that system. Using a vector to represent the tensor field, we describe the action of the operator Q as multiplication by a matrix L. Even for small values of the parameters of discretization this matrix is enormous, and much too large to store in RAM all at once. Instead of calculating the whole matrix, we generate it one row at a time, corresponding to one individual source-detector pair. Multiplying each generated row r_i by the image vector x, we build up the value of Lx, as illustrated in Figure 5.1. Once we calculate $r_i \cdot x$, we store this single value and may discard r_i to free up the memory again.

$$\begin{pmatrix} & r_1 & \\ & r_2 & \\ & \vdots & \\ & r_n & \end{pmatrix} \begin{pmatrix} \\ x \\ \\ \end{pmatrix} = \begin{pmatrix} r_1 \cdot x \\ r_2 \cdot x \\ \vdots \\ r_n \cdot x \end{pmatrix}$$

Figure 5.1: Matrix multiplication by generating one row at a time

Later we will show that code used to generate the rows of L may also be used to calculate $L^T x$. With minor modifications this enables us to use the code as a backprojector.

5.1.1 Discrete representation of the tensor field

The discretized tensor field is represented by an $N \times N \times N \times 6$ array, containing the 6 distinct values of the symmetric tensor field in each voxel. We store this as a vector by listing each value, incrementing first the tensor component number, and then x, y and finally z position. Similarly, the data is represented by an $n_\eta \times n_\theta \times h \times w \times 2$ array, where we use n_η separate axes, n_θ angle steps for tomographic acquisition around each axis and use a camera with $h \times w$ pixels. The factor of 2 is the number of independent values of Qf in (5.14) which are integrated along each ray.

5.1.2 Simulated experimental setup

We simulate an experimental setup with parallel light beams passing through a specimen. Sources and detectors consist of arrays in an equally spaced grid, either side of the object being scanned, as illustrated in Figure 5.2. To match the CCD camera in the experimental system, the width to height ratio for the detector is 4:3. The source-detector pair is kept fixed and the object is rotated. For tomographic acquisition we always rotate around the z-axis and when other tomography axes are needed, we rotate the specimen accordingly. This simplifies the calculation of tensor projections P_η.

5.1.3 Location of specimen

The location of the specimen relative to the coordinate reference frame is given by an affine transformation. We store this in an augmented matrix for each axis of rotation. For the coordinate transformation $y = Ax + b$ the augmented matrix equation is

$$\left(\begin{array}{c} y \\ \hline 1 \end{array}\right) = \left(\begin{array}{c|c} A & b \\ \hline 0 \cdots 0 & 1 \end{array}\right) \left(\begin{array}{c} x \\ \hline 1 \end{array}\right). \tag{5.1}$$

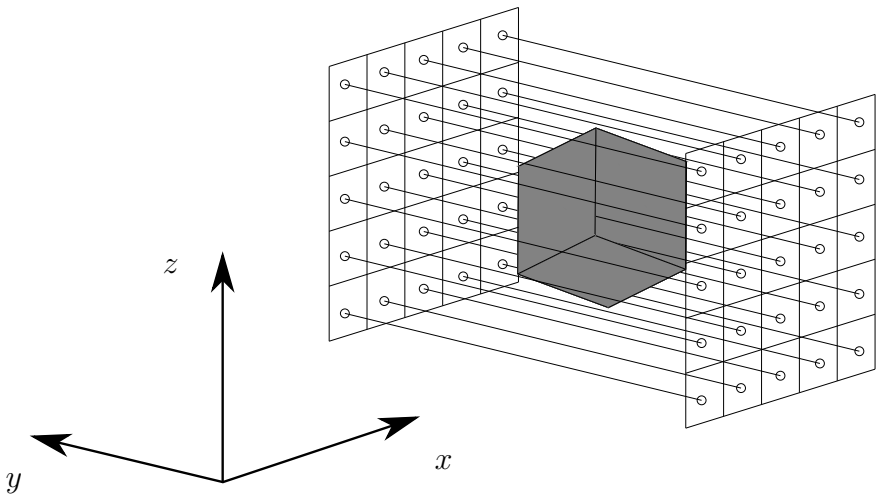

Figure 5.2: Simulated experimental setup

5.1.4 Ray path through voxel grid

The first task is to calculate the integral along a line through a voxel grid. We use the method developed by Siddon [25] in a form revised for modern CPUs by Jacobs et al. [10]. This method considers the voxels as volumes separated by the intersections of planes and calculates the intersection of a line segment with these planes. The advantage is that, whereas the number of voxels in a grid of size $n \times n \times n$ scales by n^3, the number of planes scales linearly. We outline the method below in a two-dimensional setting, which is easier to describe and readily extends to three dimensions.

The idea is to parameterize the line segment and consider the difference in the parameter value between consecutive planes (lines) of a given orientation defining the voxels (pixels). Consider the following setup, illustrated in Figure 5.3. We have a pixel grid of a certain size, defined by N_x lines in the x direction and N_y lines in the y direction. The spacing between the lines is given by d_x and d_y and the first planes intersect at the point (b_x, b_y). The line segment extends from (x_1, y_1) to (x_2, y_2) and is represented in parametric form as

$$x(\alpha) = x_1 + \alpha(x_2 - x_1) \tag{5.2}$$

$$y(\alpha) = y_1 + \alpha(y_2 - y_1). \tag{5.3}$$

We assume the ray is in a generic position, in the sense that $x_1 \neq x_2$ and $y_1 \neq y_2$, both of which are trivial to handle. The intersection points of the ray with the sides of the pixel grid are labelled $\alpha_{\min}$ and $\alpha_{\max}$. We will only need the case when the line segment starts and ends outside the grid, but for segments that start or end inside the grid we set $\alpha_{\min}$ or $\alpha_{\max}$ to 0 or 1, respectively.

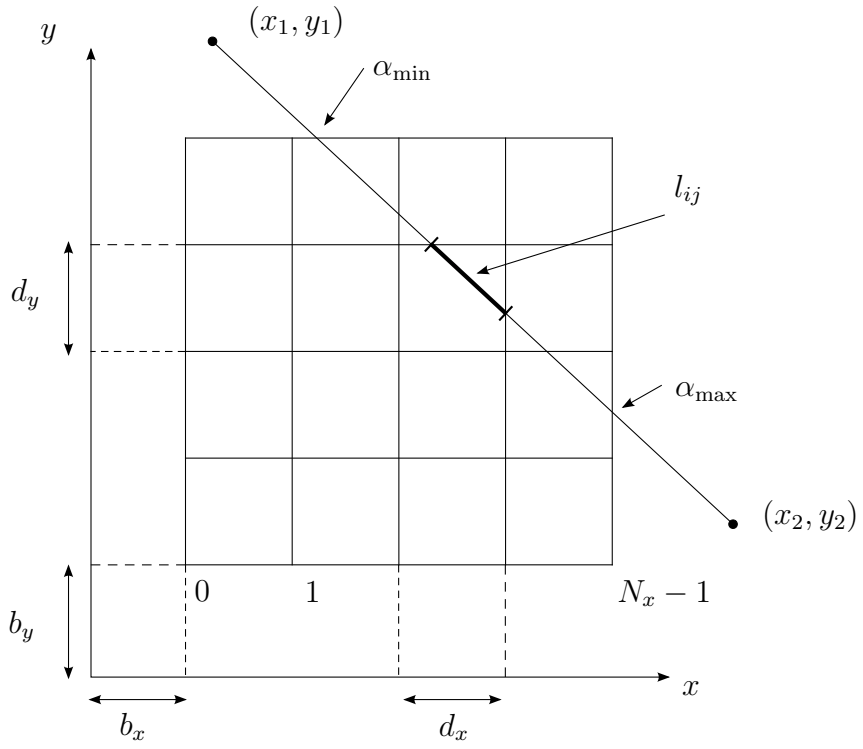

Figure 5.3: Setup for calculation of line integrals, as described in [10]

From the definition of α we may calculate its value at the intersection of the ray with a given plane as follows: For planes parallel to the x-axis, we have $\alpha = \alpha_x(i)$, and for planes parallel to the y-axis, we have $\alpha = \alpha_y(j)$, where

$$\alpha_x(i) = \frac{(b_x + id_x) - x_1}{x_2 - x_1}, \quad \text{and} \tag{5.4}$$

$$\alpha_y(j) = \frac{(b_y + jd_y) - y_1}{y_2 - y_1}. \tag{5.5}$$

We then have

$$\alpha_{\min} = \max(0,\ \alpha_{x\min},\ \alpha_{y\min}), \quad \text{and} \tag{5.6}$$

$$\alpha_{\max} = \min(1,\ \alpha_{x\max},\ \alpha_{y\max}), \tag{5.7}$$

where

$$\alpha_{x\min} = \min(\alpha_x(1),\ \alpha_x(N_x)), \tag{5.8}$$

$$\alpha_{x\max} = \max(\alpha_x(1),\ \alpha_x(N_x)), \tag{5.9}$$

$$\alpha_{y\min} = \min(\alpha_y(1),\ \alpha_y(N_y)), \quad \text{and} \tag{5.10}$$

$$\alpha_{y\max} = \max(\alpha_y(1),\ \alpha_y(N_y)). \tag{5.11}$$

Having found $\alpha_{\min}$ and $\alpha_{\max}$, we calculate the pixel through which the ray enters the grid system. We also calculate the increment in α between successive planes in both the x and y directions. Finally, we step through the grid, in each case noting which axis the next boundary crossed by the ray is parallel to and update accordingly. The length of the ray path through any given pixel l_{ij} is given by the difference between consecutive values of α. We continue stepping while $\alpha \leq \alpha_{\max}$.

Note that all the work is done in the setup, a single time for each ray. The contribution of each voxel to the ray path may then be calculated very fast by following the ray step by step through the grid in an algorithm that scales linearly with the side length of the voxel grid. Clearly only a small fraction of the voxels contribute to the integral along any given ray, so we store these values as a sparse vector.

Once the contribution of each voxel to the total integral for a given ray is known, we are able to calculate integrals along that ray. We denote the operator taking an image vector x to its line integrals by $\tilde{L}$. We make use of $\tilde{L}$ to calculate scalar back-projections. For simulating photoelastic data however, some more work is required to evaluate the functions to be integrated.

5.1.5 Projection of the tensor field

From a given tensor we need to calculate the projection onto the plane perpendicular to the ray. To simplify this, we rotate our coordinate system to align the ray with

the y-axis. In this reference frame, the projection of the tensor

$$f = \begin{pmatrix} f_{11} & f_{12} & f_{13} \\ f_{12} & f_{22} & f_{23} \\ f_{13} & f_{22} & f_{33} \end{pmatrix} \tag{5.12}$$

onto the plane perpendicular to the ray is given by

$$P_\eta f = \begin{pmatrix} f_{11} & 0 & f_{13} \\ 0 & 0 & 0 \\ f_{13} & 0 & f_{33} \end{pmatrix}. \tag{5.13}$$

Finally, we have

$$Q_\eta f = \begin{pmatrix} \frac{1}{2}(f_{11} - f_{33}) & 0 & f_{13} \\ 0 & 0 & 0 \\ f_{13} & 0 & -\frac{1}{2}(f_{11} - f_{33}) \end{pmatrix}. \tag{5.14}$$

As $Q_\eta f$ only contains two independent values, $g_1 = \frac{1}{2}(f_{11} - f_{33})$ and $g_2 = f_{13}$ say, we extract these and integrate along each ray. Having calculated the contribution of each voxel to the integral, we simply multiply the vector of g_i by the corresponding weight for each voxel and sum.

5.1.6 Backprojection

With minor modification we may reuse the same code to carry out scalar backprojection. Since it is the dual operator of ray integration $\tilde{L}$, backprojection is given by $\tilde{L}^T$. Our code generates rows of the matrix $\tilde{L}$, but we may use these to calculate $x = \tilde{L}^T y$ as follows: Let the size of $\tilde{L}$ be $m \times n$, and write $y = (y_1, y_2, \ldots, y_m)$. We initialize x to the zero vector of length n. Then for $i = 1, \ldots, n$ we calculate r_i of $\tilde{L}$ and add $y_i r_i$ to x. When this procedure is complete we have $x = \tilde{L}^T y$.

5.2 Data simulation

The model described above simulates the interaction of light with a stressed photoelastic object. We generate two different strain field phantoms to use as input to the

forward projector. The first one has only smooth features and is expected to be less sensitive to algorithm instabilities. The second phantom contains sharp edges and is designed to highlight the limitations of the unstable reconstruction algorithm. A detailed description of the number of voxels and pixels used, along with simulated noise and other steps taken to avoid "inverse crime" is given in Section 5.2.3.

5.2.1 Phantom 1: smooth

Phantom 1 is constructed from smooth Gaussians which makes it relatively easy to reconstruct. We start with a cube with sides consisting of the interval $[-1, 1]$, valued zero everywhere. We then add 3-dimensional Gaussians $b(x)$ to the different tensor components f_{ij} according to Table 5.1, where

$$b(x) = \text{Exp}\left(-50\left[(x - x_0)^2 + (y - y_0)^2 + (z - z_0)^2\right]\right). \tag{5.15}$$

Finally, we remove the hydrostatic part of the phantom, to produce the phantom illustrated in Figure 5.4.

i	j	x_0	y_0	z_0
1	1	-0.5	-0.5	-0.5
1	2	-0.5	-0.5	0.5
1	3	-0.5	0.5	-0.5
2	2	-0.5	0.5	0.5
2	3	0.5	-0.5	-0.5
3	3	0.5	-0.5	0.5

Table 5.1: Phantom 1: Smooth

5.2.2 Phantom 2: sharp edges

Phantom 2 is constructed to contain sharp edges, which are more sensitive to instabilities in the reconstructions. We start again with a cube with sides consisting of the interval $[-1, 1]$, valued zero everywhere. We set the value inside certain cuboids

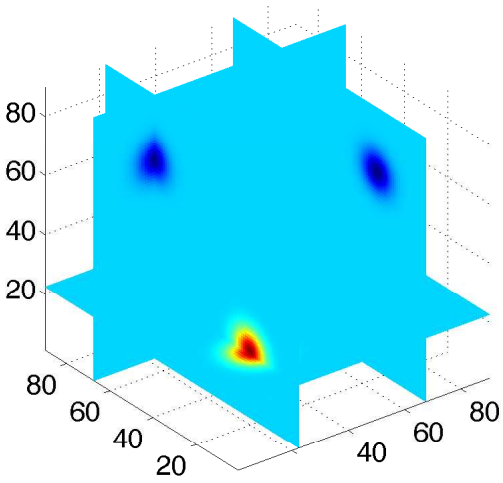

(a) f_{11}

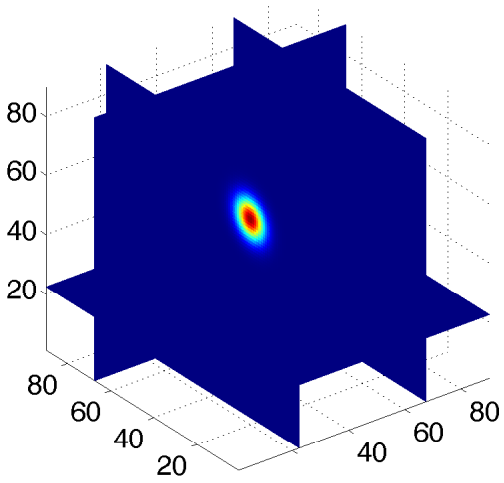

(b) f_{12}

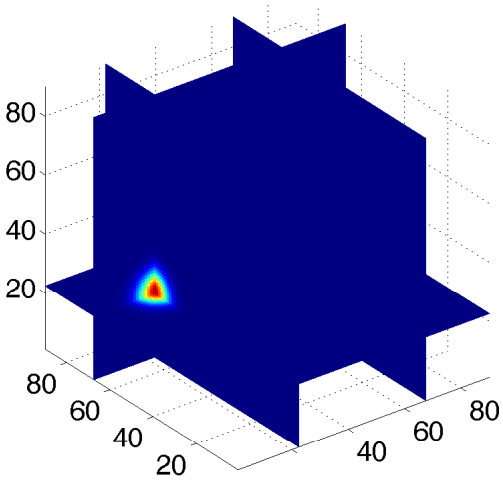

(c) f_{13}

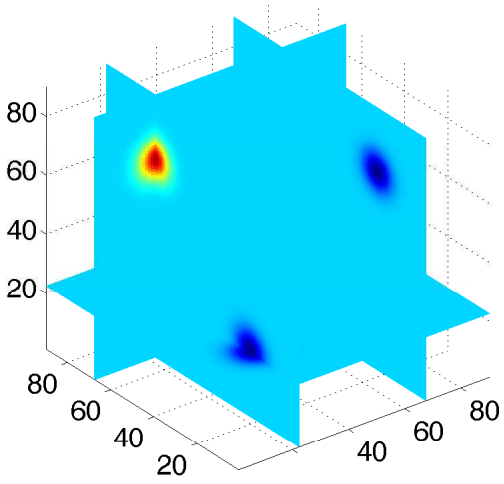

(d) f_{22}

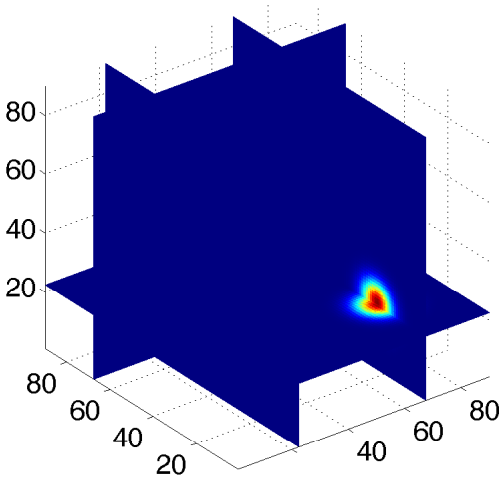

(e) f_{23}

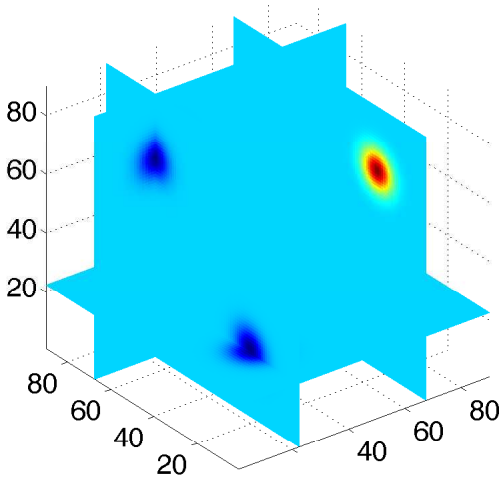

(f) f_{33}

Figure 5.4: Phantom 1: Smooth

to 1, according to Table 5.2. Finally, we remove the hydrostatic part of the phantom, to produce the phantom illustrated in Figure 5.5.

i	j	x_0	y_0	z_0
1	1	[-0.4, 0.4]	[-0.6, 0.2]	[-0.8, 0.8]
1	2	[-0.4, 0.4]	[-0.2, 0.6]	[-0.8, 0.8]
1	3	[-0.8, 0.8]	[-0.4, 0.4]	[-0.6, 0.2]
2	2	[-0.8, 0.8]	[-0.4, 0.4]	[-0.2, 0.6]
2	3	[-0.6, 0.2]	[-0.8, 0.8]	[-0.4, 0.4]
3	3	[-0.2, 0.6]	[-0.8, 0.8]	[-0.4, 0.4]

Table 5.2: Phantom 2: Sharp edges

5.2.3 Sample projection images

Figure 5.6 shows some sample projection images from Phantom 2 for a single axis of rotation at various points of rotation around the axis.

For our numerical experiments, phantoms were generated inside a cubic grid measuring $243 \times 243 \times 243$ voxels, and measurements were simulated for a pixel grid with 387×516 pixels. The pixel grid was then down-sampled by a factor of 3 to 129×172 pixels by binning. Finally, Gaussian random noise was added to each pixel corresponding to a 1% noise level for each projection image. The final reconstruction was carried out on a voxel grid measuring $90 \times 90 \times 90$. Note that this does not evenly divide the size of the original grid. The number of angle steps used was varied depending on the number of rotation axes used, in order to use the same total amount of data. A total of 1080 projections were collected, which for 6 rotation axes corresponds to 180 angle steps per rotation axis. Since our reconstructions are unique, we do not expect any artefacts outside the support of our original phantom and so we restrict the reconstructed region to match the phantoms.

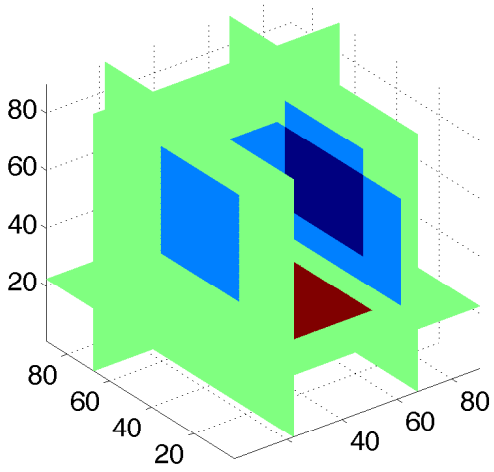

(a) f_{11}

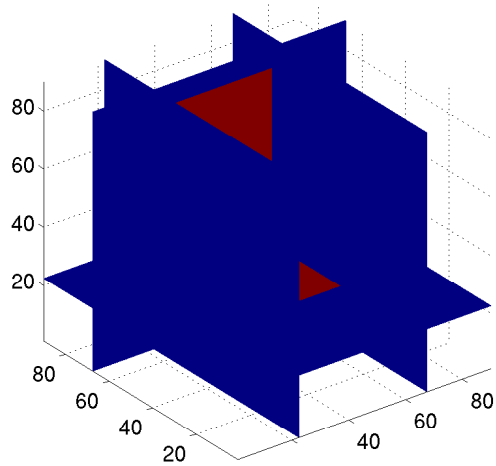

(b) f_{12}

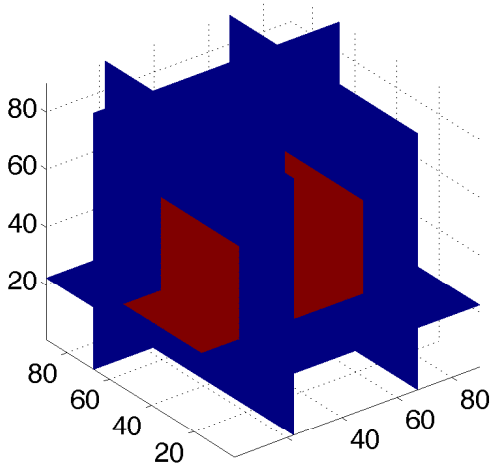

(c) f_{13}

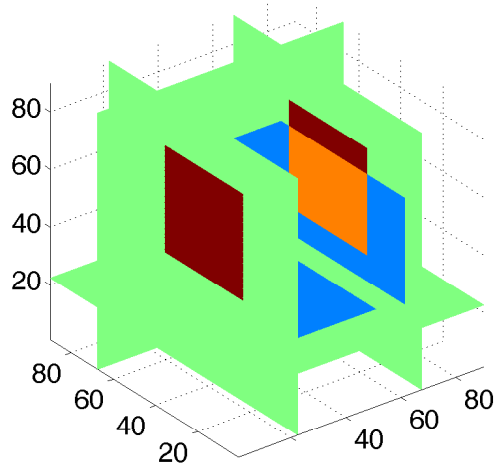

(d) f_{22}

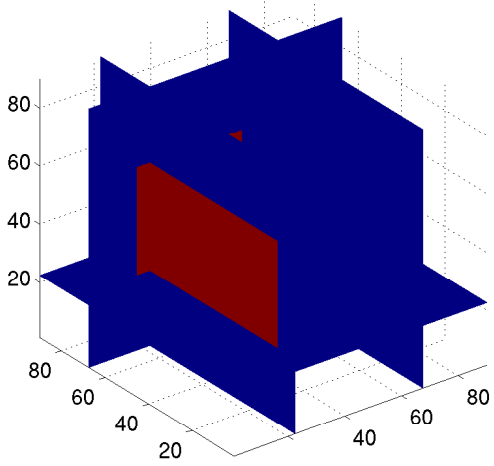

(e) f_{23}

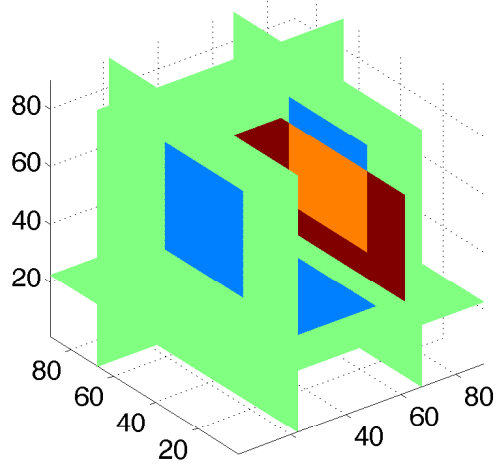

(f) f_{33}

Figure 5.5: Phantom 2: Sharp edges

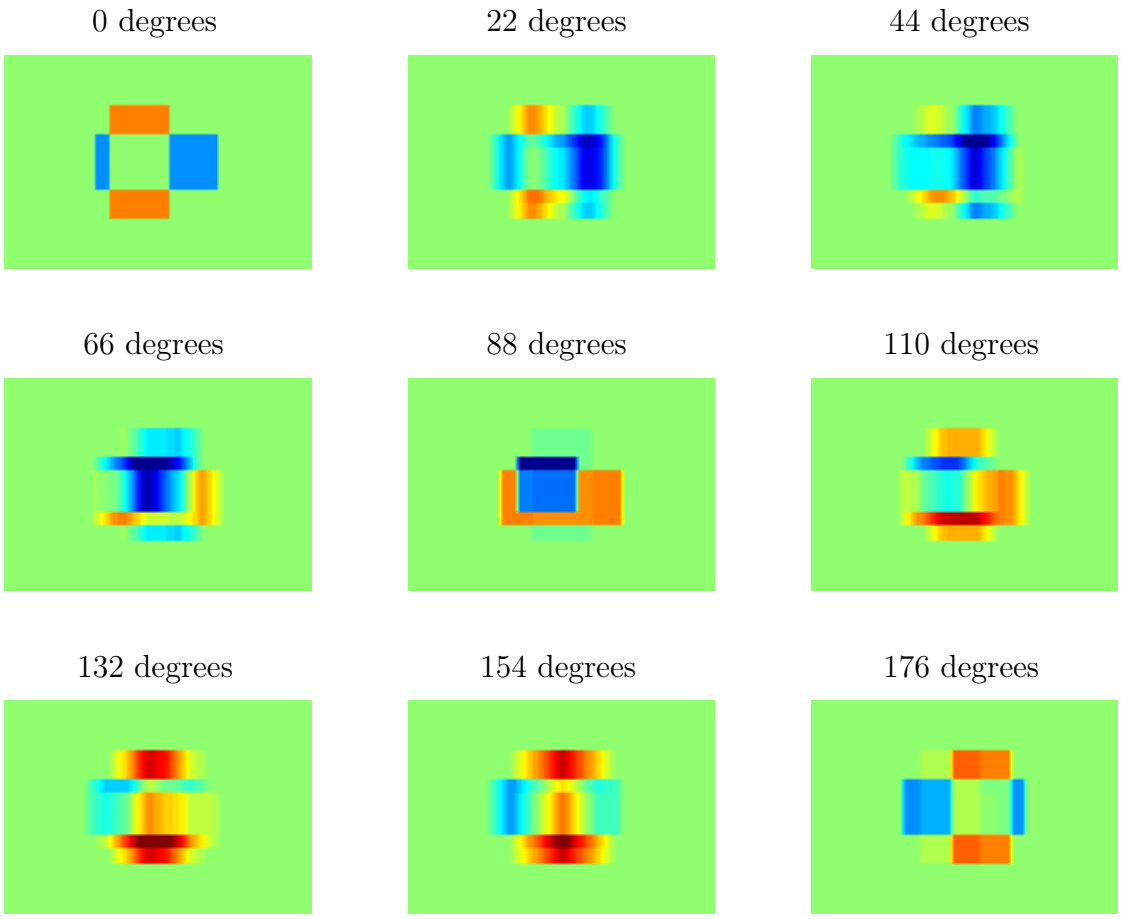

Figure 5.6: Sample projection images

5.3 Algorithm implementation

Given (simulated) data K^1 and K^2, the reconstruction procedure is as follows:

5.3.1 Stable reconstruction using data from 6 axes

Step 1

We start with

$$\lambda_\eta = \frac{i}{2}|P_\eta y|\left(B_\eta \widehat{\frac{\partial K_\eta^1 f}{\partial p}}\right) \tag{5.16}$$

$$\mu_\eta = |P_\eta y|^3(\widehat{B_\eta K_\eta^2 f}) \tag{5.17}$$

Instead of calculating λ and μ, we write

$$\lambda_\eta = \frac{i}{2}|P_\eta y|\tilde{\lambda_\eta} \tag{5.18}$$

$$\mu_\eta = |P_\eta y|^2 \tilde{\mu_\eta}. \tag{5.19}$$

This way, $\tilde{\lambda_\eta}$ is given by a slice-by-slice differentiated backprojection and $\tilde{\mu_\eta}$ is given by a slice-by-slice filtered backprojection. For $\tilde{\mu_\eta}$ we make use of (2.15), which shows that in each plane, the ramp filter commutes with the backprojection. The final filters are incorporated into the calculations of $\hat{f}_{ij}$ from λ and μ, since that already involves algebraic equations in the Fourier domain.

The projection images K^1 need to be differentiated in the p-direction. We perform a regularised derivative, which we carry out in the Fourier domain using a Hamming window regularisation: After a one dimensional Fast Fourier Transform (FFT) we multiply by $-itw(t)$, where w is the Hamming window of (2.23). Finally, we use the inverse FFT to move the signal back to the image domain.

Following the filter we backproject the filtered data onto the voxel grid using the method described in Section 5.1.6. Finally, $\tilde{\mu}_\eta$ is calculated using a three dimensional FFT.

For the data K^2 we carry out a ramp filter, again in the Fourier domain using a Hamming window for regularisation. As with K^1 we then backproject onto the voxel grid and again finish with a three dimensional FFT.

Step 2

We now have the value of $\tilde{\lambda_\eta}$ and $\tilde{\mu_\eta}$ on a voxel grid. To proceed we need to solve the system (3.27), using (5.18)-(5.19) to substitute $\tilde{\mu_\eta}$ for μ_η.

Mathematica may be used to invert the system (3.27) for $\hat{f}_{ij}$ $(i \neq j)$. The results are given by (5.20)-(5.22).

$$
\begin{aligned}
\hat{f}_{12} = \\
(\big(-y_1(2y_1^2 + (y_2 - y_3)^2)y_3(y_1^2 + y_3^2)\big)\tilde{\mu}_1 + \\
\big(-y_2(2y_2^2 + (y_1 - y_3)^2)y_3(y_2^2 + y_3^2)\big)\tilde{\mu}_2 + \\
\big((y_1^2 + y_1y_2 + y_2^2 + y_3^2)^2((y_1 - y_2)^2 + 2y_3^2)\big)\tilde{\mu}_3 + \\
\big(y_1y_3(y_1^2 + y_3^2)(2y_1^2 + (y_2 + y_3)^2)\big)\tilde{\mu}_4 + \\
\big(y_2y_3(y_2^2 + y_3^2)(2y_2^2 + (y_1 + y_3)^2)\big)\tilde{\mu}_5 + \\
\big((y_1^2 + y_1y_2 + y_2^2 + y_3^2)^2((y_1 + y_2)^2 + 2y_3^2)\big)\tilde{\mu}_6 \ ) / \\
4(y_1^6 + y_2^6 + 2y_2^4y_3^2 + 2y_2^2y_3^4 + y_3^6 + 2y_1^4(y_2^2 + y_3^2) + y_1^2(2y_2^2 + y_3^2)(y_2^2 + 2y_3^2))
\end{aligned}
\tag{5.20}
$$

$$
\begin{aligned}
\hat{f}_{13} = \\
(- y_1y_2(y_1^2 + y_2^2)(2y_1^2 + (y_2 - y_3)^2)\tilde{\mu}_1 + \\
(2y_2^2 + (y_1 - y_3)^2)(y_1^2 + y_2^2 - y_1y_3 + y_3^2)(y_1^2 + y_2^2 + y_1y_3 + y_3^2)\tilde{\mu}_2 + \\
-y_2y_3(y_2^2 + y_3^2)((y_1 - y_2)^2 + 2y_3^2)\tilde{\mu}_3 + \\
y_1y_2(y_1^2 + y_2^2)(2y_1^2 + (y_2 + y_3)^2\tilde{\mu}_4) + \\
-(y_1^2 + y_2^2 - y_1y_3 + y_3^2)(y_1^2 + y_2^2 + y_1y_3 + y_3^2)(2y_2^2 + (y_1 + y_3)^2)\tilde{\mu}_5 + \\
y_2y_3(y_2^2 + y_3^2)((y_1 + y_2)^2 + 2y_3^2)\tilde{\mu}_6 \ ) / \\
4(y_1^6 + y_2^6 + 2y_2^4y_3^2 + 2y_2^2y_3^4 + y_3^6 + 2y_1^4(y_2^2 + y_3^2) + y_1^2(2y_2^2 + y_3^2)(y_2^2 + 2y_3^2))
\end{aligned}
\tag{5.21}
$$

$$
\begin{aligned}
\hat{f}_{23} = \\
\big((2y_1^2 + (y_2 - y_3)^2)\ (y_1^2 + y_2^2 - y_2y_3 + y_3^2)(y_1^2 + y_2^2 + y_2y_3 + y_3^2)\tilde{\mu}_1 + \\
-y_1y_2(y_1^2 + y_2^2)(2y_2^2 + (y_1 - y_3)^2)\tilde{\mu}_2 + \\
-y_1y_3(y_1^2 + y_3^2)((y_1 - y_2)^2 + 2y_3^2)\tilde{\mu}_3 + \\
-(y_1^2 + y_2^2 - y_2y_3 + y_3^2)(y_1^2 + y_2^2 + y_2y_3 + y_3^2)(2y_1^2 + (y_2 + y_3)^2)\tilde{\mu}_4 + \\
y_1y_2(y_1^2 + y_2^2)(2y_2^2 + (y_1 + y_3)^2)\tilde{\mu}_5 + \\
y_1y_3(y_1^2 + y_3^2)((y_1 + y_2)^2 + 2y_3^2)\tilde{\mu}_6 \ ) / \\
4(y_1^6 + y_2^6 + 2y_2^4y_3^2 + 2y_2^2y_3^4 + y_3^6 + 2y_1^4(y_2^2 + y_3^2) + y_1^2(2y_2^2 + y_3^2)(y_2^2 + 2y_3^2))
\end{aligned}
\tag{5.22}
$$

Using these equations, $\hat{f}_{12}$, $\hat{f}_{13}$, and $\hat{f}_{23}$ are calculated at each voxel except at $(y_1, y_2, y_3) = (0, 0, 0)$ where it is undefined. The value in this voxel is set using a linear interpolation of the values in neighbouring voxels.

Having calculated $\hat{f}_{ij}$ $(i \neq j)$ we use these values together with $\tilde{\lambda}$ to calculate the final tensor components $\hat{f}_{ii}$. Again Mathematica may be used to substitute $\tilde{\lambda_\eta}$ for λ_η in (3.28) - (5.21), giving

$$\begin{aligned}
&\hat{f}_{11} = \\
&\frac{1}{6(y_1^2+y_2^2+y_3^2)}\Big(-8(y_1y_2f_{12}+y_1y_3f_{13}-2y_2y_3f_{23}) \\
&+i\Big(\tilde{\lambda}_2\sqrt{2y_2^2+(y_1-y_3)^2}(y_1-2y_3)+ \\
&\tilde{\lambda}_1\sqrt{2y_1^2+(y_2-y_3)^2}(y_2+y_3)+ \\
&\tilde{\lambda}_3(y_1-2y_2)\sqrt{(y_1-y_2)^2+2y_3^2}+ \\
&\tilde{\lambda}_6(y_1+2y_2)\sqrt{(y_1+y_2)^2+2y_3^2}+ \\
&-\tilde{\lambda}_5(y_1+2y_3)\sqrt{2y_2^2+(y_1+y_3)^2}+ \\
&\tilde{\lambda}_4(y_2-y_3)\sqrt{2y_1^2+(y_2+y_3)^2}\ \Big)\Big)
\end{aligned} \tag{5.23}$$

$$\begin{aligned}
&\hat{f}_{22} = \\
&\frac{1}{6(y_1^2+y_2^2+y_3^2)}\Big(-8(y_1y_2f_{12}-2y_1y_3f_{13}+y_2y_3f_{23})+ \\
&i\Big(\tilde{\lambda}_1\sqrt{2y_1^2+(y_2-y_3)^2}(y_2-2y_3)+ \\
&\tilde{\lambda}_2\sqrt{2y_2^2+(y_1-y_3)^2}(y_1+y_3)+ \\
&\tilde{\lambda}_3(-2y_1+y_2)\sqrt{(y_1-y_2)^2+2y_3^2}+ \\
&-\tilde{\lambda}_6(2y_1+y_2)\sqrt{(y_1+y_2)^2+2y_3^2}+ \\
&\tilde{\lambda}_5(-y_1+y_3)\sqrt{2y_2^2+(y_1+y_3)^2}+ \\
&\tilde{\lambda}_4(y_2+2y_3)\sqrt{2y_1^2+(y_2+y_3)^2}\ \Big)\Big)
\end{aligned} \tag{5.24}$$

$$
\begin{aligned}
&\hat{f}_{33} = \\
&\frac{1}{6(y_1^2+y_2^2+y_3^2)}(-8(-2y_1y_2f_{12}+y_1y_3f_{13}+y_2y_3f_{23}) \\
&+i\Big(\tilde{\lambda}_2\sqrt{2y_2^2+(y_1-y_3)^2}(-2y_1+y_3)+ \\
&\tilde{\lambda}_1\sqrt{2y_1^2+(y_2-y_3)^2}(-2y_2+y_3)+ \\
&\tilde{\lambda}_3(y_1+y_2)\sqrt{(y_1-y_2)^2+2y_3^2}+ \\
&\tilde{\lambda}_6(y_1-y_2)\sqrt{(y_1+y_2)^2+2y_3^2}+ \\
&\tilde{\lambda}_5(2y_1+y_3)\sqrt{2y_2^2+(y_1+y_3)^2}+ \\
&-\tilde{\lambda}_4(2y_2+y_3)\sqrt{2y_1^2+(y_2+y_3)^2}\ \Big)\Big).
\end{aligned}
\tag{5.25}
$$

Again, the values of f_{11}, f_{22}, and f_{33} at $(y_1, y_2, y_3) = (0, 0, 0)$ is not defined by (5.23)-(5.25) and as above we use a linear interpolation from neighbouring voxels.

Finally, we use the three dimensional inverse FFT to recover f_{ij} from $\hat{f}_{ij}$. Results for our phantoms are shown in Section 5.4.

5.3.2 Unstable reconstruction using data from 3 axes

Step 1

We begin as in Section 5.3.1 to compute $\tilde{\lambda}$ and $\tilde{\mu}$ on a voxel grid.

Step 2

To proceed with the unstable reconstruction formula we need to solve the system (3.25). This system separates and we first use the initial three equations to solve for $\hat{f}_{ij}$ $(i \neq j)$. As before we use (5.18) to substitute $\tilde{\lambda}$ for λ and solve the system using Mathematica. The result is given by (5.26)-(5.28).

Given $\hat{f}_{ij}$ $(i \neq j)$ we may carry out the substitution (5.19) and invert the last three equations of (3.25) to obtain $\hat{f}_{ii}$, which are given by (5.29)-(5.31).

$$\hat{f}_{12} = \frac{\tilde{\lambda}_2 y_2 \sqrt{2y_2^2 + (y_1 - y_3)^2} + \tilde{\lambda}_1 y_1 \sqrt{2y_1^2 + (y_2 - y_3)^2} - \tilde{\lambda}_3 y_3 \sqrt{2y_3^2 + (y_1 - y_2)^2})}{2\sqrt{2} y_1 y_2} \tag{5.26}$$

$$\hat{f}_{13} = \frac{\tilde{\lambda}_1 y_1 \sqrt{2y_1^2 + (y_2 - y_3)^2} - \tilde{\lambda}_2 y_2 \sqrt{2y_2^2 + (y_1 - y_3)^2} + \tilde{\lambda}_3 y_3 \sqrt{2y_3^2 + (y_1 - y_2)^2}}{2\sqrt{2} y_1 y_3)} \tag{5.27}$$

$$\hat{f}_{23} = \frac{-\tilde{\lambda}_1 y_1 \sqrt{2y_1^2 + (y_2 - y_3)^2} + \tilde{\lambda}_2 y_2 \sqrt{2y_2^2 + (y_1 - y_3)^2} + \tilde{\lambda}_3 y_3 \sqrt{2y_3^2 + (y_1 - y_2)^2}}{2\sqrt{2} y_2 y_3} \tag{5.28}$$

$$\begin{aligned}
\hat{f}_{11} = -\Big(&2y_1^2 y_2^2 (2f_{12} y_1 y_2 + \tilde{\mu}_3 (y_1^2 + y_2^2)) + \\
&2y_1 y_2 (-(f_{23} y_1) + f_{13} y_2)(y_1^2 + 2y_2^2) y_3 + (y_1^2 + 4y_2^2)(2f_{12} y_1 y_2 + \tilde{\mu}_3 (y_1^2 + y_2^2)) y_3^2 + \\
&4(f_{13} y_1 - f_{23} y_2)(y_1^2 + 2y_2^2) y_3^3 + 2(2f_{12} y_1 y_2 + \tilde{\mu}_3 (y_1^2 + y_2^2)) y_3^4 + \\
&-\tilde{\mu}_1 (y_1^2 + 2y_2^2)(y_2^2 + y_3^2)(y_1^2 + 2y_3^2) + \tilde{\mu}_2 (y_1^2 + 2y_2^2)(y_1^2 + y_3^2)(y_2^2 + 2y_3^2)\Big) \\
&\Big/ \Big(6(y_1^2 + y_2^2 + y_3^2)(y_2^2 y_3^2 + y_1^2 (y_2^2 + y_3^2))\Big)
\end{aligned} \tag{5.29}$$

$$\begin{aligned}
\hat{f}_{22} = -(&2y_1^2 y_2^2 (2f_{12} y_1 y_2 + \tilde{\mu}_3 (y_1^2 + y_2^2)) + \\
&2y_1 y_2 (f_{23} y_1 - f_{13} y_2)(2y_1^2 + y_2^2) y_3 + (4y_1^2 + y_2^2)(2f_{12} y_1 y_2 + \tilde{\mu}_3 (y_1^2 + y_2^2)) y_3^2 + \\
&-4(f_{13} y_1 - f_{23} y_2)(2y_1^2 + y_2^2) y_3^3 + 2(2f_{12} y_1 y_2 + \tilde{\mu}_3 (y_1^2 + y_2^2)) y_3^4 + \\
&\tilde{\mu}_1 (2y_1^2 + y_2^2)(y_2^2 + y_3^2)(y_1^2 + 2y_3^2) - \tilde{\mu}_2 (2y_1^2 + y_2^2)(y_1^2 + y_3^2)(y_2^2 + 2y_3^2)) \\
&\Big/ \Big(6(y_1^2 + y_2^2 + y_3^2)(y_2^2 y_3^2 + y_1^2 (y_2^2 + y_3^2))\Big)
\end{aligned} \tag{5.30}$$

$$\begin{aligned}\hat{f}_{33} = -(&-4y_1^2y_2^2(2f_{12}y_1y_2 + \tilde{\mu}_3(y_1^2 + y_2^2))+\\ &4y_1y_2(f_{13}y_2(2y_1^2 + y_2^2) + f_{23}(y_1^3 + 2y_1y_2^2))y_3+\\ &-2(y_1^2 + y_2^2)(2f_{12}y_1y_2 + \tilde{\mu}_3(y_1^2 + y_2^2))y_3^2+\\ &2(f_{13}y_1(2y_1^2 + y_2^2) + f_{23}y_2(y_1^2 + 2y_2^2))y_3^3 - (2f_{12}y_1y_2 + \tilde{\mu}_3(y_1^2 + y_2^2))y_3^4\\ &+\tilde{\mu}_1(y_1^2 + 2y_2^2)(2y_1^2 + y_3^2)(y_2^2 + y_3^2)+\\ &\tilde{\mu}_2(2y_1^2 + y_2^2)(y_1^2 + y_3^2)(2y_2^2 + y_3^2))\\ &\Big/\Big(6(y_1^2 + y_2^2 + y_3^2)(y_2^2y_3^2 + y_1^2(y_2^2 + y_3^2))\Big)\end{aligned} \tag{5.31}$$

With the equations in place, $\hat{f}_{ij}$ may be calculated at each voxel except the coordinate axes where it is undefined. The values in these voxels are set using a linear interpolation of the values in neighbouring voxels. As before we complete the reconstruction with the three dimensional inverse FFT, giving f_{ij} from $\hat{f}_{ij}$. The results for our phantoms are illustrated in the next section.

5.4 Results

Below we illustrate the results of our implemented reconstructions. The original used for comparison is regenerated on a smaller grid matching the reconstructions. Note that this is smaller than the original phantom used to generate the data. Each page shows one component of the tensor field, comparing the original phantom to the result of a reconstruction using the unstable algorithm and one using the stable algorithm. Figures 5.7 – 5.12 were made using Phantom 1, and Figures 5.13 – 5.18 were made using Phantom 2. For problems at this scale, the reconstruction time was a couple of minutes on a 2 GHz dual core AMD Opteron processor. In practice, though this time will increase, we still expect the limiting factor to be image acquisition time, which is currently over ten hours.

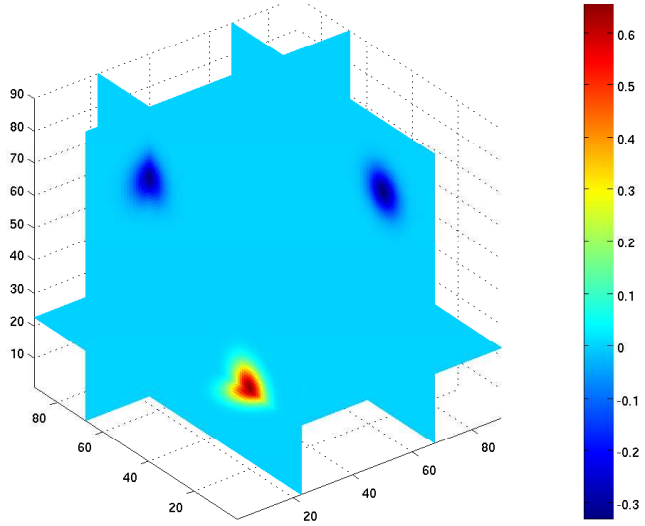

(a) Original phantom

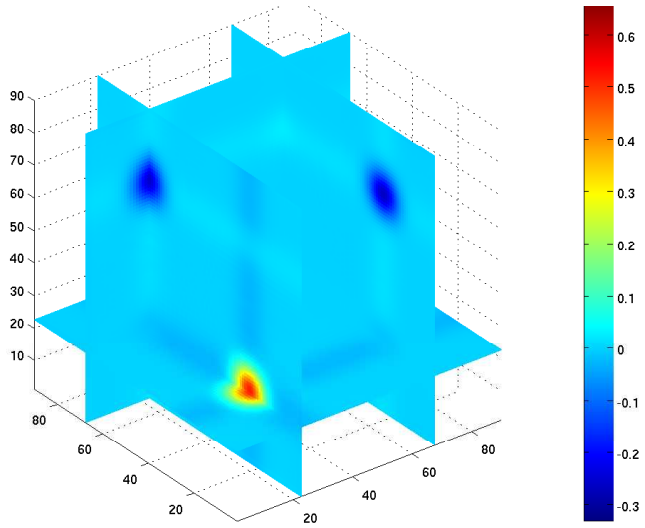

(b) Unstable reconstruction

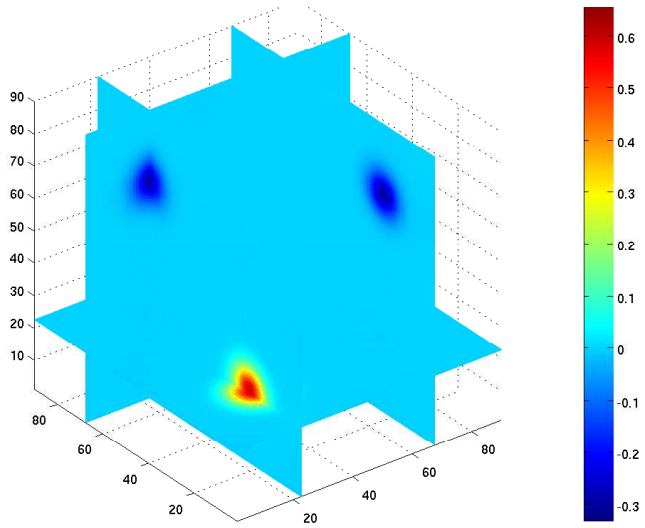

(c) Stable reconstruction

Figure 5.7: Reconstruction of Phantom 1 (smooth), f_{11}

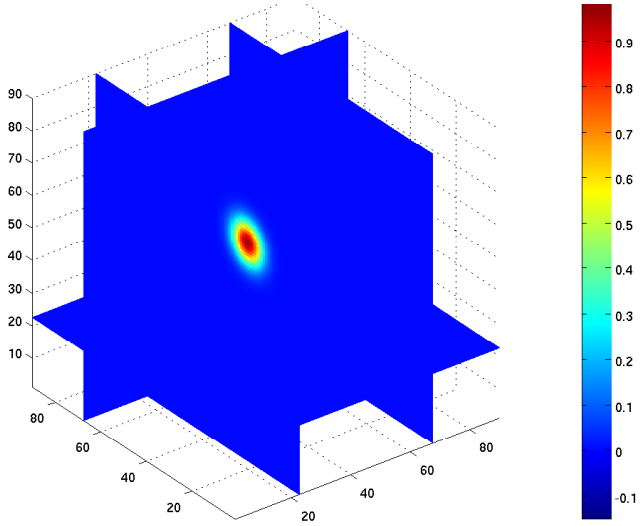

(a) Original phantom

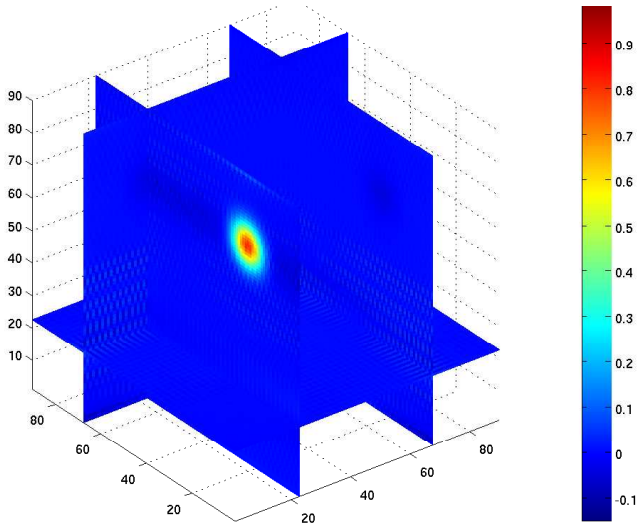

(b) Unstable reconstruction

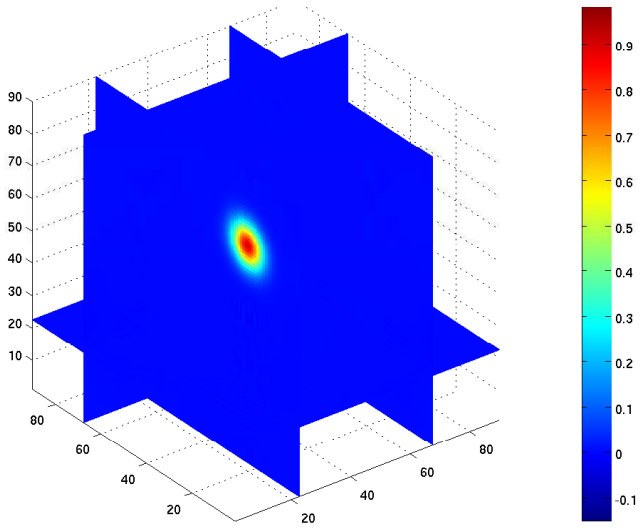

(c) Stable reconstruction

Figure 5.8: Reconstruction of Phantom 1 (smooth), f_{12}

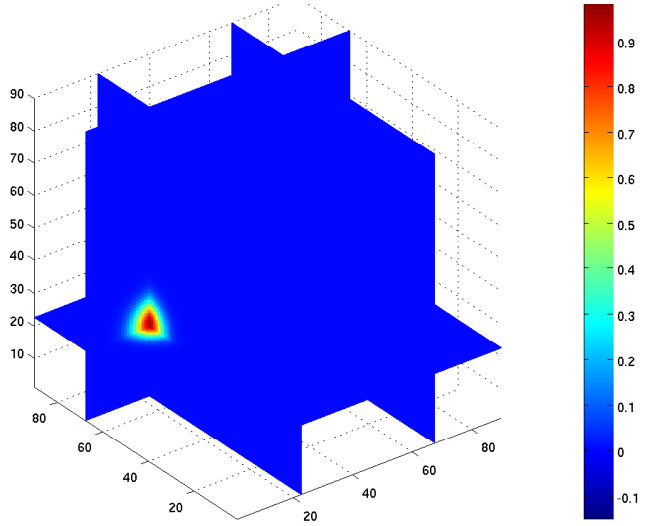

(a) Original phantom

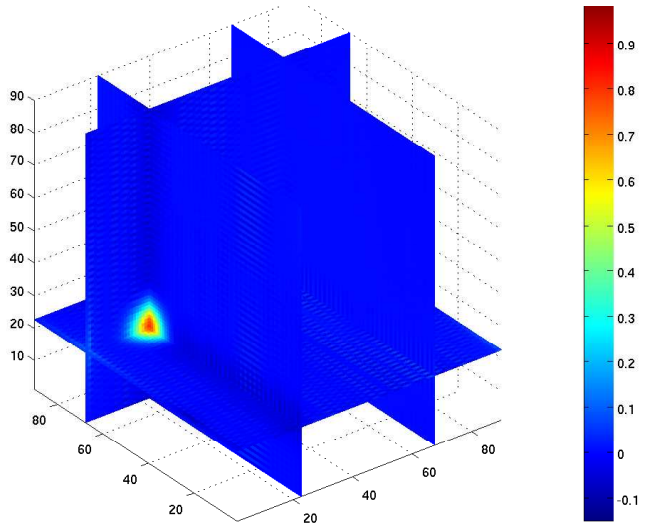

(b) Unstable reconstruction

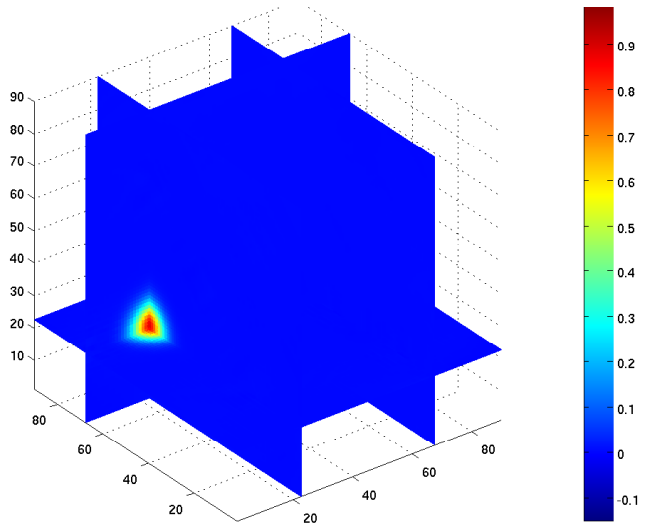

(c) Stable reconstruction

Figure 5.9: Reconstruction of Phantom 1 (smooth), f_{13}

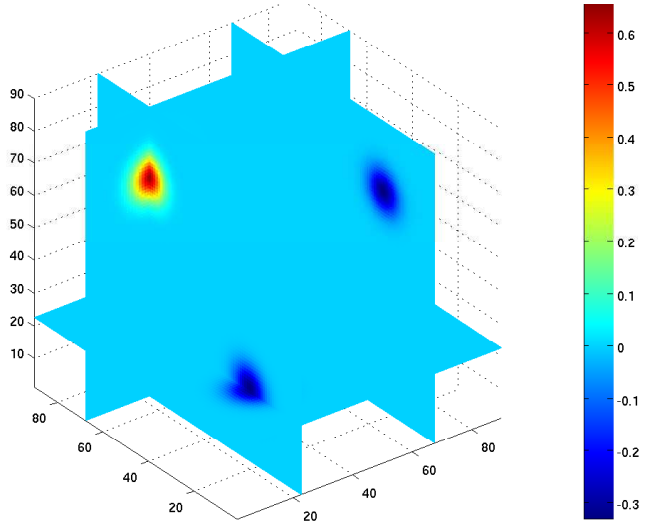

(a) Original phantom

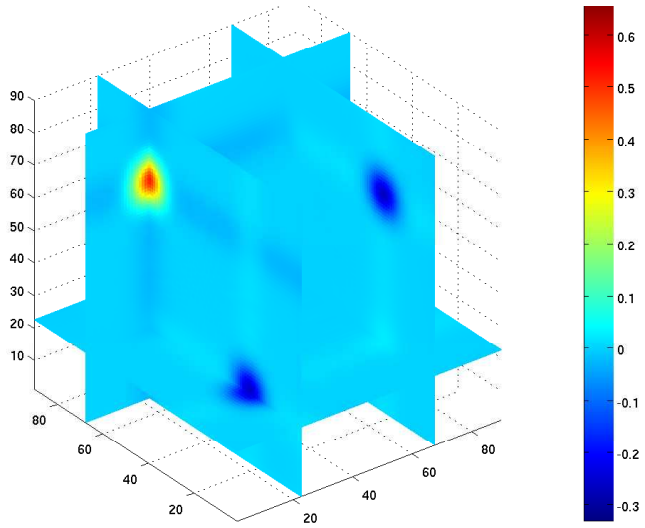

(b) Unstable reconstruction

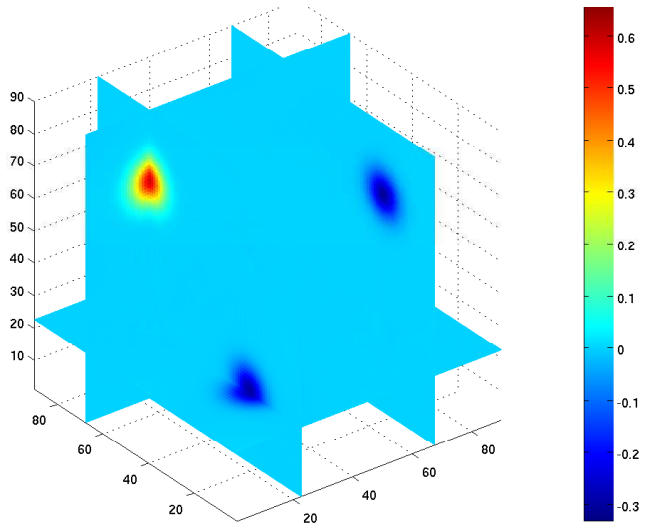

(c) Stable reconstruction

Figure 5.10: Reconstruction of Phantom 1 (smooth), f_{22}

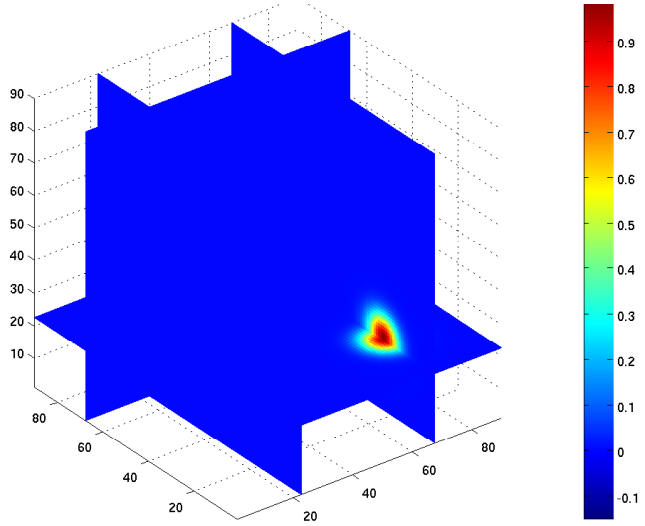

(a) Original phantom

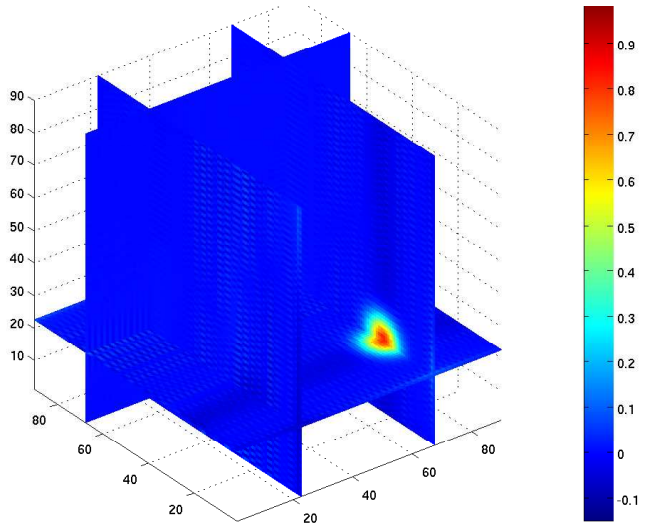

(b) Unstable reconstruction

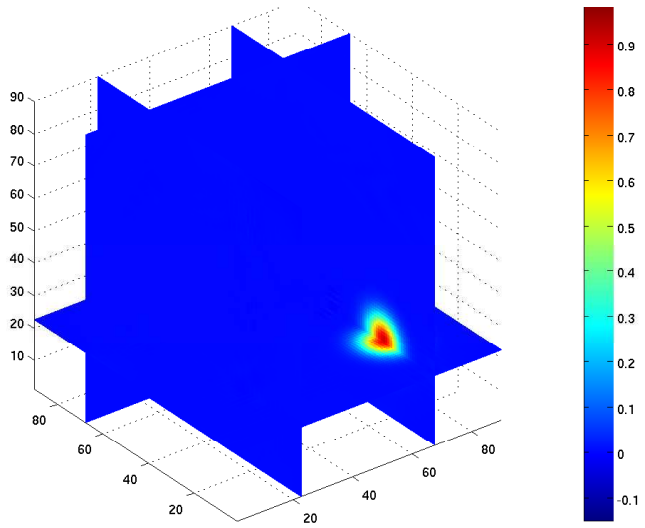

(c) Stable reconstruction

Figure 5.11: Reconstruction of Phantom 1 (smooth), f_{23}

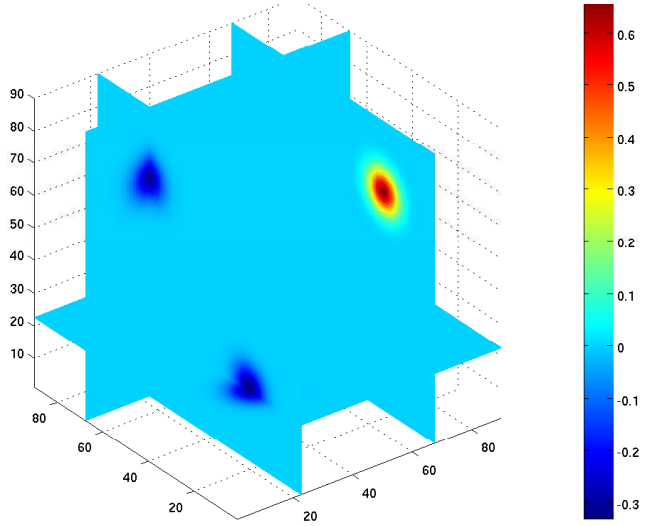

(a) Original phantom

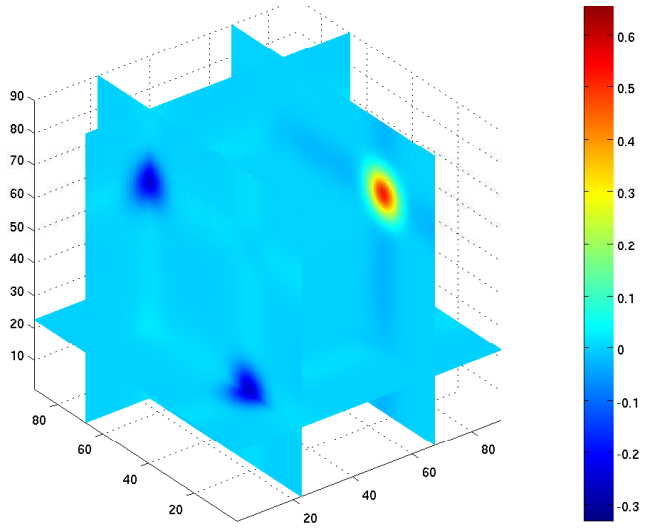

(b) Unstable reconstruction

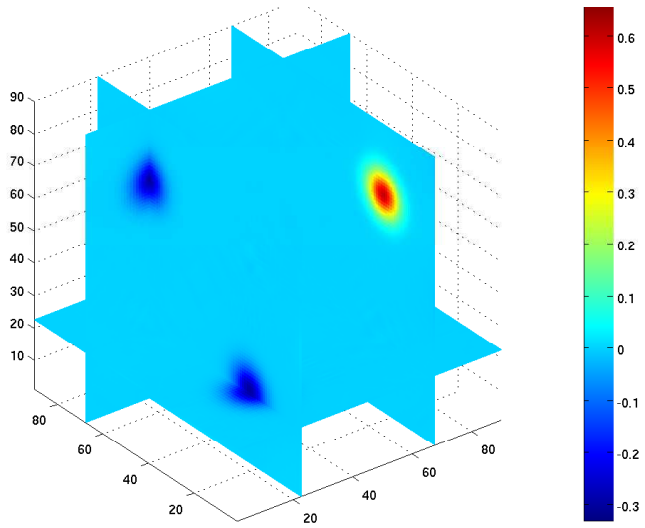

(c) Stable reconstruction

Figure 5.12: Reconstruction of Phantom 1 (smooth), f_{33}

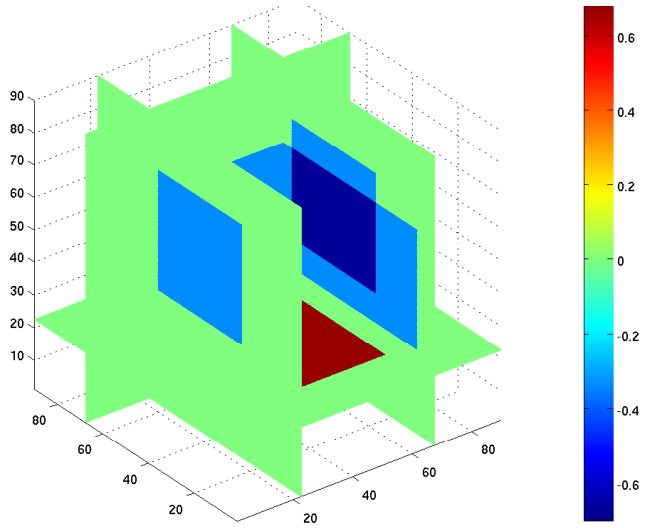

(a) Original phantom

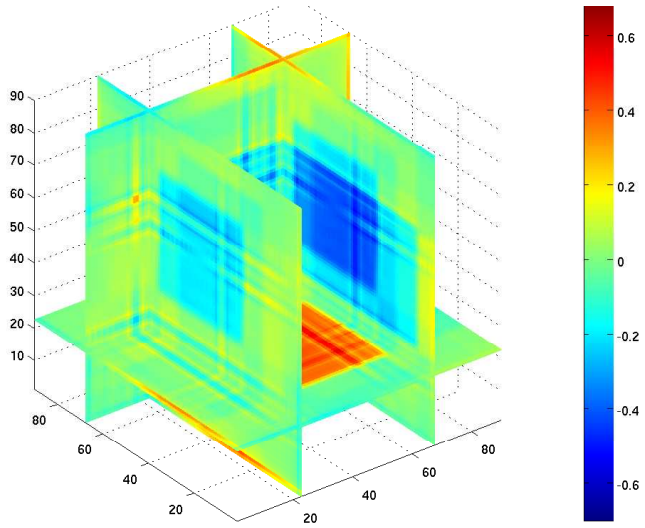

(b) Unstable reconstruction

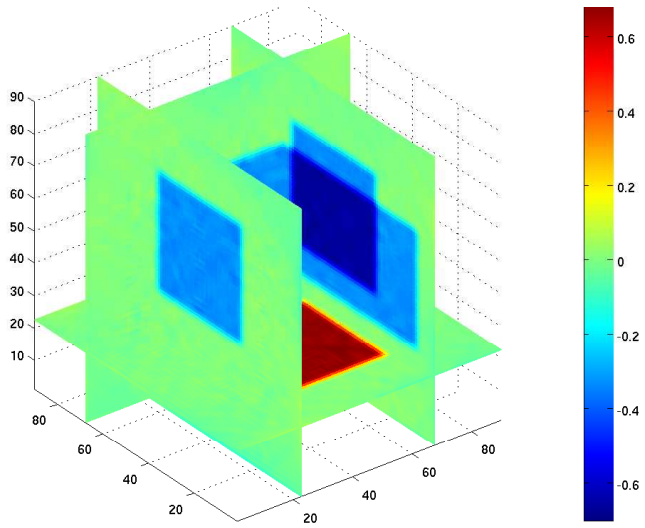

(c) Stable reconstruction

Figure 5.13: Reconstruction of Phantom 2 (sharp edges), f_{11}

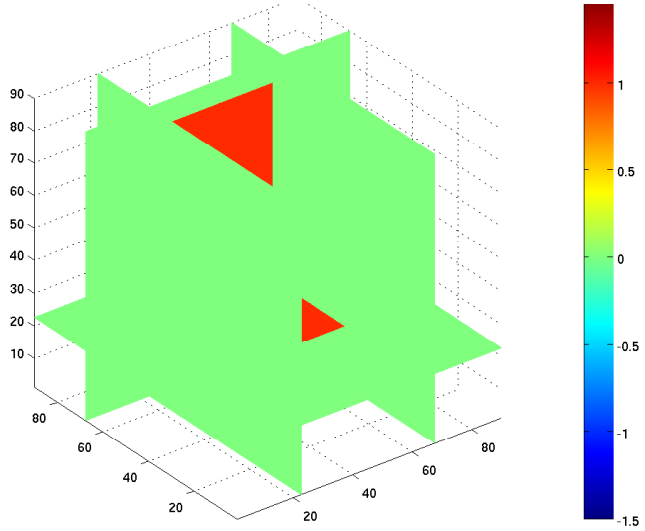

(a) Original phantom

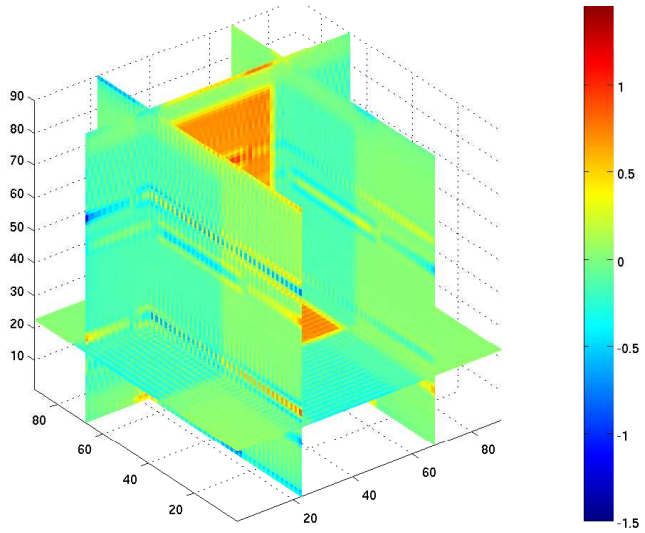

(b) Unstable reconstruction

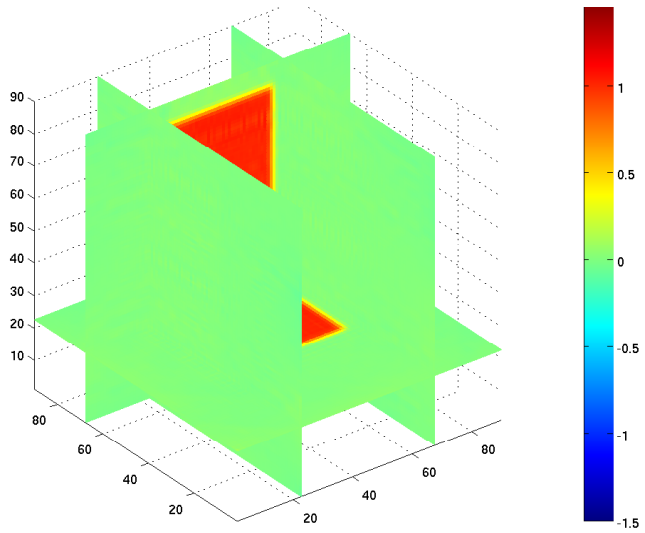

(c) Stable reconstruction

Figure 5.14: Reconstruction of Phantom 2 (sharp edges), f_{12}

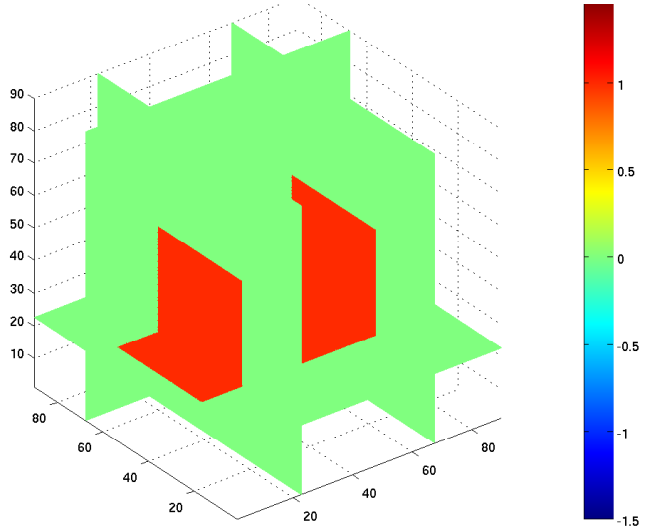

(a) Original phantom

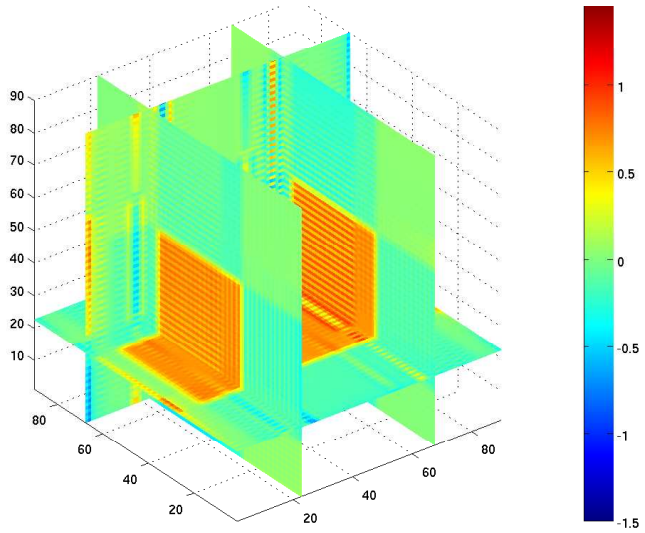

(b) Unstable reconstruction

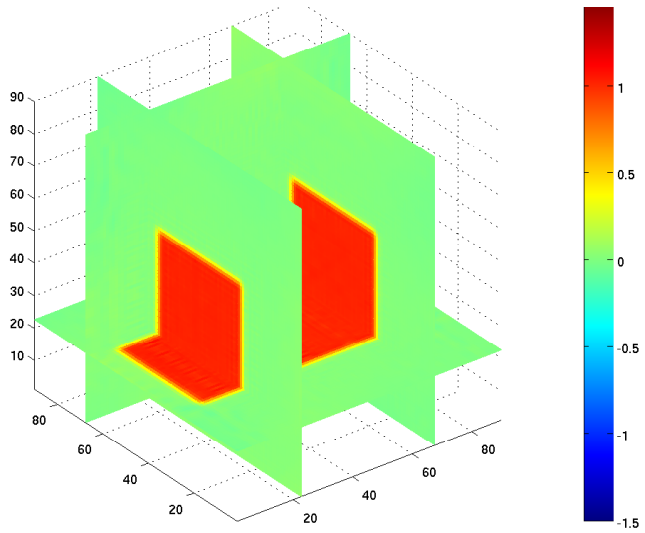

(c) Stable reconstruction

Figure 5.15: Reconstruction of Phantom 2 (sharp edges), f_{13}

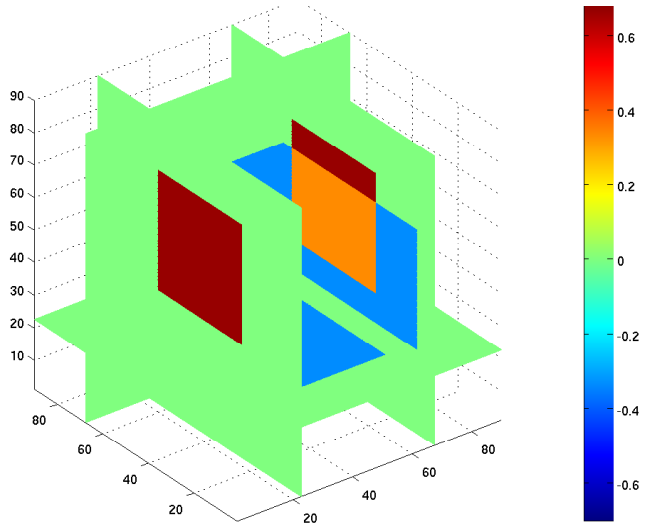

(a) Original phantom

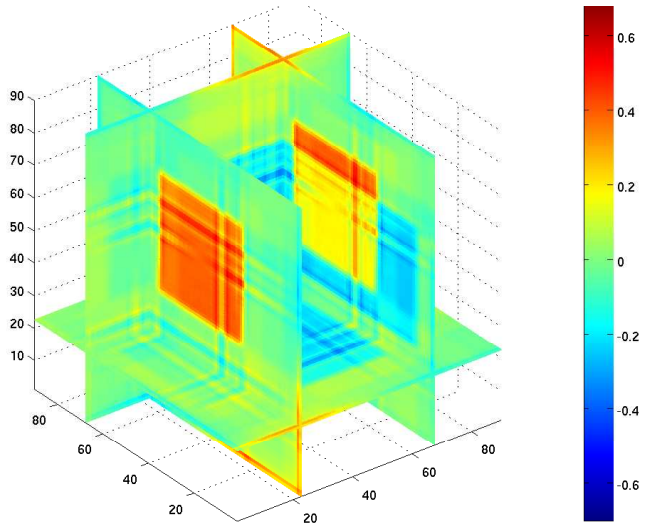

(b) Unstable reconstruction

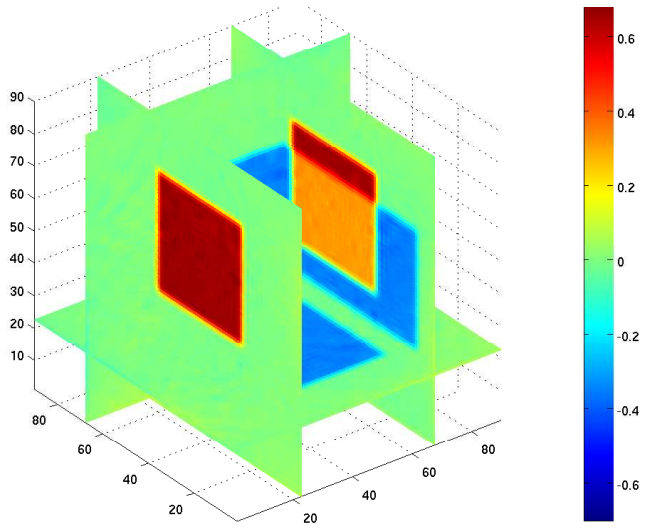

(c) Stable reconstruction

Figure 5.16: Reconstruction of Phantom 2 (sharp edges), f_{22}

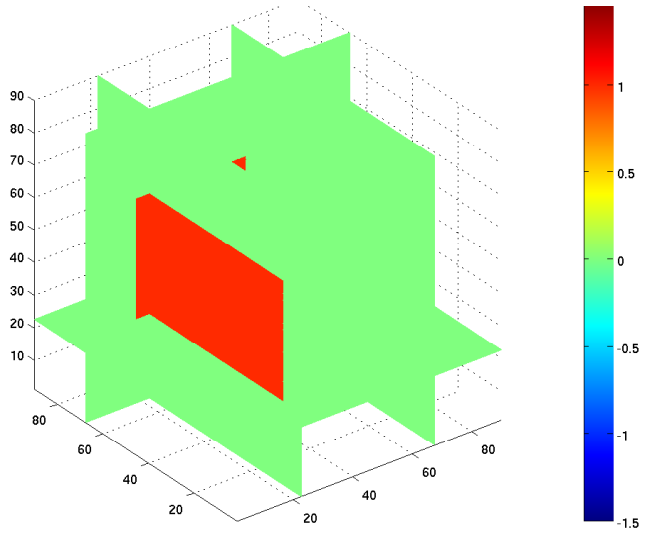

(a) Original phantom

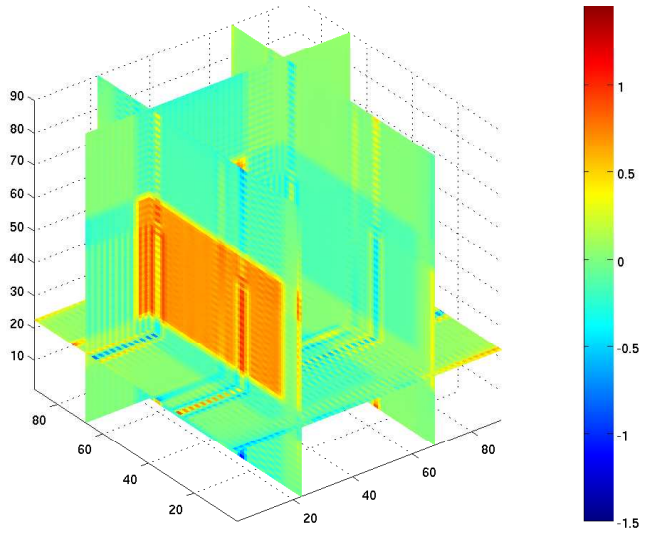

(b) Unstable reconstruction

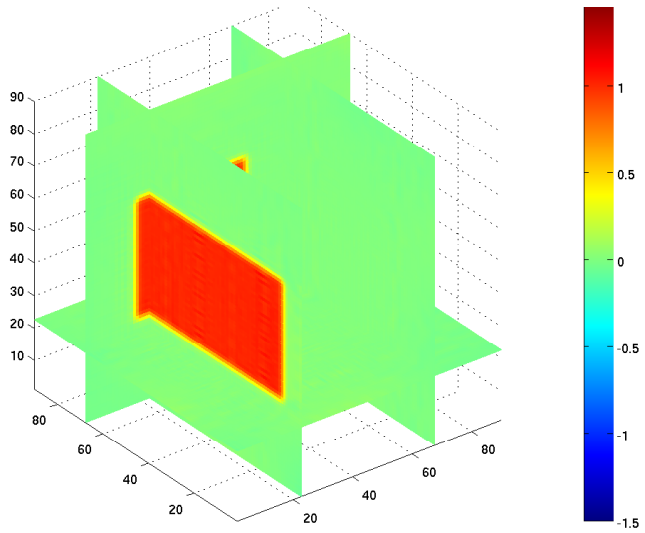

(c) Stable reconstruction

Figure 5.17: Reconstruction of Phantom 2 (sharp edges), f_{23}

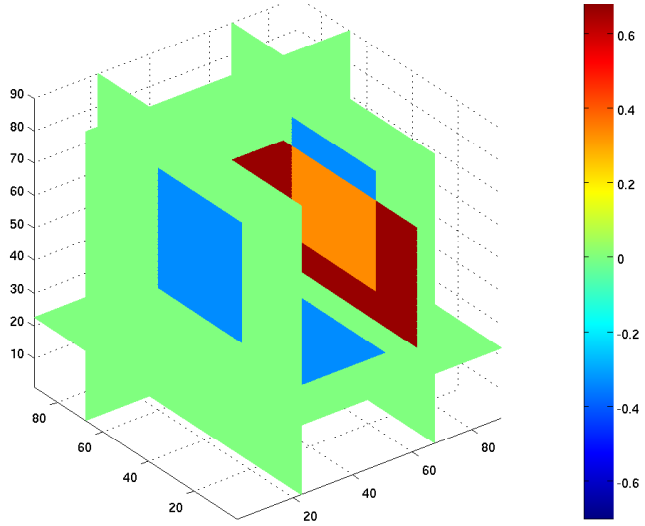

(a) Original phantom

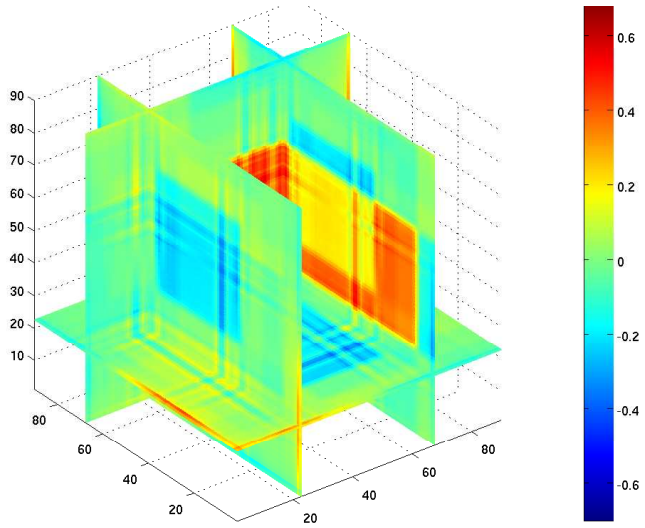

(b) Unstable reconstruction

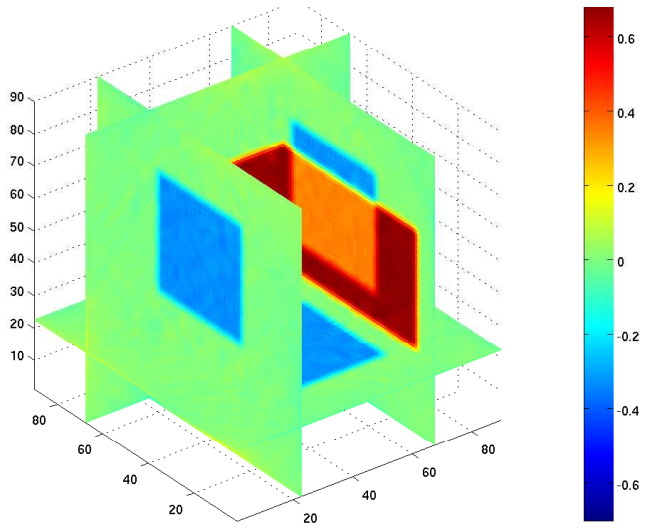

(c) Stable reconstruction

Figure 5.18: Reconstruction of Phantom 2 (sharp edges), f_{33}

5.5 Summary

These results clearly illustrate the performance of the two algorithms. Both the three axis unstable reconstruction and the six axis stable reconstruction show promise. For sufficiently smooth data sets a three axis reconstruction may be acceptable, as may be seen from the results for Phantom 1 in Figures 5.7 – 5.12. There are some visible artefacts but these may be accepted in return for the easier reconstruction. The advantage of only using three axes is particularly apparent when considering the physical issues concerning specimen placement and registration issues in matching views from separate axes of rotation. While acquisition time is dependent on the number of views, rather than the number of axes, a typical system can collect data from a number of views for a fixed axis without user interaction. In the case of the test system [27], each change of axis of rotation requires a user present, so reducing the number of axes needed can greatly reduce the amount of effort required.

Introducing sharp edges as in Phantom 2, the limitation of the unstable reconstruction becomes apparent. As may be seen in Figures 5.13 – 5.18, strong artefacts are visible in the reconstructions with the unstable method. While artefacts are expected, they do appear surprisingly severe. We postulate that there may be another factor affecting the reconstructions: The sharp phantom is aligned with the voxel grid. For the unstable reconstruction, the rotation axes are also aligned with the voxel grid, whereas the axes used for the stable reconstructions are not. To investigate the effect of this further we rotate the phantom by 45° around the x- and y-axes and repeat our experiment.

With the rotated phantom our pane-by-plane visualisation becomes difficult to read, so we use rotated cut-plane instead and look head on for a two dimensional view. The previous and new visualisations are shown in Figure 5.19.

The main instability of the unstable reconstruction algorithm is due to its inability to recover the values of $\hat{f}$ on the coordinate planes. For comparison, as well as displaying the original rotated phantom, we display a version of the phantom where we set the Fourier coefficients on each coordinate plane to zero. As we can see

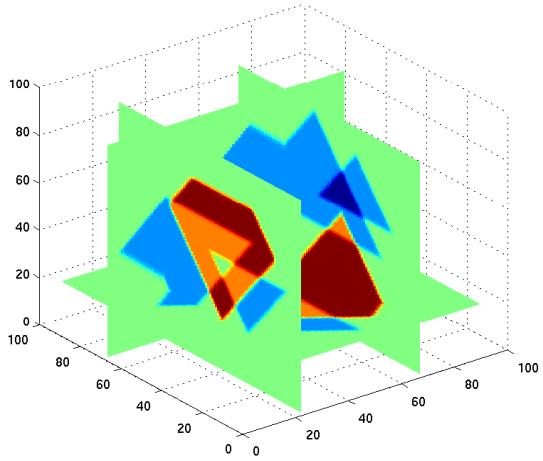

(a) Original view

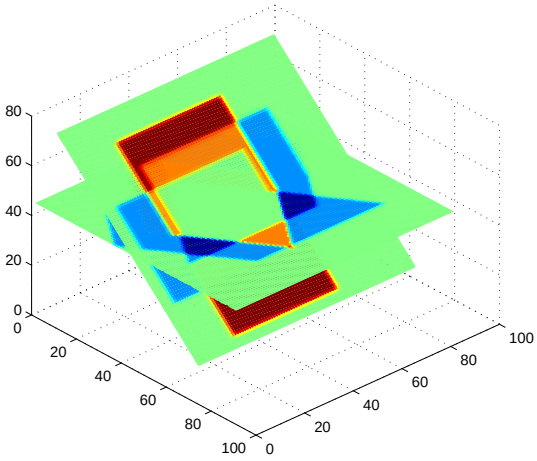

(b) Using tilted cut-planes

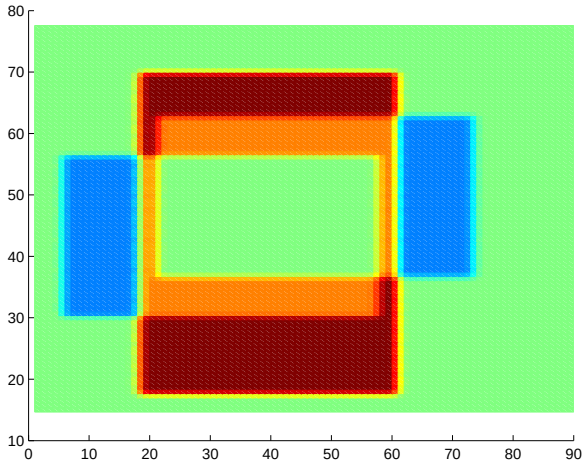

(c) Head-on view

Figure 5.19: Visualisation for rotated phantom

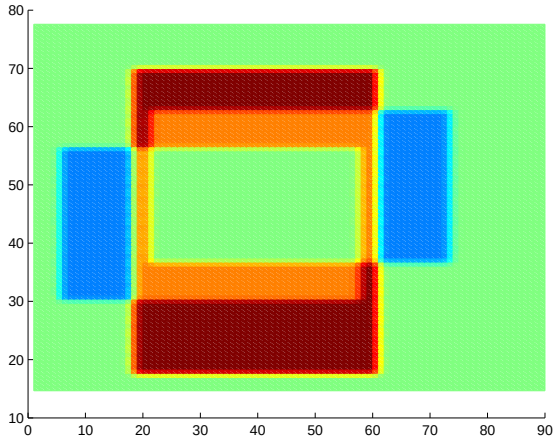

(a) Original phantom

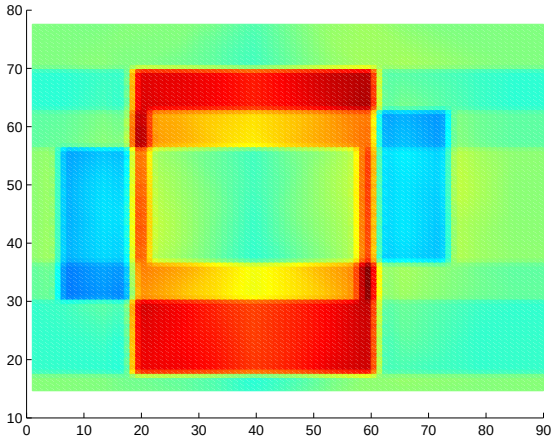

(b) The original phantom with coordinate-plane Fourier components set to zero

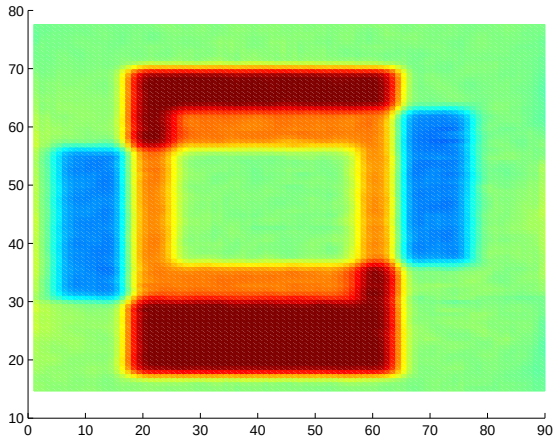

(c) Stable reconstruction

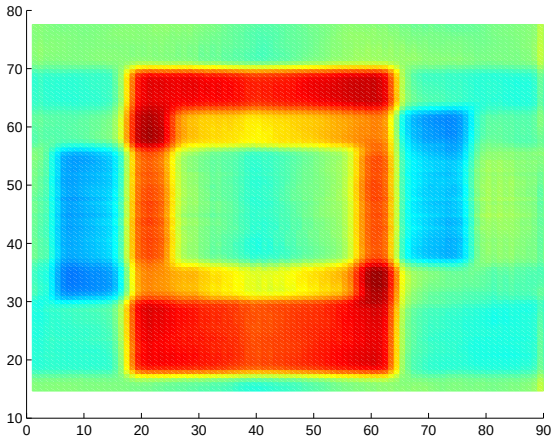

(d) Unstable reconstruction

Figure 5.20: Comparison of artefacts in an unstable reconstruction

in Figure 5.20, the artefacts arising from this manipulation match the artefacts in the unstable reconstruction very well. In general these are much less severe than in the axis-aligned phantom, but they are still strong enough to justify a six-axis reconstruction.

Chapter 6

Conclusions and Future Work

This concludes our investigations into x-ray and photoelastic tomography. While this thesis is finished, the subject is by no means closed. We give some thoughts on our journey, and on where to go next.

We have presented new reconstruction results for photoelastic tomography, focusing on limited data problems. We begin with the observation that three dimensional photoelastic tomography, like three dimensional scalar tomography is dimensionally overdetermined. This is fortunate, since collecting full three dimensional tomographic data is extremely difficult, as this would entail scans from directions covering half a sphere. In this sense, only limited data sets may be collected but our initial numerical studies show that these limited sets are sufficient for full reconstruction.

We have described an algorithm recently developed by Sharafutdinov and Lionheart which gives an explicit reconstruction algorithm for this type of limited data. With this as our starting point we first extended this excellent work from the Schwartz class to Sobolev spaces, also giving stability results. We then moved on to describe several novel reconstruction algorithms for certain commonly occurring special cases of tensors. We also extended our new results to certain cases of data truncation. Finally, we gave the first results of numerical implementation of Sharafutdinov and Lionheart's algorithm.

During our investigations we made some observations which are relevant in a more general inverse problems setting:

6.1 Deceptive singular value decomposition

The SVD is a commonly used numerical tool for understanding under-determined and ill-conditioned problems. While very useful for lower dimensional problems, care is needed when applying such techniques to problems in higher dimensions. Due to computational complexity, in particular with tensor valued functions of three dimensions, only very coarse grids may be possible.

Our initial numerical investigations included a study of the SVD of our forward model. However, this did not tell the whole story and indeed also gave slightly misleading results. Looking at just the singular values of the TTRT for one axis, suggested that a complete reconstruction might be possible. Carrying out a numerical reconstruction on the other hand gave very poor results. Going back to the theory we were able to prove the existence of a nullspace. The moral is that results need to be taken with a pinch of salt, especially when the singular vectors are unavailable or difficult to interpret.

6.2 Future work

There are a number of obvious directions in which to continue this research. While we have extended the general reconstruction algorithm of Sharafutdinov and Lionheart to Sobolev spaces, it is still restricted to a linear approximation. The next step in this direction is to use projective Newton methods in an iterative non-linear scheme. This would involve a full ODE solution along each ray to solve the forward problem of Rytov-Kravtsov. Novikov [19] takes this approach for the non-truncated TRT.

On the numerical side, we believe the implementation is ready to be tested in experimental data. Until now, TTRT data has unfortunately been difficult to collect but further numerical studies are also of interest. More simulated experiments investigating performance at various noise levels would no doubt be useful.

We have showed that reconstruction of the full tensor requires data from at least two, and most likely three axes of rotation. To achieve stable reconstruction of full

tensors yet more axes are needed. However, as is often the case for inverse problems, it is worth going back to the underlying question. For some applications, it may not be the tensor itself, but rather some property calculated from it that is actually sought. Such properties include the von Mises yield criterion or other tensor invariants. It may be possible to recover such invariants of the tensor, stably or unstably from fewer axes of rotation.

The experimental work considered is currently only for parallel light rays. In many practical applications of x-ray tomography, there has been a tendency to move towards fan beam and cone beam acquisition modalities. Since a parallel ray geometry suits our current experimental setup, this is where our theoretical work was focused. Extending this work to other measurement geometries is yet another interesting open problem in this field.

Finally, it would be interesting to find some parallels to other fields of applied tensor tomography. Applications known to this author include diffusion MRI and seismic imaging. However, these are closer in nature to the TRT, whereas photoelastic tomography suffer the added complication of the TTRT. For the former problems, one common problem is the choice of measurement axes. It is clear that six axes whose outer product spans the space of symmetric matrices are needed, but a possible optimal choice of such is not known. For the TTRT case we are only recovering the deviatoric part of the tensor field, and it not clear what the minimal number of measurements are. Further investigation would benefit not only photoelastic, but may yield results relevant to other fields using tensor tomography.

Bibliography

[1] H. Aben. *Integrated Photo-elasticity*. McGraw-Hill Inc.,US, 1979.

[2] H. Aben, A. Errapart, L. Ainola, and J. Anton. Photoelastic tomography for residual stress measurement in glass. *Optical Engineering*, 44(9):093601, 2005.

[3] C. Amrouche, P.G. Ciarlet, L. Gratie, and S. Kesavan. On Saint Venant's compatibility conditions and Poincaré's lemma. *Comptes rendus-Mathématique*, 342(11):887–891, 2006.

[4] I. K. Chun, M. H. Cho, S. C. Lee, M. H. Cho, and S. Y. Lee. X-ray micro-tomography system for small-animal imaging with zoom-in imaging capability. *Physics in Medicine and Biology*, 49(17):3889–3902, 2004.

[5] H. W. Engl, M. Hanke, and A. Neubauer. *Regularization of Inverse Problems (Mathematics and Its Applications)*. Springer, 2000.

[6] H. Hammer and W.R.B. Lionheart. Reconstruction of spatially inhomogeneous dielectric tensors through optical tomography. *Journal of the Optical Society of America A-Optics Image Science and Vision*, 22(2):250–255, FEB 2005.

[7] P. C. Hansen. Regularization tools: A matlab package for analysis and solution of discrete ill-posed problems. *Numerical Algorithms*, 6:1–35, 1994.

[8] J. Hsieh, E. Chao, . J. Thibault, B. Grekowicz, A. Horst, S. McOlash, and T. J. Myers. A novel reconstruction algorithm to extend the CT scan field-of-view. *Medical Physics*, 31:2385–2391, 2004.

[9] Y. C. Hung, J. A. Bennett, F. A. Garcia-Pastor, M. Di Michlel, J. Y. Buffière, T. J. A. Doel, P. Bowen, and P. J. Withers. Fatigue crack growth and load redistribution in Ti/SiC composites observed in situ. *Acta Materialia*, 57(2):590–599, Jan 2009.

[10] F. Jacobs, E. Sundermann, B. De Sutter, M. Christiaens, and I. Lemahieu. A fast algorithm to calculate the exact radiological path through a pixel or voxel space.

[11] W. A. Kalender. X-ray computed tomography. *Physics in Medicine and Biology*, 51(13):R29–R43, 2006.

[12] M. Lak, D. Neraudeau, A. Nel, P. Cloetens, V. Perrichot, and P. Tafforeau. Phase contrast X-ray synchrotron imaging: Opening access to fossil inclusions in opaque amber. *Microscopy and Microanalysis*, 14(3):251–259, Jun 2008.

[13] L. D. Landau and E. M. Lifshitz. *Electrodynamics of Continuous Media (Course of Theoretical Physics)*. Pergamon P, 1984.

[14] A. Lefèvre. Development of novel apparatus for 3D stress analysis. Master's thesis, The University of Sheffield, UK, 2009.

[15] W. Lionheart and V. Sharafutdinov. Reconstruction algorithm for the linearized polarization tomography problem with incomplete data. In *Imaging Microstructures: Mathematical and Computational Challenges*, volume 494, pages 137–159. Amer Mathematical Soc, 2009.

[16] S. G. Mikhlin. *Integral equations and their applications to certain problems in mechanics, mathematical physics, and technology*. London : Pergamon Press, 1957.

[17] F. Natterer. *The Mathematics of Computerized Tomography*. Society for Industrial and Applied Mathematics, 2001.

[18] F. Noo, R. Clackdoyle, and J. D. Pack. A two-step Hilbert transform method for 2D image reconstruction. *Phys. In Medicine Biol.*, 49(17):3903–3923, 2004.

[19] R. G. Novikov. On Iterative Reconstruction in the Nonlinearized Polarization Tomography. *Inverse Problems*, 25(11), Nov 2009.

[20] C. E. Pearson. *Theoretical Elasticity*. Harvard Univ Pr, 1959.

[21] J. Radon. Über die bestimmung von funktionen durch ihre integralwerte längs gewisser mannigfaltigkeiten. *Leipz. Ber.*, 69:262–277, 1917.

[22] A.G. Ramm and A.I. Katsevich. *The Radon Transform and Local Tomography*. CRC Press, Boca Raton, Florida, 1996.

[23] I. Richards and H. Youn. *Theory of Distributions: A Non-technical Introduction*. Cambridge University Press, 1990.

[24] V. A. Sharafutdinov. *Integral Geometry of Tensor Fields (Inverse and Ill-Posed Problems)*. Walter de Gruyter, 1994.

[25] R. L. Siddon. Fast Calculation of the Exact Radiological Path for a 3-Dimensional CT Array. *Medical Physics*, 12(2):252–255, 1985.

[26] G. Sparr and K. Stråhlén. Vector field tomography, an overview. 1998.

[27] D. Szotten, W.R.B. Lionheart, and R. A. Tomlinson. Tomographic reconstruction of stress from photoelastic measurements using elastic regularization. MIMS EPrint 2006.5, Manchester Institute for Mathematical Sciences, University of Manchester, Manchester, UK, January 2006.

[28] S. Timoshenko and J.N. Goodier. *Theory of Elasticity*. McGraw-Hill Book Company, New York, second edition, 1951.

[29] M. L. L. Wijerathne, Kenji Oguni, and Muneo Hori. Stress field tomography based on 3D photoelasticity. *Journal of the Mechanics and Physics of Solids*, 56(3):1065–1085, Mar 2008.

[30] H. Yang, S. Gibson, and R. A. Tomlinson. Improvement of fourier polarimetry for applications in tomographic photoelasticity. *Experimental Mechanics*, 46(5):619–626, October 2006.

[31] J. S. You and G. L. Zeng. Explicit finite inverse Hilbert transforms. *Inverse Problems*, 22(3):L7–L10, 2006.